ON THE UNCERTAINTIES AND DYNAMICS OF PACIFIC INTERANNUAL AND DECADAL CLIMATE VARIABILITY AND CLIMATE CHANGE

A Dissertation
Presented to
The Academic Faculty

by

Jason C. Furtado

In Partial Fulfillment
of the Requirements for the Degree
Doctor of Philosophy in the
School of Earth and Atmospheric Sciences

Georgia Institute of Technology
December 2010

ON THE UNCERTAINTIES AND DYNAMICS OF PACIFIC INTERANNUAL AND DECADAL CLIMATE VARIABILITY AND CLIMATE CHANGE

Approved by:

Dr. Emanuele Di Lorenzo, Advisor
School of Earth and Atmospheric Sciences
Georgia Institute of Technology

Dr. Peter J. Webster
School of Earth and Atmospheric Sciences
Georgia Institute of Technology

Dr. Robert X. Black
School of Earth and Atmospheric Sciences
Georgia Institute of Technology

Dr. Bruce T. Anderson
Department of Geography and Environment
Boston University

Dr. Kim M. Cobb
School of Earth and Atmospheric Sciences
Georgia Institute of Technology

Date Approved: 1 November 2010

ACKNOWLEDGEMENTS

First and foremost, I would like to thank God for all of His blessings and His help through the difficult times in my graduate school career and the challenges I faced while pursuing my doctorate degree.

Secondly, I would like to thank my advisor, Dr. Emanuele ("Manu") Di Lorenzo, for his help and guidance throughout my Ph.D. career. He has helped to shape me into the well-rounded climate scientist that I am today. I would also like to thank my committee members: Dr. Robert X. Black, Dr. Kim M. Cobb, Dr. Peter J. Webster, and Dr. Bruce T. Anderson for their contributions to various parts of the research and providing insightful and constructive comments on my dissertation. Many thanks also to the members of the Di Lorenzo Research Group, past and present, for their camaraderie throughout my Ph.D. career at Georgia Tech.

I would also like to thank my masters advisor, Dr. David W. J. Thompson from Colorado State University (CSU). As my first graduate school advisor, he shaped my interest in large-scale climate dynamics and also taught me a lot about statistics and how to interpret them. One of his favorite sayings was "Always remember the big picture." I continue to follow that advice today.

For specific scientific comments and discussion throughout my graduate school career, I would like to thank Laura Ciasto, Ph.D., my former CSU officemate and continued friend, Cegeon Chan, Ph.D., a longtime college friend who inspired me to keep working on this dissertation, and James Benedict, Ph.D., who also continued to push me to write and finish this dissertation.

Finally, thank you to my friends and family, particularly my parents who have been there through it all and supported me in the most stressful of times to remain

focused and keep my eyes on the prize. I would not be the person I am today without their love and support.

The work presented in this dissertation was funded through several grants from three agencies: (1) the National Science Foundation (NSF) (OCE-0550266, OCE-0606575, and OCE-0815280); (2) the National Aeronautics and Space Administration (NASA) (OES-NNG05GC98G); and (3) the National Oceanic and Atmopsheric Administration (NOAA) (NA06OAR4310116).

TABLE OF CONTENTS

LIST OF TABLES

LIST OF FIGURES

LIST OF ABBREVIATIONS

ACF	Autocorrelation Function
AGCM	Atmospheric General Circulation Model
AL	Aleutian Low
AR-1	Autoregressive Order 1
cEOF	Combined Empirical Orthogonal Function
CFR	Climate Field Reconstruction
CMAP	Climate Prediction Center Merged Analysis of Precipitation
CMIP3	Coupled Model Intercomparison Project, Phase 3
CO_2	Carbon Dioxide
CPW	Central Pacific Warming
CSIRO	Commonwealth Scientific and Research Organization
DJF	December, January, and February
EC	Expansion Coefficient
ENSO	El Niño-Southern Oscillation
EOF	Empirical Orthogonal Function
ERA-40	European Centre for Medium-Range Weather Forecasts Re-Analysis
FFT	Fast Fourier Transform

FTP	File Transfer Protocol
GCM	General Circulation Model
ICTP	International Centre for Theoretical Physics
IPCC	Intergovernmental Panel on Climate Change
IPCC AR4	Intergovernmental Panel on Climate Change Fourth Assessment Report
LSV	Left Singular Vector
MSE	Mean Square Error
NAO	North Atlantic Oscillation
NASA	National Aeronautics and Space Administration
NCEP/NCAR	National Centers for Environmental Prediction/National Center for Atmospheric Research
NDJFM	November, December, January, February, and March
NOAA	National Oceanic and Atmospheric Administration
NOAA ER SSTs	National Oceanic and Atmospheric Administration Extended Reconstruction Sea Surface Temperature Dataset
NPDV	North Pacific Decadal Variability
NPGO	North Pacific Gyre Oscillation
NPO	North Pacific Oscillation
NPO NP	The Northern Pole of the North Pacific Oscillation Pattern

NPO SP	The Southern Pole of the North Pacific Oscillation Pattern
OPeNDAP	Open-source Project for a Network Data Access Protocol
PC	Principal Component
PCA	Principal Component Analysis
PCMDI	Project for Climate Model Diagnosis and Intercomparison
PDF	Probability Distribution Function
PDO	Pacific Decadal Oscillation
RMS	Root Mean Square
RSV	Right Singular Vector
SLP	Sea Level Pressure
SLPa	Sea Level Pressure Anomalies
SNR	Signal-to-Noise Ratio
SPCZ	South Pacific Convergence Zone
SST	Sea Surface Temperature
SSTa	Sea Surface Temperature Anomalies
SVD	Singular Value Decomposition
WES	Wind-Evaporation-Sea Surface Temperature
YBP	Years Before Present

SUMMARY

Tropical and extratropical Pacific decadal climate variability substantially impact physical and biological systems in the Pacific Ocean and strongly influence global climate through teleconnection patterns. Current understanding of Pacific decadal variability centers around three key modes of variability in the atmosphere and ocean: the El Niño-Southern Oscillation (ENSO), the Aleutian Low (AL), and the Pacific Decadal Oscillation (PDO). However, recent literature has highlighted the emerging roles of secondary modes of variability of the tropical and extratropical Pacific atmosphere and ocean that explain and drive other aspects of the climate system (i.e., the Central Pacific Warming (CPW) phenomenon, the North Pacific Oscillation (NPO), and the North Pacific Gyre Oscillation (NPGO)). This work analyzes the statistics and uncertainties behind Pacific interannual and decadal-scale climate variability in observations and models, and in particular, focuses on better understanding the importance of the roles of the CPW, NPO, and NPGO for predictability of global climate change.

The study begins by examining the dynamics of the NPO and its role in Pacific interannual and decadal climate variability. While the NPO is considered an intrinsic mode of atmospheric variability in the North Pacific, analyses demonstrate that the individual poles of the NPO behave differently. In particular, the subtropical node contains strong power at low frequencies (periods of 7-10 years), but not the northern pole. The source of this low-frequency variability in the southern node of the NPO is tropical Pacific sea surface temperature (SST) variability, as shown through a simple modeling experiment. NPO variability is further divided into: (a) a high-frequency component associated with stochastic forcing and the ENSO precursor signature; and

(b) a low-frequency component directly connected with tropical Pacific SST forcing. The NPO-induced variability by the tropical Pacific SSTa is then integrated by the underlying ocean surface to form the decadal-scale NPGO signal. Thus, a new link between the CPW, the NPO, and the NPGO is formed, akin to the ENSO-AL-PDO framework.

The new framework of North Pacific decadal variability (NPDV) is then evaluated in 24 state-of-the-art coupled climate models used for the Intergovernmental Panel on Climate Change (IPCC) Fourth Assessment Report (AR4). Results indicate that the PDO and NPGO do not exhibit significant changes in their spatial and temporal characteristics under projected greenhouse warming. However, the ability of the models to capture the dynamics associated with the PDO and NPGO is questionable. The temporal and spatial statistics of PDO and NPGO exhibit significant discrepancies from observations in their 20^{th} century climate, especially for the NPGO. Furthermore, most models lack the proper connections between extratropical and tropical Pacific, for both the ENSO-AL-PDO and CPW-NPO-NPGO connections. In fact, the atmospheric teleconnections associated with the CPW phenomenon in some models have a significant projection on, and excite, the AL/PDO coupled mode instead.

The last part of the dissertation explores further the importance of the CPW mode by comparing and contrasting two popular paleoclimate SST anomaly reconstruction methods used for tropical Indo-Pacific SSTs. The first method exploits the high correlation between the canonical ENSO mode and tropical precipitation; the second method uses a multi-regression model that exploits the multiple modes of covariability between tropical precipitation and SSTs, including the CPW mode. The multi-regression approach demonstrates higher skill throughout the tropical Indo-Pacific than the first approach, illustrating the importance of including the CPW phenomenon in understanding past climates.

CHAPTER I

INTRODUCTION

The Pacific Ocean is the largest ocean basin on Earth, covering close to 30% of the total surface area of the planet. Figure 1.1 shows the mean observed sea surface temperatures (SSTs) (Fig. 1.1a) and standard deviation of SSTs (Fig. 1.1b) in the Pacific basin. In the mean SST field, one prominent feature is the strong zonal gradient in SSTs across the equatorial Pacific (between the Maritime Continent and South America). The warmest SSTs found on Earth reside in the western tropical Pacific Ocean - i.e., the West Pacific Warm Pool. Moving eastward along the equator toward South America, the SSTs decrease. A "tongue" of relatively colder waters extends from the central equatorial Pacific towards the Peruvian coast. This area of colder waters results from upwelling of colder waters due to trade wind forcing. The colder waters along the South American coast are also from upwelling associated with the Humboldt Current. The standard deviation of SSTs (Fig. 1.1b) shows two regions of high variability: (a) off the coast of Japan and into the central North Pacific, associated with variations in the Kuroshio Current; and (b) a relatively weaker but still noticeable area associated with the equatorial Pacific cold tongue region and upwelling along the Peruvian coast. The latter region of high SST variability is directly associated with the El Niño-Southern Oscillation (ENSO) phenomenon, arguably the most prominent and largest global climate signal on Earth.

Walker and Bliss (1932) pioneered efforts to examine large-scale patterns of variability in the data-sparse Pacific Ocean, among other global locations. In the paper, the authors studied sea level pressure (SLP) records from several stations across the globe and examined covarying patterns of SLP variability. Among several

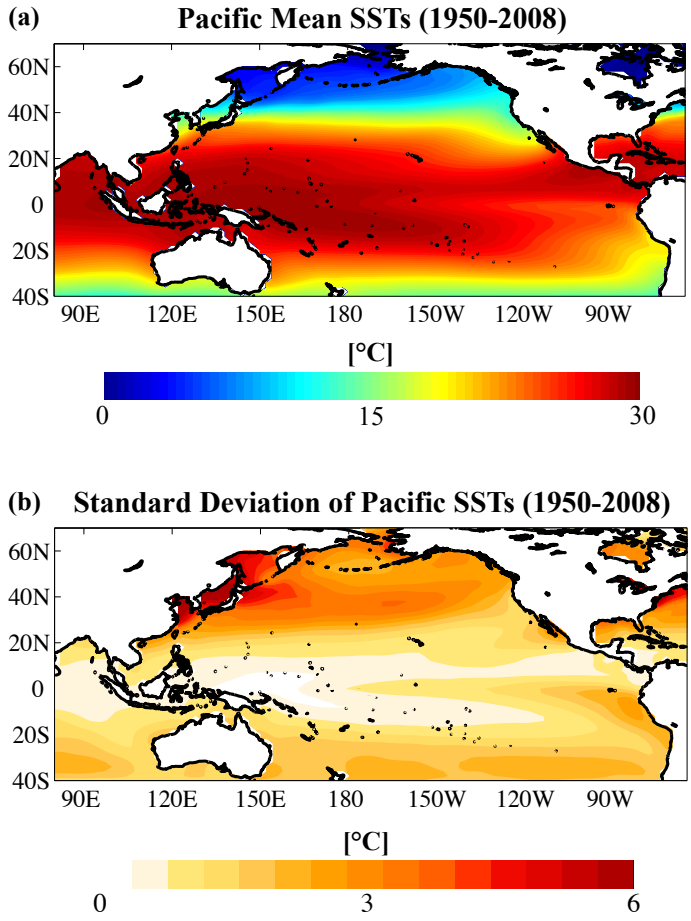

FIG. 1.1. (a) Mean Pacific SSTs (°C) from 1950 - 2008. (b) The standard deviation (°C) of Pacific SSTs from 1950 - 2008. SST data used are from monthly-mean fields from the NOAA ER SSTs (see Section 2.1.1 for more information).

patterns of covariability identified, Walker and Bliss (1932) were among the first to identify two oscillations in Pacific basin atmospheric pressure: the Southern Oscillation Index (SOI), a difference in surface pressure between the island of Tahiti and Darwin, Australia, and the North Pacific Oscillation (NPO), an SLP dipole between Alaska and Hawaii. The former became a central component of the studies of ENSO that ensued in the second half of the 20^{th} century, while the latter pattern remained essentially dormant in the climate literature until the early 2000s.

Following Walker and Bliss's work, interest in North Pacific climate variability remained of interest, but mostly academic rather than for practical and predictability

applications. However, by the middle of the 20^{th} century, economic impacts on the fishing industry and societal impacts of periodic changes in weather conditions motivated ventures into better understanding and predicting Pacific climate variability on multiple timescales (seasonal, interannual, and multi-decadal). Anecdotal evidence of changes in fish catches off of Peru and changes in tropical and subtropical Pacific rain patterns on intradecadal timescales were directly tied to the ENSO phenomenon. In the North Pacific, a number of studies presented evidence of longer-term variability, including changes in salmon population (Mantua et al., 1997), sardine catches (Yasuda et al., 1999) and other biological variables along the western North American coast (Miller et al., 2004). Evidence of the changes and variability in the Pacific on the multi-decadal scale are also supported in several paleoclimate records (e.g., Urban et al. 2000; Cole et al. 2000; Evans et al. 2001). Furthermore, the impacts of sensible weather and climate patterns downstream in the Northern Hemisphere (e.g., Latif and Barnett 1996), originating from the leading mode of Pacific interannual and decadal variability, led efforts to improve its prediction for seasonal forecasting applications. Of late, concerns over global climate change from increased greenhouse forcing and anthropogenic carbon dioxide (CO_2) emissions have heightened awareness of the importance of potential changes in the major modes of Pacific climate variability. To date, uncertainties in interannual and decadal climate variability in the Pacific, as expressed by the Intergovernmental Panel on Climate Change (IPCC) Fourth Assessment Report (AR4), remains a prime question in climate dynamics research.

In this chapter, the underlying basics for the research conducted in this dissertation is laid out. First, an overview of the major patterns of large-scale variability, both oceanic and atmospheric, that govern Pacific decadal variability studies is presented. These modes are interlinked, so understanding the dynamics and evolution of one mode in a certain region requires knowledge of the evolution of other modes

throughout the Pacific basin. Then, two particular mechanisms linking North Pacific and tropical Pacific climate variability at various timescales are explained in detail. These mechanisms will be central in evaluating the fidelity of model output and in discerning new connections and mechanisms proposed in this work. Motivating factors for the research conducted, the objectives of the study, and an outline of the dissertation follow.

1.1 The Leading Modes of Variability in the Pacific Basin

1.1.1 North Pacific Oceanic Modes

The two leading patterns of North Pacific climate variability are also the ones that contribute the most to North Pacific decadal variability (NPDV): the Pacific Decadal Oscillation (PDO; Mantua et al. 1997) and the North Pacific Gyre Oscillation (NPGO; Di Lorenzo et al. 2008). The leading mode, the PDO, was identified through two key observations suggesting low frequency variability in North Pacific SST anomalies (SSTa). One was in relation to the "climate transition" of 1976/77, formally identified first by Miller et al. (1994) but also referred to in numerous other studies (e.g., Trenberth 1990; Ebbesmeyer et al. 1991; Graham et al. 1994; Zhang et al. 1997). The "climate transition" was noted by an extended period of El Niño-like conditions throughout the North Pacific without a significant continuous El Niño event in the tropical Pacific. The second key observation leading to the PDO identification was the inverse relationship between salmon catches in the Gulf of Alaska and those in the Pacific Northwest recognized by Francis and Sibley (1991) and Mantua et al. (1997). The latter authors tied this cyclic relationship to a particular transient, low-frequency pattern of North Pacific SSTs, terming this pattern the PDO.

Figures 1.2a and 1.2b present the spatial pattern and standardized time series of the PDO. As the leading empirical orthogonal function (EOF) of North Pacific

SSTa, the PDO describes nearly 21% of the variance in the field. The positive phase of the PDO is characterized by negative SSTa in the central North Pacific encircled by positive SSTa along the North American coastline (Fig. 1.2). The PDO index (Fig. 1.2b) shows that the phenomenon experiences multi-decadal variability, with a period of negative values from the 1950s to the mid-1970s, followed by a shift toward positive values in the 1980s and 1990s. Within the last decade, the PDO has transitioned again toward its negative phase.

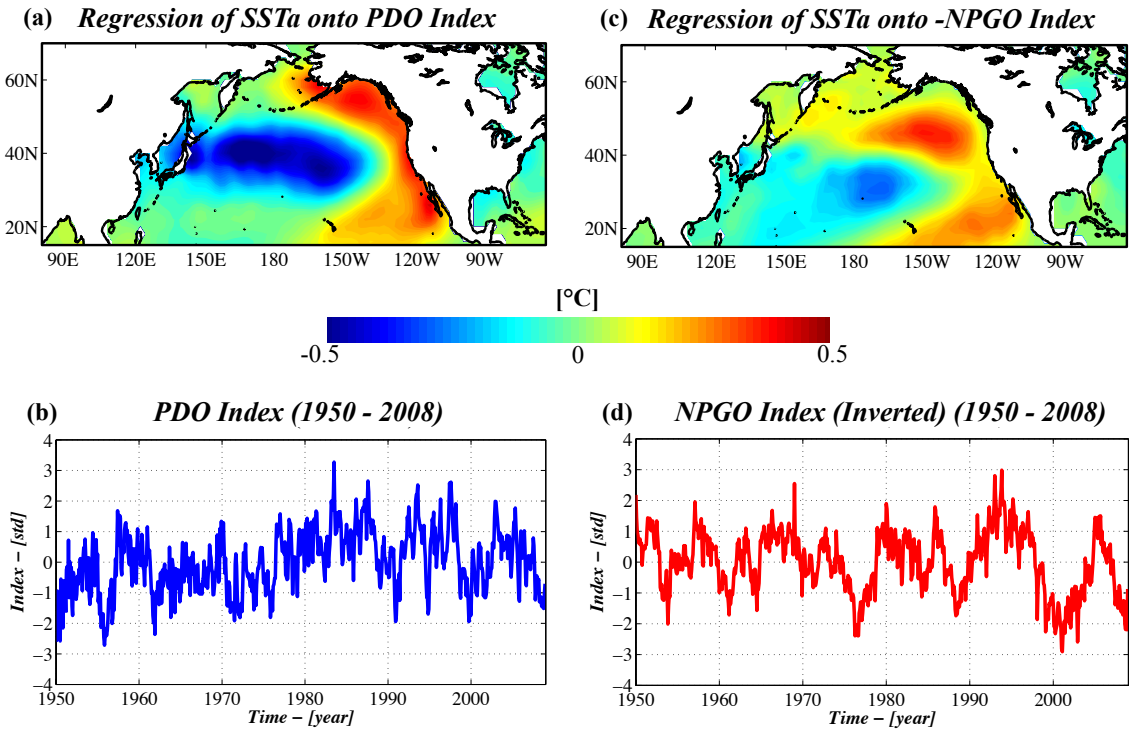

FIG. 1.2. (a) Regression of monthly-mean SSTa (°C) from 1950 - 2008 onto the standardized PDO index (found at `http://jisao.washington.edu/pdo/PDO.latest`). (b) The PDO index (standardized) from 1950 - 2008. (c) As in (a) but for regression onto the inverted NPGO index (found at `http://ocean.eas.gatech.edu/npgo`). (d) As in (b) but for the inverted NPGO index (standardized).

The second leading pattern of North Pacific oceanic climate variability, the NPGO, is formally defined as the second EOF of northeast Pacific sea surface height (SSH) anomalies (Di Lorenzo et al., 2008). This mode of variability physically represents changes in the strength of the subtropical and subpolar gyres in the North Pacific

and tracks prominent decadal fluctuations in salinity and nutrients observed in the central and eastern North Pacific, previously unexplained by the PDO (Di Lorenzo et al., 2008, 2009). Ceballos et al. (2009) also linked the NPGO to changes in strength of the Kuroshio-Oyashio Extension current, therefore showing that NPGO variability latitudinally spans the North Pacific. Figs. 1.2c and 1.2d illustrate the characteristic pattern of the NPGO in SSTs and the temporal evolution of the mode, respectively[1]. The SSTa regression pattern associated with the NPGO shows negative SSTa in the central North Pacific and a ring of positive SSTa with in the northeastern Pacific, extending along the coast of California, and then southwestward near and to the south of Hawaii. This pattern is closely related to the second leading mode of North Pacific SSTa, referred to as the "Victoria" mode (Bond et al., 2003), and the second leading mode of Pacific-wide SSTa (Di Lorenzo et al., 2008). The second leading mode of North Pacific SSTa (i.e., that congruent with the NPGO) describes nearly 11% of variance in North Pacific monthly-mean SSTa. The evolution of the NPGO over the last half of the 20th century/early part of the 21st century (Fig. 1.2d) shows a low-frequency cyclic phenomenon with two periods of sharp turns toward negative values: in the mid-1970s, close to the "climate transition" period, and the late 1990s/early 2000s.

1.1.2 North Pacific Atmospheric Modes

The leading modes of the North Pacific SST field are intimately tied to the two leading modes of North Pacific SLP anomalies (SLPa). Figure 1.3 displays the spatial patterns and time series for these two leading atmospheric modes of variability. The leading climate pattern of SLPa variability in the North Pacific is the Aleutian Low (AL), explaining 23% of of the variance of North Pacific SLPa (27% of the

[1]For the purposes of the discussion, we have inverted the NPGO index for the regression and the time series plots. This inversion is done to better visualize connections with other modes of variability, shown throughout the dissertation.

wintertime variance in boreal winter SLPa, when the AL is the most active). The AL is characterized by a broad area of negative SLPa over the far northern Pacific, near and to the southeast of the Aleutian Islands (hence its name; Fig. 1.3a). Physically, this pattern of variability represents the paths of extratropical cyclones in the North Pacific and where the storms mature / decay. The anomalous wind stresses associated with the AL act as the atmospheric forcing for the PDO (Miller et al., 2004; Chhak et al., 2009). The AL index (Fig. 1.3b) further illustrates that the pattern is governed by high-frequency variability, but there are important low-frequency variations in the AL, similar to the PDO (e.g., Trenberth 1990; Deser et al. 2004).

The second leading pattern of North Pacific SLPa is characterized by a dipole

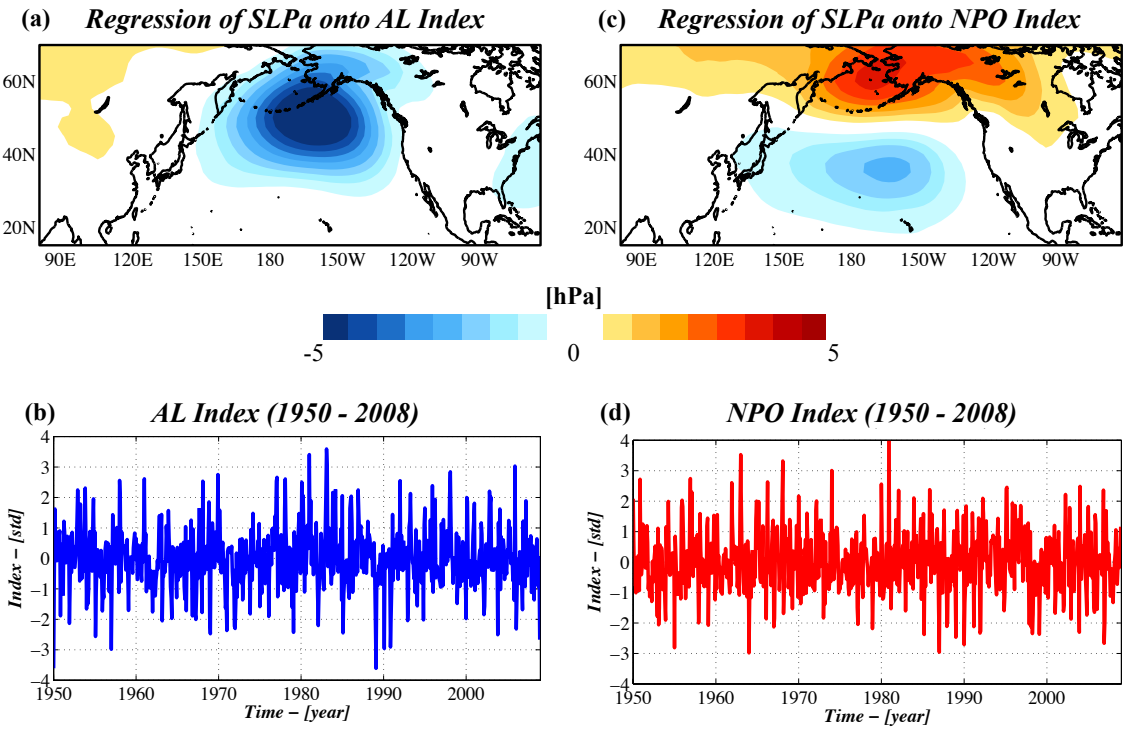

FIG. 1.3. (a) Regression of monthly-mean SLPa (hPa) onto the standardized AL index (defined as the first expansion coefficient (EC) time series of North Pacific boreal winter SLPa - see Section 2.2.2 for more details). (b) The AL index (standardized) from 1950 - 2008. (c) As in (a) but for regression onto the standardized NPO index (defined as the second EC time series of North Pacific boreal winter SLPa). (d) As in (b) but for the NPO index.

in pressure between Alaska and North America and the region just north of Hawaii (Fig. 1.3c). This pattern is the characteristic pattern of the NPO, originally discovered by Walker and Bliss (1932), and it explains 14% of the total variance in monthly-mean North Pacific SLPa (16% for for boreal winter SLPa variability). Unlike the AL, the NPO has not been a heavily studied mode of variability, particularly until the early 2000s (Rogers (1981) is a notable exception). Yet, the mode is directly connected to downstream weather conditions in North America (Rogers 1981; Linkin and Nigam 2008) and serves as the atmospheric forcing pattern for the NPGO (Chhak et al., 2009). The NPO index is dominated by high frequency variability with little low-frequency variability readily evident in the time series (Fig. 1.3d).

1.1.3 Tropical Pacific SST Modes

The major modes of variability in the North Pacific are defined regionally but are connected dynamically to the leading modes of the tropical Pacific Ocean. The dominant mode of tropical Pacific SSTa variability is El Niño - the oceanic component of ENSO involving changes in the steep zonal SST gradient in the equatorial Pacific. Bjerknes (1966) formulated the first general hypothesis for ENSO: anomalous warming of the eastern tropical Pacific weakens the zonal SST gradient, which consequently weakens the trade winds. The weakened trade winds decrease the wind stress forcing which reduces upwelling in the central and eastern equatorial Pacific. This reduction in upwelling leads to a weakened zonal SST gradient, generating a positive feedback. Consequently, the shift in warm waters to the eastern Pacific provides low-level instability that generates anomalous rising motion and convection, shifting heavy rains from its climatological position in the West Pacific Warm Pool to the east during a positive (i.e., warm SSTa in the eastern tropical Pacific) ENSO event. Bjerknes's work was followed by other studies by Wyrtki (1975) and Rasmusson and Carpenter (1982) which looked more in-depth into the evolution of ENSO events. No

one theory on the evolution and excitement of ENSO events exist, though the delayed oscillator model (Schopf and Suarez, 1987; Battisti, 1988; Suarez and Schopf, 1988; Battisti and Hirst, 1989) and the recharge/discharge mechanism (Jin, 1997) are two popular hypotheses.

Figure 1.4 presents an overview of the canonical signature of ENSO in the SST (Fig. 1.4a) and SLP (Fig. 1.4b) fields through regression onto the NINO3 index, the area-averaged SSTa in the region bounded by 5°S - 5°N and 150°W - 90°W. In the SSTa regression field (Fig. 1.4a), the positive phase of ENSO is displayed - anomalously warm SSTa encompass the Pacific cold tongue region in the central tropical Pacific and extends eastward toward the South American coast. Surrounding the warm SSTa is a horseshoe-shaped region of cool SSTa (e.g., Wallace et al. 1998), with the center of cooling in the West Pacific Warm Pool, then branching into the subtropical North and South Pacific Oceans. The SSTa pattern in the North Pacific resembles that of the PDO (Fig. 1.2a), indicating a relationship between ENSO variability and the PDO. The atmospheric signature of ENSO shows a weakening of the Walker circulation, creating anomalous rising motion in the central and eastern Pacific Ocean and consequently convection (Fig. 1.4b). In turn, the western tropical Pacific experiences anomalous subsidence and consequently drier conditions. In the North Pacific, ENSO projects onto the AL, thus impacting Northern Hemisphere storm tracks and the position of the mid-latitude jet stream.

While ENSO may be considered the largest signal in the climate system, the phenomenon varies in strength and spatial structure, altering its effect on the extratropical and tropical atmospheric circulation. Recently, Ashok et al. (2007) noted another "flavor" of ENSO that has become more frequent in the last two decades - the El Niño-Modoki phenomenon, referred to herein as Central Pacific Warming (CPW) or Central Pacific El Niño. Rather than the warmest SSTa being located in the eastern equatorial Pacific Ocean (e.g., Fig. 1.4a), the maximum warming during

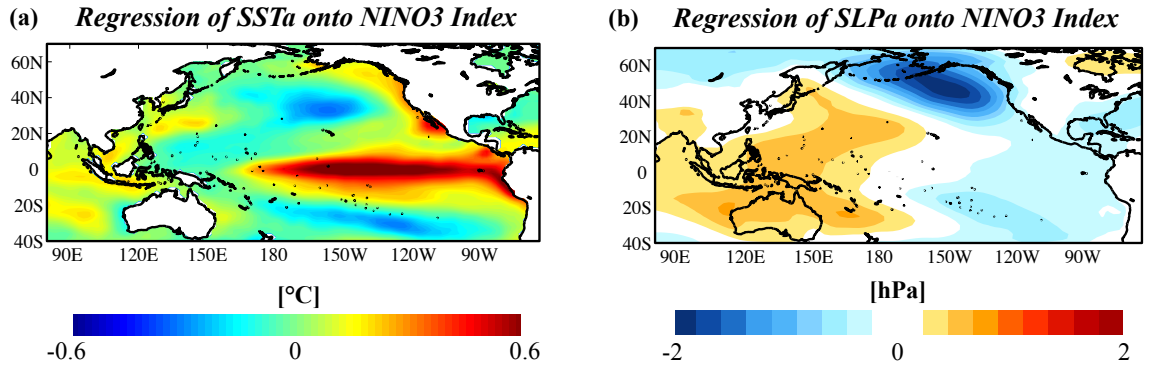

FIG. 1.4. (a) Regression of December - February (DJF) SSTa (°C) onto the standardized NINO3 index. (b) Regression of DJF SLPa (hPa) onto the standardized NINO3 index.

CPW events is concentrated in the central tropical Pacific Ocean, flanked by negative SSTa in the eastern and western equatorial Pacific Ocean (Figure 1.5a). In the North Pacific, the SST response is quite similar to that of the canonical ENSO, with a PDO-like response (compare the North Pacific sectors of Figs. 1.4a and 1.5a). Despite this similarity in the North Pacific SSTa, the atmospheric teleconnection pattern associated with CPW events differs substantially from the traditional El Niño events. Fig. 1.5b shows that in the North Pacific, the SLPa response to the CPW phenomenon is a dipole in pressure similar to that of the NPO, not a projection onto the AL as during canonical ENSO events. In the tropical Pacific, the weakening of the Walker cell is still apparent, but the negative SLPa center is moved to the west, closer to the axis of maximum warming. Ashok et al. (2007), Weng et al. (2007), Ashok et al. (2009), and Weng et al. (2009) highlight more teleconnection patterns associated with the CPW phenomenon, including its impacts on the east Asian monsoon and Southern Hemisphere storm tracks.

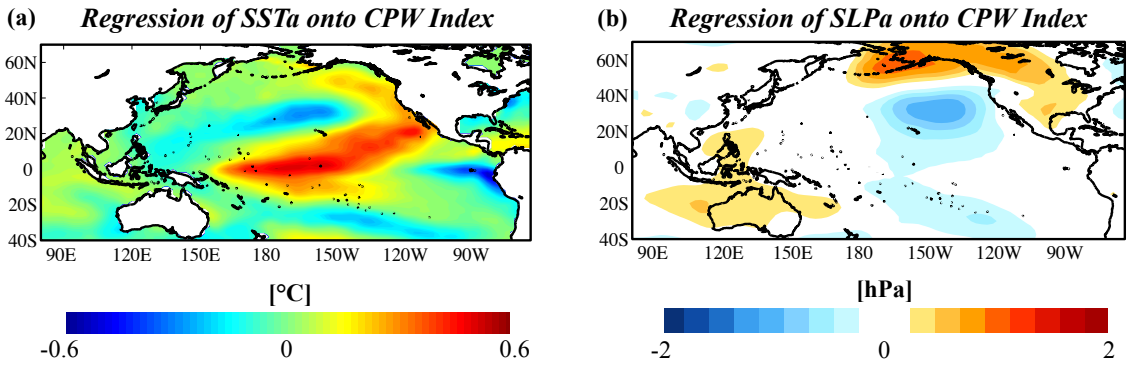

FIG. 1.5. (a) Regression of DJF SSTa (°C) onto the standardized CPW index (defined in Section 3.2.3). (b) Regression of DJF SLPa (hPa) onto the standardized CPW index.

1.2 Mechanisms Linking Tropical Pacific and North Pacific Modes of Climate Variability

Having introduced the major patterns of climate variability in the North Pacific and tropical Pacific Ocean, we now turn to examining how these modes, though regionally defined, can physically impact variability elsewhere in the Pacific Ocean and even globally. Several mechanisms linking tropical Pacific Ocean and North Pacific Ocean interannual and decadal variability have been proposed, with atmospheric-only pathways (e.g., Barnett et al. 1999; Alexander et al. 2002) and coupled oceanic-atmospheric pathways (e.g., Gu and Philander 1997; Knutson and Manabe 1998; Kleeman et al. 1999; Schneider et al. 1999). For the purposes of this dissertation, only two mechanisms are highlighted in detail, as these mechanisms are directly related to results presented. Liu and Alexander (2007) offer a more comprehensive review of the mechanisms linking tropical Pacific - North Pacific interannual and decadal variability and associated global climate teleconnections.

1.2.1 The Atmospheric Bridge

Alexander et al. (2002) analyzed the teleconnections associated with the ENSO phenomenon and termed the mechanism through which tropical Pacific variability alters extratropical circulation as the "atmospheric bridge." Figure 1.6 summarizes the

atmospheric bridge mechanism. Though Alexander et al. (2002) considered impacts of ENSO in multiple locations, here we focus only on the effects in the North Pacific. During a warm ENSO event, anomalous warming in the eastern tropical Pacific Ocean generates anomalous convection. These convective towers rise in the eastern Pacific Ocean and alter the strength and mean position of the Hadley cell and Walker circulation. As such, wave generation and propagation from the tropics into the subtropics and extratropics is altered significantly. In particular, in the North Pacific, the atmospheric Rossby waves enhance the climatological Pacific storm track and strengthen the AL. The strengthening of the AL creates stronger warm air advection over the eastern North Pacific Ocean and enhances cold air advection originating from Russia and Alaska down into the central North Pacific Ocean. The increased cold (warm) air advection enhances the net ocean-to-atmosphere (atmosphere-to-ocean) surface heat fluxes (both sensible and latent heat fluxes; i.e., Q_{net} in Fig. 1.6), thus cooling (warming) the underlying ocean waters. This pattern of warming/cooling of SSTs is similar to the characteristic pattern of the positive phase of the PDO (see Fig. 1.2a). Furthermore, the anomalous wind stresses associated with the strengthened AL also drive anomalous southward Ekman transport via enhanced northwesterly and westerly winds in the central North Pacific, further cooling the waters in that region. These changes in the North Pacific are then able to feedback onto the overlying atmospheric circulation, generally maintaining or even enhancing the observed atmospheric wavetrains in the extratropical Northern Hemisphere.

1.2.2 The ENSO Precursor Pattern and the Seasonal Footprinting Mechanism

Several studies have examined precursor signatures in the atmosphere and ocean and optimal excitation patterns that may lead to and explain variability associated with ENSO (e.g., Penland and Sardeshmukh 1995; Gu and Philander 1997; Barnett et al. 1999; Kim and North 1999; Vimont et al. 2001, 2003; Anderson 2003;

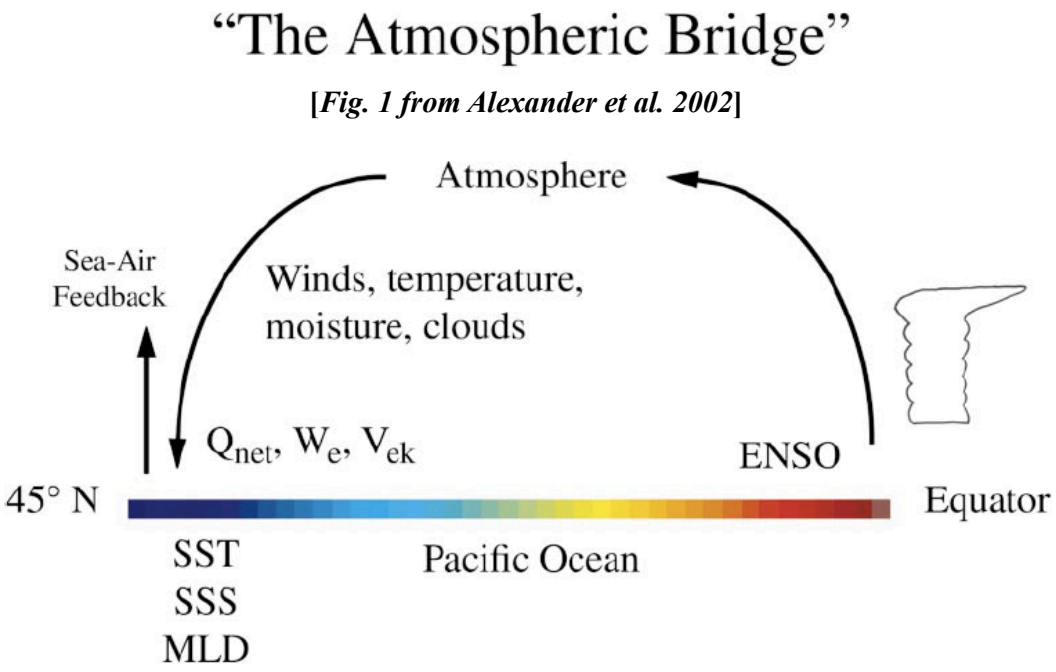

FIG. 1.6. Pictorial representation of the atmospheric bridge mechanism linking equatorial Pacific climate variability associated with ENSO to the extratropical North Pacific. In the diagram, Q_{net} refers to the net surface heat flux, w_e the entrainment rate into the mixed layer from the ocean below, V_{ek} the Ekman transport, SSS the sea surface salinity, and MLD the mixed layer depth. Adapted from Alexander et al. (2002).

Alexander et al. 2008). Figure 1.7 presents a schematic of one proposed mechanism: the *seasonal footprinting mechanism* (SFM; Vimont et al. 2001). The SFM links winter-to-winter atmospheric variability in the North Pacific atmosphere to tropical Pacific SSTa variability the following year. During the winter, stochastic atmospheric variability organizes into the NPO pattern which lays down a particular SSTa pattern generated from net surface heat fluxes driven by the atmospheric wind stresses. For the positive phase of the NPO, for example, the anticyclonic (cyclonic) circulation in the northern (southern) pole of the NPO generates negative SSTa in the central North Pacific contrasted with positive SSTa wrapping down the North American coast and southwestward across Hawaii and into the central tropical Pacific (shading in Fig. 1.7). This SSTa pattern constitutes the optimal excitation pattern detailed by Penland and Sardeshmukh (1995). Thus, during the winter, the ocean is enslaved to the overlying

atmospheric forcing. As the spring and summer seasons evolve, the NPO pattern in the North Pacific fades, but the SST pattern originally generated in the winter remains. With the lack of atmospheric forcing, the subtropical SSTa then *forces the overlying atmosphere* through anomalous heat fluxes. The instability generated by anomalous warming of subtropical North Pacific and central tropical Pacific drives convection, and through coupled ocean-atmosphere dynamics can potentially excite an ENSO event. Vimont et al. (2009) use a model forced with NPO-related heat flux anomalies to explicitly show that the tropical Pacific circulation indeed evolves according to the SFM and the wind-evaporation-SST (WES) feedback.

While the SFM relies on the WES feedback for its evolution, Anderson and Maloney (2006) take a different take on the ENSO precursor pattern. The authors find that tropical Pacific anomalies are indeed related to an NPO-like SLPa pattern in the North Pacific one year prior, but this SLPa pattern is also concurrent with the deepening of the average tropical Pacific isotherm depths. The deepening of the thermocline in the eastern Pacific rapidly warms the SSTs and can lead to an ENSO event. This evolution of the SSTs follows the recharge/discharge mechanism for ENSO evolution (Jin, 1997).

1.3 Motivation for Research and Research Goals

This dissertation aims to improve our understanding of NPDV and tropical-extratropical Pacific climate variability at interannual, decadal, and even multi-decadal timescales. In particular, three key motivating factors for this research are highlighted below.

- *A Better Understanding of the NPO.* The NPO appears as the second leading mode of North Pacific SLPa but serves several other important roles in the climate system: (a) as the SLPa pattern associated with the ENSO precursor

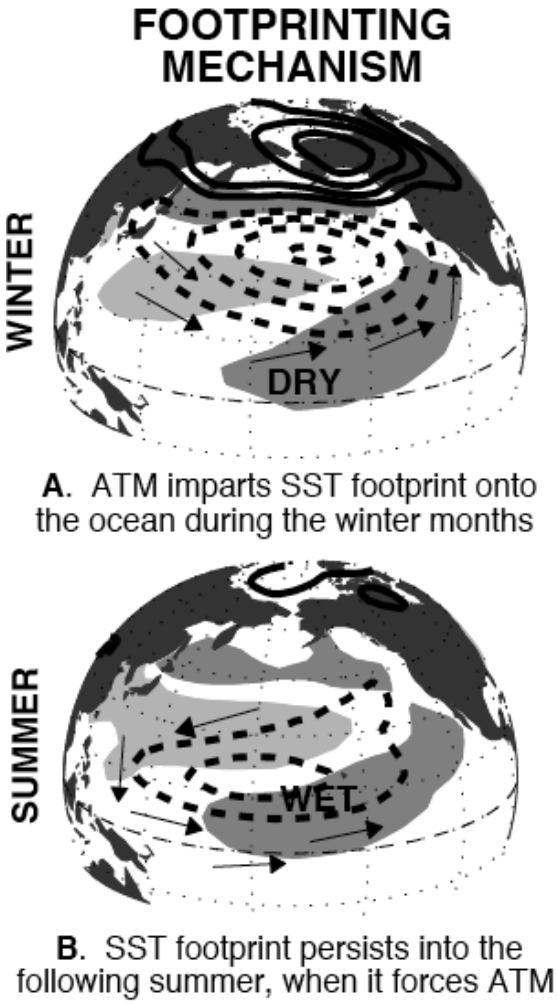

[*Fig. 4 from Vimont et al. 2001*]

FIG. 1.7. Schematic of the seasonal footprinting mechanism during the (top) winter and (bottom) summer. Contours denote SLPa (solid (dashed) contours denote positive (negative) SLPa), while shading denotes SSTa (dark (light) shading denotes positive (negative) SSTa). The vectors in the diagram illustrate the anomalous wind stress imposed on the ocean while text ("DRY" and "WET") refer to anomalous precipitation responses. Adapted from Vimont et al. (2001).

pattern / SFM (e.g., Vimont et al. 2001; Anderson 2003); (b) as the atmospheric driver for the NPGO (Chhak et al., 2009); and (c) as a pattern of climate variability associated with teleconnections that impact North American weather and climate (e.g., Rogers 1981; Linkin and Nigam 2008). The multiple roles of the NPO heighten the importance of understanding the dynamics associated with it. Prevailing knowledge suggests this mode is wholly stochastic and thus

unpredictable. However, given that one node of the NPO resides in the subtropical North Pacific Ocean, close to the tropics and influenced strongly by changes in the Hadley cell associated with ENSO, the individual nodes of the NPO may behave differently.

- *The Roles of the NPO, NPGO, and CPW in Pacific Decadal Climate Variability.* The current prevailing paradigm of North Pacific - tropical Pacific decadal and multidecadal variability centers around three key modes: ENSO, the AL, and the PDO. Figure 1.8 summarizes a simplified[2] framework of North Pacific - tropical Pacific connections, with the mechanisms and modes of variability depicted. In Fig. 1.8, the "start" of the loop is likely with the stochastic variability of the extratropical North Pacific atmosphere, which can excite ENSO (e.g., Barnett et al. 1999; Vimont et al. 2001, 2003; Anderson 2003; Anderson and Maloney 2006). Yet, as shown earlier, the second leading modes of variability in tropical Pacific SSTs (the CPW) and in the extratropical North Pacific atmosphere and ocean (the NPO and the NPGO) project uniquely onto the global climate system and thus will potentially have different impacts and feedbacks on sensible weather and long-term climate change. Where these modes fit into the larger picture of Pacific decadal climate variability is not represented in Fig. 1.8.

- *Uncertainty in the Future Climate State for the Pacific.* With recent focus on the impacts of anthropogenic greenhouse forcing on the climate of Earth, the question of changes in structure, magnitude, and frequency of the dominant modes of variability of the North Pacific and tropical Pacific are central to global

[2]The framework discussed in this dissertation is highly simplified from the actual North Pacific ocean-atmosphere climate system. For example, it does not discuss the roles of several oceanic "tunnels" or the effects of decadal-scale changes in the Kuroshio Current on the North Pacific ocean circulation, the SST field, and the subsequent atmospheric response through surface heat fluxes (e.g., Taguchi et al. 2007; Ceballos et al. 2009).

climate change because of their vast global influences. Because of the intimate relationship between ENSO, the PDO, and the North Pacific extratropical atmosphere, and the substantial impacts that North Pacific climate variability have on biological systems in the basin, constraining the range of uncertainty in the future states of these modes is important to evaluate and better quantify.

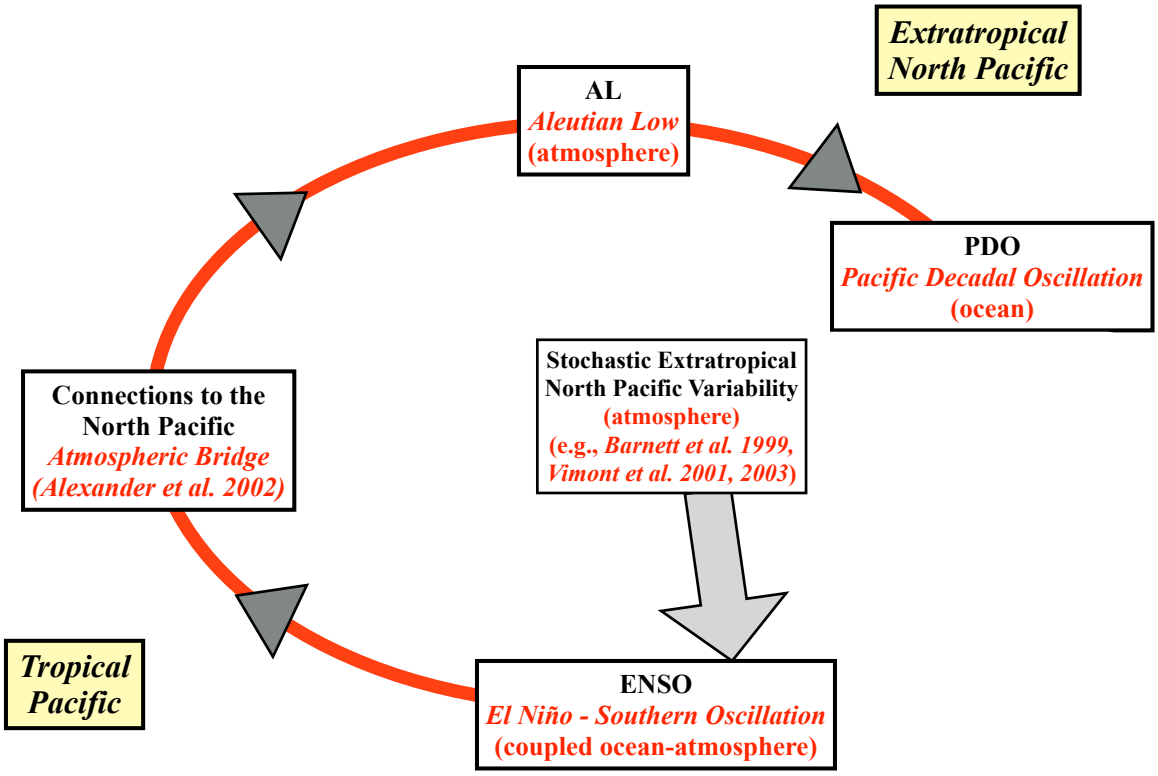

FIG. 1.8. The current simplified framework depicting links between major modes of variability and mechanisms associated with tropical Pacific and North Pacific interannual and decadal climate variability.

Given these motivating factors, the following are the goals of the work presented in this dissertation:

1. *Explore the fundamental characteristics and dynamics of the NPO, including those its individual poles and their frequency content (i.e., high frequency vs. low frequency variability).*

2. *Assess further the relationships between the CPW, the NPGO, and the NPO,*

particularly since the NPO pattern shares variance with the NPGO and the CPW phenomena.

3. *Build a similar framework to that in Fig. 1.8 that includes the CPW, NPO, and the NPGO along with appropriate connections/mechanisms.*

4. *Evaluate how state-of-the-art coupled climate models capture and represent the leading modes of NPDV and tropical Pacific variability and what future changes are projected for these modes.*

5. *Examine the degree of importance of the CPW phenomenon in reconstruction techniques for tropical SST fields using paleoclimate records.*

1.4 Outline of the Dissertation

This dissertation presents analyses and results that collectively address the five goals outlined in the previous section. Chapter 2 presents an overview of the major datasets used and general statistical methods common to analyses throughout the dissertation. Chapter 3 then presents an in-depth investigation and characterization of the NPO both spatially and also in frequency space. Results include experiments from a simple atmospheric general circulation model (AGCM) forced by tropical Pacific SSTs only to quantify the degree to which NPO variability is tied to tropical Pacific SSTa. With these results, a new viewpoint of NPDV/tropical Pacific variability emerges. Chapter 4 invokes this new framework and explores the representation of NPDV in the 24 models used in the IPCC AR4, both in frequency and space. Chapter 5 then explores optimal methods of reconstructing tropical Pacific SSTs using paleoclimate proxy networks. As shown, the optimal reconstructions result from methods that include not only the traditional ENSO signature but also that of the CPW phenomenon (among other higher order modes). This application directly shows the

importance of the variability of the CPW in representing earlier climate conditions and consequently in understanding future climate change in the Pacific basin. Chapter 6 then presents a summary of the dissertation with overall conclusions and ideas for future work.

CHAPTER II

DATA AND GENERAL METHODOLOGY

2.1 Data and Models

2.1.1 Observational Datasets

Observational datasets of atmospheric and oceanic variables used throughout the dissertation are primarily from reanalysis projects. For atmospheric variables, we use the National Centers for Environmental Prediction/National Center for Atmospheric Research (NCEP/NCAR) Reanalysis Project (Kistler et al., 2001). Variables of interest from the NCEP/NCAR Reanalysis are SLP and streamfunction, which reside on a 2.5° by 2.5° horizontal grid and 17 vertical pressure levels, ranging non-uniformly from 1000 to 10 hPa. The data span 1950 - 2008 and are monthly-mean values. SSTs are are taken from the National Oceanic and Atmospheric Administration Extended Reconstruction SST dataset (NOAA ER SSTs), version 3 (Smith et al., 2008). The monthly-mean SST values from the NOAA ER SSTs are gridded on a 2 ° by 2 ° global horizontal grid. The data used in the analyses span 1950 - 2008 and are monthly-mean values.

Observational precipitation data used in Chapter 5 originate from two sources. The Climate Prediction Center Merged Analysis of Precipitation (CMAP) dataset, which combines in situ rain gauge measurements and satellite-derived estimates of precipitation (Xie and Arkin, 1997), is one of them. The CMAP data are on a 2.5° by 2.5° horizontal grid globally and extend back to 1979. For this study, the "non-enhanced" version of the CMAP dataset is used (i.e., no assimilated data from numerical model output). A second observational precipitation dataset used is the 40-yr European Centre for Medium-Range Weather Forecasts Re-Analysis (ERA-40)

(e.g., Simmons and Gibson 2000). These data are interpolated onto a 2.5° by 2.5° horizontal grid globally, and the dataset extends from 1957 - 2002.

2.1.2 Models

2.1.2.1 The International Centre for Theoretical Physics (ICTP) Model

Model experiments for testing the influence of tropical Pacific SST variability on the NPO and NPGO (Chapter 3) and for generating precipitation fields for SST reconstructions (Chapter 5) are done using the International Centre for Theoretical Physics (ICTP) AGCM, also known as "SPEEDY" (**S**implified **P**arameterization, primitiv**E**-**E**quation **DY**namics). The model atmosphere consists of eight vertical layers and T30 horizontal resolution (3.75° by 3.75° on a longitude/latitude grid). The physical parameterizations of the model are described in Molteni (2003), and prior applications of the model in various configurations can be found in Bracco et al. (2006), Kucharski et al. (2006), and Kucharski et al. (2007). The model can be run with two different lower boundary conditions for the ocean: (1) with prescribed SSTa forcing the atmosphere; or (2) with a slab ocean; i.e., an interactive mixed layer with constant depth. Details on specific experiments and configurations used for the various analyses are provided in Chapters 3 and 5.

2.1.2.2 IPCC Models

For analysis of NPDV in coupled climate models, we use the 24 coupled climate models that were analyzed in the IPCC AR4 (Table 2.1). These models are all part of the Coupled Model Intercomparison Project Phase 3 (CMIP3), but will be referred to as the "IPCC models" in this work. The model output is available for downloading and processing through FTP or OPeNDAP from the Program for Climate Model Diagnosis and Intercomparison (PCMDI) at the Lawrence Livermore

National Laboratory[3]. We use the 20C3M scenario (i.e., greenhouse gas concentrations increase throughout the 20$^{\text{th}}$ century as in observations) to represent the 20$^{\text{th}}$ century climate and the SRESA1B scenario (i.e., atmospheric CO_2 levels increase to 720 parts per million by 2100 and are stabilized at that level thereafter) to represent the 21$^{\text{st}}$ century climate. More details on the variables used and specific methods of analysis for the IPCC model output is reserved for Chapter 4.

2.2 General Methodology and Statistical Techniques

This section highlights the major statistical techniques and methods used throughout the dissertation and provides background on them. Common to all analyses, monthly-mean anomalies of the atmospheric or oceanic field of interest are employed. Anomalies are computed by subtracting the climatological monthly-mean value at each grid point from the raw field. All anomalies are also linearly detrended to eliminate the influence of trends on the underlying statistical and inferred dynamical relationships among variables.

2.2.1 Linear Regression Analysis

For two arbitrary time series $x(t)$ and $y(t)$, the approximation of $y(t)$, using $x(t)$ as a linear predictor, can be written as

$$y(t) = \hat{y}(t) + \epsilon(t) = a_o + a_1 x(t) + \epsilon(t) \tag{2.1}$$

where $\hat{y}(t)$ denotes a linear approximation between $x(t)$ and $y(t)$, and ϵ is the error in this approximation (e.g., Wilks 2006). The optimal choices for a_o and a_1 are those

[3]More information on the program is available at `http://www-pcmdi.llnl.gov/`.

Table 2.1. List of IPCC AR4 models analyzed in this study, along with the number of realizations available for processing for both the 20C3M and SRESA1B scenarios.

Originating Group, Country	***Model Name***	***Realizations (20C3M / SRESA1B)***
Bjerknes Centre for Climate Research, Norway	BCCR-BCM2.0	1/1
Canadian Centre for Climate Modeling and Analysis, Canada	CGCM3.1 (T47)	5/5
Canadian Centre for Climate Modeling and Analysis, Canada	CGCM3.1 (T63)	1/1
Météo-France/Centre National de Recherches Mtorologiques, France	CNRM-CM3	1/1
CSIRO Atmospheric Research, Australia	CSIRO3.0	3/1
CSIRO Atmospheric Research, Australia	CSIRO3.5	1/1
NOAA Geophysical Fluid Dynamics Laboratory, United States of America	GFDL2.0	3/1
NOAA Geophysical Fluid Dynamics Laboratory, United States of America	GFDL2.1	3/1
NASA Goddard Institute for Space Studies, United States of America	GISS-AOM	2/2
NASA Goddard Institute for Space Studies, United States of America	GISS-EH	5/3
NASA Goddard Institute for Space Studies, United States of America	GISS-ER	9/5
Institute of Atmospheric Physics, China	IAP-FGOALS1.0	3/3
Instituto Nazionale di Geofisica e Vulcanologia & Max Planck Institute for Meteorology, Italy/Germany	INGV-ECHAM4	1/1
Institute of Numerical Mathematics, Russia	INMCM3.0	1/1
Institute Pierre Simon Laplace, France	IPSL-CM4	1/1
Center for Climate System Research, Japan	MIROC-HIRES	1/1
Center for Climate System Research, Japan	MIROC-MEDRES	3/3
Meteorological Institute of the University of Bonn & Meteorological Research Institute of KMA, Germany/Korea	MIUB-ECHO-G	5/3
Max Planck Institute for Meteorology, Germany	MPI-ECHAM5	4/4
Meteorological Research Institute, Japan	MRI-CGCM2.3.2	5/5
National Center for Atmospheric Research, United States of America	NCAR-CCSM3.0	8/7
National Center for Atmospheric Research, United States of America	NCAR-PCM1	4/4
Hadley Centre for Climate Prediction and Research / Met Office, United Kingdom	UK-HADCM3	2/1
Hadley Centre for Climate Prediction and Research / Met Office, United Kingdom	UK-HADGEM1	2/1

that minimize the mean square error (MSE; i.e., ϵ^2). Assuming that ϵ is Gaussian-distributed, the optimal choices are:

$$a_o = \bar{y} - a_1 \bar{x}, \tag{2.2}$$

$$a_1 = \frac{\overline{x'y'}}{\overline{x'^2}}. \tag{2.3}$$

where overbars denote means; i.e.,

$$\overline{(\ )} = \frac{\sum_{i=1}^{N} (\ )}{N}, \tag{2.4}$$

(N is the total number of samples), and primes denote departures from the mean; i.e.,

$$(\ )' = (\ ) - \overline{(\ )}. \tag{2.5}$$

a_1 is called the *regression coefficient* and describes the slope of the linear relationship between the two variables (i.e., the change in y per unit change in x). If x is standardized, then the units of the regression coefficient are the units of y per standard deviation in x.

2.2.1.1 Statistical Significance of Regression and Correlation Coefficients

(2.1) provides an estimate for predicting $y(t)$ linearly based only on $x(t)$. However, deriving (2.1) does not necessarily mean the relationship is "statistically significant." That is, (2.1) could describe a relationship between two time series that occurs simply by chance. In order to determine the statistical significance of the linear relationship between $x(t)$ and $y(t)$, we evaluate the statistical significance of the correlation coefficient, r:

$$r = a_1 \frac{\sqrt{\overline{x'^2}}}{\sqrt{\overline{y'^2}}}. \tag{2.6}$$

Note that the square of r tells us the fraction of the total variance of $y(t)$ explained by (2.1).

Two methods for assessing the statistical significance of the correlation coefficient are used in this study:

1. *The t-statistic*: The t-statistic is defined as:

$$t = \frac{r\sqrt{N_{eff} - 2}}{\sqrt{1 - r^2}} \tag{2.7}$$

where N_{eff} is the effective sample size. N_{eff} is used instead of the total sample size, N, to account for persistence in the dataset. The larger the difference between N and N_{eff}, the more persistence the dataset contains. To calculate N_{eff}, we use the equation derived by Bretherton et al. (1999):

$$N_{eff} = N\frac{1 - r_1 r_2}{1 + r_1 r_2} \tag{2.8}$$

where r_1 and r_2 are the lag-1 autocorrelations of $x(t)$ and $y(t)$, respectively.

2. *The Bootstrap Method*: Another method of significance testing for correlations in time and space is the bootstrap approach (e.g., Wilks 2006). The original time series are decomposed into their Fourier series, and subsequently 2000 red-noise time series with the same lag-1 correlation coefficient are simulated. However, for each red-noise time series, the phases of the original time series are randomized. The probability density function (PDF) of the cross-correlation between those simulated series is then computed. Desired significance levels (e.g., the 95% and 99% significance levels) are found by computing the area under the PDF and comparing those values to the cross-correlation between the two time series in question to accept or reject the null hypothesis (i.e., $r = 0$).

The determination of significance of a correlation coefficient in space or time is insensitive to which method is chosen.

2.2.2 EOF and Combined EOF Analysis

The major large-scale patterns of climate variability in the atmosphere and ocean are characterized and defined by performing EOF analysis on the atmospheric and oceanic variables. Traditional EOF analysis aims to break a large dataset with many state vectors, represented by $\mathbf{A}$, into a smaller set of state vectors that explains a large fraction of the variability in the original dataset (e.g., Wilks 2006). With combined EOF (cEOF) analysis, two or more variables are placed into $\mathbf{A}$, which is subsequently decomposed using singular value decomposition (SVD; e.g., Bretherton et al. 1992).

With SVD, $\mathbf{A}$ can be factored into three distinct matrices:

$$\mathbf{A} = \mathbf{U}\mathbf{\Sigma}\mathbf{V}^T \tag{2.9}$$

where the columns of $\mathbf{U}$ are the eigenvectors of $\mathbf{A}\mathbf{A}^T$, the columns of $\mathbf{V}$ are the eigenvectors of $\mathbf{A}^T\mathbf{A}$ ($\mathbf{U}$ and $\mathbf{V}$ are orthogonal), and the diagonal of $\mathbf{\Sigma}$ contains the square roots of the non-zero eigenvalues of $\mathbf{A}^T\mathbf{A}$ and $\mathbf{A}\mathbf{A}^T$. As an example, for traditional EOF analysis, the columns of $\mathbf{U}$ represent the principal component (PC) time series (i.e., temporal eigenvectors), and the columns of $\mathbf{V}$ are the EOFs (i.e., spatial eigenvectors) associated with each PC time series. The first EOF (EOF-1; i.e., the first column is $\mathbf{V}$) is called the leading EOF and is the spatial pattern that explains the largest fraction of variability in the dataset. Subsequent EOFs explain successively lower fractions of variability. The PC time series represents the temporal evolution of each individual EOF pattern. For example, the first column of $\mathbf{U}$ (the leading PC time series) describes the temporal evolution of the leading EOF.

EOFs/cEOFs and PCs alone have arbitrary amplitude and are dimensionless. A convenient way to present EOFs is by regressing the original data onto standardized values of the respective PC time series. The spatial pattern that emerges then has units of the original data and illustrates a pattern of variability in the dataset.

Furthermore, to obtain a time series representing a particular EOF-pattern but for a longer time period than that performed in the EOF analysis, expansion coefficient (EC) time series can be computed by projecting raw individual monthly-mean anomaly maps onto the EOF/cEOF spatial pattern of interest.

2.2.3 Power Spectrum Analysis

In climate dynamics, time series analyses involve not only regression and correlation, but also the study of the periodicity of atmospheric and oceanic phenomenon. One convenient method for this analysis is *power spectrum analysis*, which aims to decompose a given time series into linear combinations of sine and cosine waves with various frequencies. The following offers a brief overview of power spectrum analysis and follows closely the description provided by Hartmann (cited 2010).

The discrete Fourier expansion of a time series $y(t)$ is:

$$y(t) = \frac{1}{2}A_o + \sum_{k=1}^{N/2}\left[A_k \cos\left(\frac{2\pi kt}{T}\right)\right] + \sum_{k=1}^{N/2}\left[B_k \sin\left(\frac{2\pi kt}{T}\right)\right] \tag{2.10}$$

where k is the "wavenumber," N is the total number of timesteps in the time series, t is an individual time step, and T is the total time length. (2.10) illustrates that each predictor (i.e., each cosine and sine wave) is a harmonic function that has a frequency $\omega = k/T$. The frequency $\omega = \dfrac{N}{2T}$ is the highest possible frequency that can be resolved in the dataset and is known as the *Nyquist frequency*. From (2.10), for a given k, a cosine and sine wave are being fitted with variable amplitude. This is equivalent to fitting a cosine wave with variable amplitude and variable phase. Regardless, for both cases, there are two predictors used for k.

The objective of using power spectrum analysis is ultimately to produce a plot of the amplitude of the total wave,

$$\frac{C_k^2}{2} = \frac{A_k^2 + B_k^2}{2}, \tag{2.11}$$

which is equivalent to the variance explained or the "energy" of the signal at that

wavenumber. Employing the Discrete Fourier Transform, the coefficients, A_k and B_k, are obtained from the following equations:

$$A_k = \frac{2}{N}\sum_{n=1}^{N} y_n \cos\left(\frac{2\pi kn\Delta t}{T}\right), \tag{2.12}$$

$$B_k = \frac{2}{N}\sum_{n=1}^{N} y_n \sin\left(\frac{2\pi kn\Delta t}{T}\right), \tag{2.13}$$

$$A_{N/2} = \frac{1}{N}\sum_{n=1}^{N} y_n \cos\left(\frac{\pi Nn\Delta t}{T}\right), \tag{2.14}$$

$$A_o = \overline{y}. \tag{2.15}$$

The numerical computation of power spectra typically uses the Fast Fourier Transform (FFT) to calculate C_k^2. Such packages, however, assume that the time series is cyclic and thus imposes cyclic continuity in processing the signal. This assumption leads to "spectral leakage" at the endpoints. To reduce this effect, in this study all power spectra are computed using a *Hanning window* ($w(t)$):

$$w(t) = \begin{cases} \frac{1}{T}\left[1 + \cos\left(\frac{2\pi t}{T}\right)\right] & \text{if } 0 \le |t| \le \frac{T}{2} \\ 0 & \text{if } |t| > \frac{T}{2}, \end{cases} \tag{2.16}$$

which tapers the ends of the time series before applying FFT and reduces spectral leakage.

The null hypothesis for power spectrum analysis is that of a red noise process with a power spectrum $\Phi(\omega)$ given by:

$$\Phi(\omega) = \frac{2R}{1 + R^2\omega^2}, \tag{2.17}$$

where $R = -\dfrac{\Delta t}{\ln r_1}$ and r_1 is the lag-1 autocorrelation of $y(t)$. To assess the significance of peaks in our power spectra versus the null hypothesis, we use the method outlined in Torrence and Compo (1998) and Hartmann (cited 2010). A mean normalized red-noise spectrum (i.e; (2.17)) is calculated for the particular index, and the 95% confidence spectrum is then found by multiplying $\Phi(\omega)$ by the appropriate F-statistic. Only peaks exceeding the significance spectrum are considered significant.

Significance of the peaks also depends on the number of degrees of freedom present in the power spectrum of interest. Spectral estimates inherently have 2 degrees of freedom associated with them. Hartmann (cited 2010) provides the following empirical formula for calculating the degrees of freedom (ν) in a power spectrum:

$$\nu = \frac{N}{M^*} \tag{2.18}$$

where M^* represents the number of individual spectral estimates. To increase the degrees of freedom in our power spectrum, we seek ways to decrease M^*, thus increasing ν. Two accepted methods to reduce M^* are:

1. *Averaging multiple realizations of the power spectrum together.* This technique requires that the original time series be divided into a number of sub-series, and power spectrum analysis be performed on each sub-series. The final power spectrum is then obtained by averaging together the individual spectra. Dividing the time series into x sub-series increases ν x-fold. However, the disadvantage of this method is that, as length of the sub-series decreases, so does the ability to capture low-frequency variability.

2. *Averaging adjacent spectral estimates together.* This method simply employs using a running mean on the values of the power spectrum. Doing an x-point running mean will increase ν x-fold, but the bandwidth on the frequency axis is reduced x-fold. Furthermore, one loses the highest and lowest resolvable frequencies in the time series.

In this study, both methods above are used to increase degrees of freedom for statistical significance testing.

CHAPTER III

THE DYNAMICS OF THE NORTH PACIFIC OSCILLATION AND ITS CONNECTION TO CENTRAL PACIFIC WARMINGS AND PACIFIC DECADAL VARIABILITY

3.1 Introduction

The prevailing paradigm of Pacific decadal climate variability centers around two prominent patterns in the Pacific: ENSO in the tropical Pacific and the PDO in the North Pacific (Mantua et al., 1997). The chain of events linking ENSO to the PDO goes as follows. Through changes in equatorial Pacific SSTs, ENSO induces changes in tropical Pacific convection patterns and thus alters the extratropical wintertime atmospheric circulation via changes in Rossby wave source regions. In particular, through teleconnections associated with the atmospheric bridge mechanism (Alexander et al., 2002) wintertime storm tracks in the North Pacific are altered in location and magnitude, thus affecting the strength and position of the AL. The PDO is directly linked to variability in the AL (e.g., Miller et al. 2004; Chhak et al. 2009). Also known as the North Pacific "long-lived El Niño" (Zhang et al., 1997), the PDO is likely the result of the integration of multiple modes of variability, both internal to the ocean as well as forced by the atmosphere, that produce this multi-decadal oceanic mode (e.g., Schneider and Cornuelle 2005). Like ENSO, the PDO is also associated with teleconnections which impact precipitation and temperatures across primarily North America (Mantua et al., 1997).

Recently, impacts of climate change in the North Pacific and tropical Pacific

have excited other modes of variability in the Pacific, providing potential new influences upon Pacific decadal variability. In the tropical Pacific Ocean, Ashok et al. (2007) recently identified the CPW phenomenon, formally defined as the second leading mode of tropical Pacific SSTa. The CPW phenomenon exhibits warm SSTa in the central tropical Pacific flanked by negative anomalies in the eastern and western equatorial Pacific Ocean. This mode contrasts strongly with "canonical" ENSO episodes, during which the axis of maximum positive SSTa exists closer to the South American coast. Because of its relatively new identification in the climate literature, mechanisms and dynamics related to CPWs remain unresolved. However, the projected increase in frequency and magnitude of CPW events under greenhouse warming in coupled climate models (Yeh et al., 2009) emphasizes the need to better understand this mode.

As with the canonical ENSO feature, CPWs are also related to extratropical North Pacific atmospheric variability. Correlation analyses done by Ashok et al. (2007) indicate that the CPW phenomenon is linked to SLP fluctuations in the subtropical North Pacific, particularly near Hawaii. Anderson (2003, 2007) offers similar connections between tropical Pacific SSTa variability and North Pacific subtropical SLPa variations. These variations in the subtropical North Pacific atmosphere are also tied into the variability of the NPO, as its southern node resides there (e.g., Walker and Bliss 1932; Rogers 1981).

Recent interest in the NPO has centered around two main topics. One topic is the role of the NPO in the SFM (Vimont et al., 2001, 2003) (see Section 1.2.2 for more details on the SFM). For the SFM, the NPO is thought of as an intrinsic mode of North Pacific atmospheric variability that organizes into a preferred pattern that drives the SSTa pattern that potentially excites an ENSO event. The other topic involves teleconnections across the Pacific and the Northern Hemisphere associated with the NPO. Rogers (1981) studied the impacts of the NPO on the position of the AL and

consequences for storm activity across the Pacific Ocean. The study noted that the NPO was the Pacific analog to the North Atlantic Oscillation (NAO), a pressure dipole between Iceland and the Azores, but unlike the NAO, "its [the NPO's] modes occur randomly in time" (Rogers, 1981), implying the NPO is stochastic in nature. In a subsequent study, Linkin and Nigam (2008) also noted that NPO variability operates only on small timescales (i.e., weeks to months), limiting its predictability.

Variability in the North Pacific SLP field, however, also has important implications for decadal-scale variations in the North Pacific, particularly in the subtropical North Pacific. In a recent paper by Di Lorenzo et al. (2010), we[4] illustrated, through a modeling experiment with the ICTP AGCM, that SLPa variability in the subtropical North Pacific is forced by tropical Pacific SSTa variability. Indeed, the subtropical North Pacific SLPa near Hawaii from the model are strongly correlated with the CPW index (Di Lorenzo et al., 2010). Moreover, the response of the extratropical SLPa field to the tropical Pacific forcing is then integrated by the underlying ocean to form the decadal-scale expression of the NPGO. The latter result was confirmed using a simple autoregressive model of order 1 (AR-1) model forced with SLPa near and to the east of Hawaii to reconstruct the NPGO index (see Figure 4 of Di Lorenzo et al. (2010)). Thus, there is substantial evidence that at least a portion of the NPO (i.e., the southern node) exhibits a deterministic component that is intimately tied to tropical Pacific SSTa variability, particularly that associated with the CPW phenomenon.

This chapter diagnoses further the dynamics of the NPO and shows that both nodes of the NPO are not alike. The subtropical node of the NPO has important low-frequency variability that is connected with both the CPW phenomenon and also the NPGO, while the northern node of the NPO is related to high frequency atmospheric variability. The chapter begins with an overview of the data, the model experiments,

[4]I am a co-author on this paper.

and statistical methods employed (Section 3.2). Then, Section 3.3 introduces some key characteristics of the CPW phenomenon, both spatially and temporally, and its link to the NPO. A detailed examination of the NPO and its individual poles in observations and the AGCM is presented in Section 3.4. Section 3.5 then decomposes the NPO and its poles into a high-frequency component and low-frequency component to illustrate the differences in strength and explanatory power of each pole. In particular, the observational analyses show that the high-frequency component of the NPO indices are connected with the ENSO precursor SSTa pattern, while the low-frequency component of the NPO SP in particular is related to low frequency changes in central tropical Pacific SSTa variability. A mechanism for the connections between the CPW and the extratropical North Pacific atmospheric circulation is then proposed in Section 3.6. Discussion of the results is offered in Section 3.7.

3.2 Analysis Techniques and Model Experiments

3.2.1 Observational Data

Atmospheric variables used in the study originate from the NCEP/NCAR Reanalysis Project (Kistler et al., 2001). Monthly-mean values of the variables from 1950 - 2008 are analyzed with a focus on boreal winter values (December - February; DJF) as this is the season when the climate patterns of interest are at their peak variability and intensity. SLP and streamfunction at 200 hPa are the atmospheric variables used. The only observed oceanic variable used in our analysis is SST from the NOAA ER SSTs (Smith et al., 2008).

3.2.2 ICTP AGCM Experiments

To test hypotheses on the connection between NPO variability and tropical Pacific SST forcing, two experiments are run with the ICTP AGCM. One experiment consists of the model forced by prescribed time-varying SSTa globally from 1950 -

2008 (herein referred to as the CONTROL run). This run depicts how well the model performs in recreating the various relationships associated with the NPO and SSTa. The second integration of the model is the same that was used by Di Lorenzo et al. (2010). The run uses prescribed time-varying SSTa over the equatorial Pacific Ocean (12°S - 12°N) only, while for the remainder of the ocean basins, the mixed layer model is used with constant depth of 50 m. For the mixed layer configuration, a heat flux climatology is generated from a previous integration of the model that is forced with the NOAA ER SSTs from 1950 - 2008. This experiment, which consists of 45 ensemble members, is referred to as the TROP run. Each ensemble member differs by randomizing the tropical Pacific SSTa forcing for the first two years of the integration, and then allowing the model to evolve thereafter. Hence, for both the CONTROL and TROP runs, we only use output from 1953 - 2008 for analysis to exclude the "spin-up" output. Statistics and results shown from the TROP runs are derived from the ensemble-mean statistics (i.e., statistics are computed for each ensemble member separately and then averaged together). This method of ensemble averaging allows us to retain both the signal from the tropical SSTa forcing and also some of the "noise" from each ensemble member.

3.2.3 Statistical Methods and Index Definitions

Indices of the two dominant modes of variability referenced in this paper, the NPO and the CPW, are defined as follows:

- *The NPO Index.* Vimont et al. (2003) define the NPO as the second leading EOF of November - March (NDJFM) North Pacific SLPa poleward of 15°N. While this definition is convenient, using an EOF-based definition for the AGCM runs is not ideal because the second leading EOF of the model SLPa fields may not have the same location for the poles as seen in the observations (or even necessarily be the same pattern as observed). To avoid this

problem, we define the NPO differently in this study. First, using observations, we compute EOF-2 of NDJFM North Pacific SLPa and produce the correlation map between NDJFM SLPa and the second PC time series. The two loading centers of the NPO are identified and used to define two additional indices: the NPO NorthPole (NPO NP) and NPO SouthPole (NPO SP) indices; i.e., the area-averaged monthly-mean SLPa within the nodes. Finally, the NPO index is defined simply as:

$$NPO(t) = NPO_{NP}(t) - NPO_{SP}(t) \tag{3.1}$$

Figure 3.1a illustrates the observed NPO signature obtained from correlating NDJFM SLPa with the NPO index defined in (3.1), along with gray boxes denoting the regions where the NPO NP and NPO SP are defined. The characteristic dipole of the NPO is clearly recovered using this method. Furthermore, the correlation between the NPO index computed using (3.1) and that from EOF analysis is $r = 0.98$, validating this approach. Figs. 3.1b and 3.1c show the NPO signature in the models, using the same regions as in Fig. 3.1a to construct the model NPO index. In general, the correlation maps between the two model runs match well with the observed NPO pattern (spatial correlations for the model maps compared to the observations is $r = 0.91$ for the ICTP CONTROL run and $r = 0.87$ for the ensemble-mean ICTP TROP runs).

- *The CPW Index.* In this study, the CPW index is defined as the second PC time series of monthly-mean tropical Pacific SSTa (20°S-20°N, 80°E - 60°W), similar to the definition used by Ashok et al. (2007).

Power spectrum analysis and filtering are the two primary techniques in isolating variability at different frequencies for the NPO and CPW. Power spectra are normalized so that values represent the percent of variance explained at a particular period, with the total area under the curve equal to 100%. Time series are subdivided

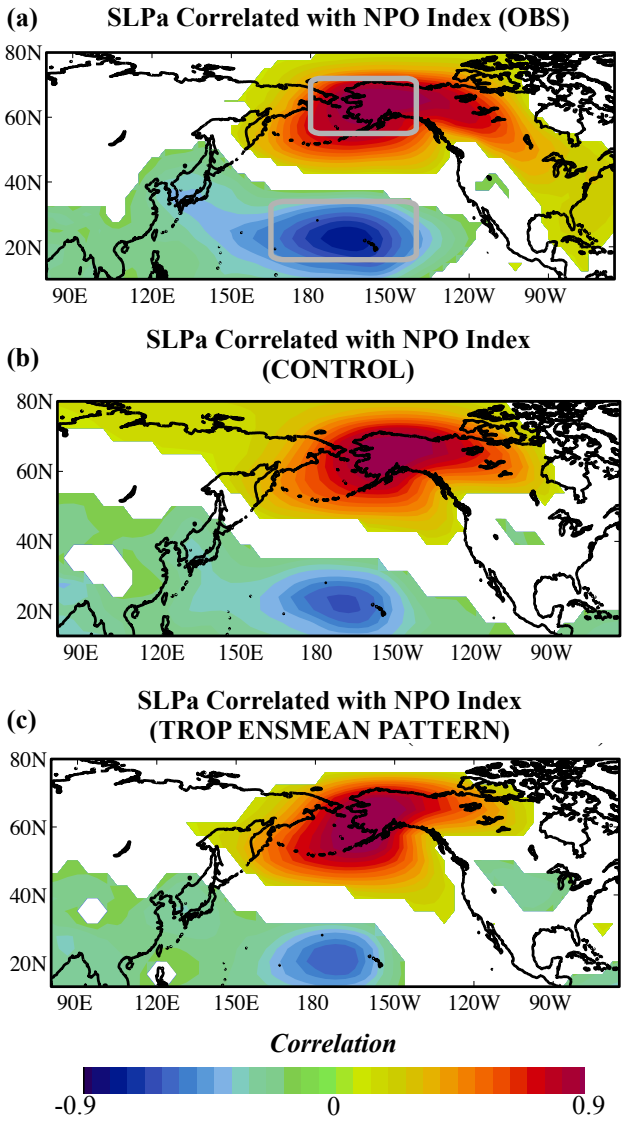

FIG. 3.1. (a) Correlation of observed DJF SLPa with the standardized NPO index from observations (see text for details). Gray boxes denote the locations of the area-averaged SLPa used to compute the NPO NorthPole (northernmost box) and NPO SouthPole (southernmost box). (b) As in (a) but for SLPa and NPO index from the output of the CONTROL run. (c) As in (a) but the ensemble-mean SLPa correlation pattern of the TROP runs.

three times, and a three-point running mean is applied to the power spectra, increasing the degrees of freedom ninefold. Peaks that are referred to as "significant" in the text are those peaks which pass the F-statistic test as described in Section 2.2.3. For filtering of the time series, the Fourier transform method is used. Since this method is problematic at the ends of time series, the first and last year of the time series (i.e.,

12 values on either side) are discarded post-filtering when calculating regressions and correlations with the filtered time series.

Relationships between the NPO and other atmospheric and oceanic variables are deduced through linear regression and correlation analysis. The significance of correlation coefficients is determined through a bootstrap approach, detailed in Section 2.2.1.1.

3.3 Basic Characteristics of the CPW

Before exploring dynamical connections between the NPO and tropical Pacific variability, we provide an overview of some basic characteristics of the CPW phenomenon (Figure 3.2). The monthly time series of the CPW index (Fig. 3.2a) displays variability at several frequencies. Year-to-year variations are evident as is a low-frequency envelope of variability in the index. Two additional specific observations of the CPW index are: (1) Most of the 1990s show a prolonged period of positive values of the CPW index, consistent with the reported prolonged El Niño state observed at that time (e.g., Goddard and Graham 1997; van Loon et al. 2003); and (2) The time series exhibits heteroskedasticity, whereby more low frequency variability is seen over high-frequency variability toward modern times. This change in variance of the time series seemingly coincides with the 1976-77 "climate transition", which has tropical Pacific origins (e.g., Trenberth 1990; Graham et al. 1994; Zhang et al. 1997; Deser et al. 2004; Deser and Phillips 2006).

Figs. 3.2b - 3.2c display spatial characteristics of the CPW phenomenon in SSTa and SLPa via contemporaneous regressions on the index. The contemporaneous regression of DJF SSTa onto the CPW index (Fig. 3.2b) displays warm anomalies in the central Pacific Ocean, flanked on either side by negative anomalies. Negative SSTa also extend in a horseshoe pattern into the extratropical North and South

Pacific. Significant correlations in the SSTa field ($p < 0.05$; red contours in Fig. 3.2b) reside from the central tropical Pacific northeastward to the North American coast, as well as a portion of the negative SSTa in the central North Pacific. The SLPa pattern coinciding with the CPW phenomenon (Fig. 3.2c) displays two key features: a shifted Walker circulation in the tropical Pacific and a distinct SLPa dipole between the North Pacific and North America. The North Pacific features are significant ($p < 0.05$) and reminiscent of NPO variability and its projection onto North American SLP (e.g., Linkin and Nigam 2008), though the negative pole is shifted eastward from the canonical NPO signature (Fig. 3.1a). The response in the North Pacific atmosphere is notably different from that of the canonical ENSO on the AL (e.g, Alexander et al. 2002, 2008).

Ten months prior to a CPW event, the Pacific SSTa field (Fig. 3.2d) has a pattern similar to that in Fig. 3.2b but weaker in magnitude and insignificant almost everywhere. The preceding SLPa pattern to the CPW (Fig. 3.2e) features a similar dipole in SLPa in the North Pacific as in Fig. 3.2c, with positive SLPa in Alaska and Canada and negative SLPa near and north of Hawaii. This precursor SLPa pattern matches well with that identified by Vimont et al. (2001), Vimont et al. (2003), and Anderson (2003). In particular, note that the negative SLPa near Hawaii are significant in both the contemporary and antecedent regression patterns (Figs. 3.2c and 3.2e).

To distinguish CPW variability from that of the canonical ENSO, we contrast the power spectrum (Figure 3.3a) and autocorrelation function (ACF; Figure 3.3b) of the CPW index to that of the NINO3 index, a measure of eastern Pacific warmings. In the power spectra plot, the NINO3 power spectrum displays significant power in the interannual band, as expected (Fig. 3.3a, black line). However, the CPW index exhibits remarkably different behavior (Fig. 3.3a, red curve). The CPW power spectrum shows a small peak near 2 years, illustrating biennial power in this type of

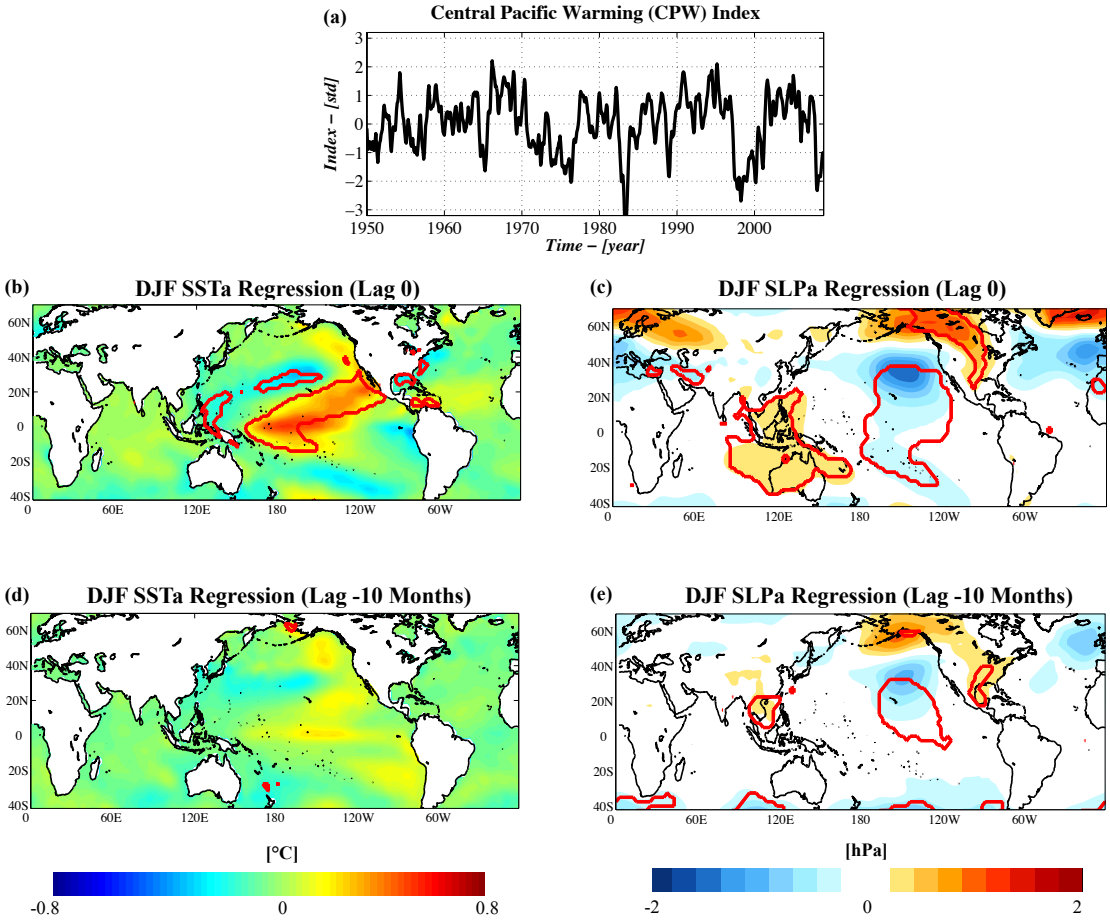

FIG. 3.2. (a) The CPW index (3-month running mean; standardized) from 1950 - 2008. (b) (shading) Regression of DJF SSTa (°C) onto the standardized CPW index. Red contour denotes areas where correlation coefficients exceed the 95% significance level. (c) As in (b) but for DJF SLPa (hPa). (d) As in (b) but for lag = -10 months. (e) As in (c) but for lag = -10 months. Negative lag indicates that the variable leads the CPW index.

El Niño. For periods longer than 2 years, the spectrum increases in power toward low frequencies, with significant power from 6-10 years and even beyond. Thus, the CPW phenomenon has both high-frequency and low-frequency power, in agreement with our hypothesis of its role in seasonal and quasi-decadal variability of the North Pacific. Fig. 3.3b illustrates that the NINO3 ACF has a quicker decay in time than the CPW index; at a lag of one year, the ACF of the NINO3 index is already negative, while for the CPW index, $r \approx 0.25$. For longer lags (3-7 years), the ACF of the NINO3 index is barely positive or near zero, unlike the CPW ACF, which oscillates about $r = -0.2$.

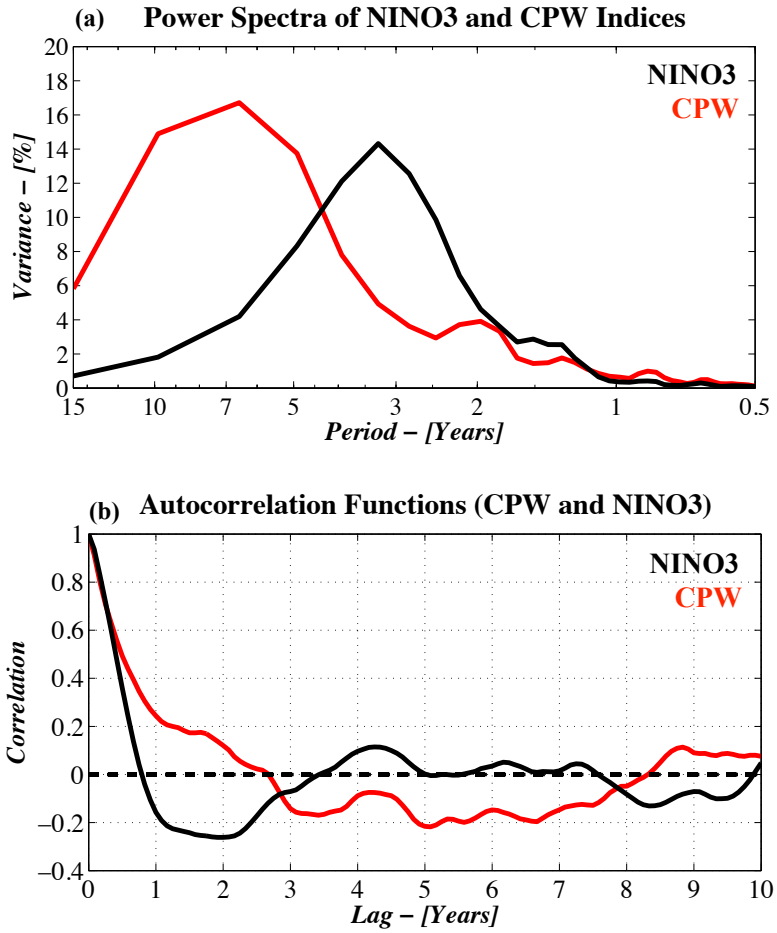

FIG. 3.3. (a) Power spectrum (plotted as percent variance) as a function of period (years) for the NINO3 index (black) and CPW index (red). (b) The ACFs plotted versus lag (years) of the NINO3 index (black) and CPW index (red). Horizontal black dashed line in (b) denotes $r = 0$.

Figure 3.4 shows the correlations of SLPa and SSTa with both the CPW index and the low-passed (periods > 7 years retained) NPO index. In the SLPa correlation plots (Figs. 3.4a and 3.4c), both plots share a common location of strong correlations located over Hawaii and to its east (a portion of which is denoted by the gray box, which serves as the definition for an index used in later analyses). Furthermore, the SSTa correlation plots between the CPW and low-passed NPO index are also highly similar in structure (Figs. 3.4b and 3.4d). These similarities suggest that the effects of the CPW may contribute to low-frequency variability in the subtropical North Pacific atmosphere and, in turn, even the ocean.

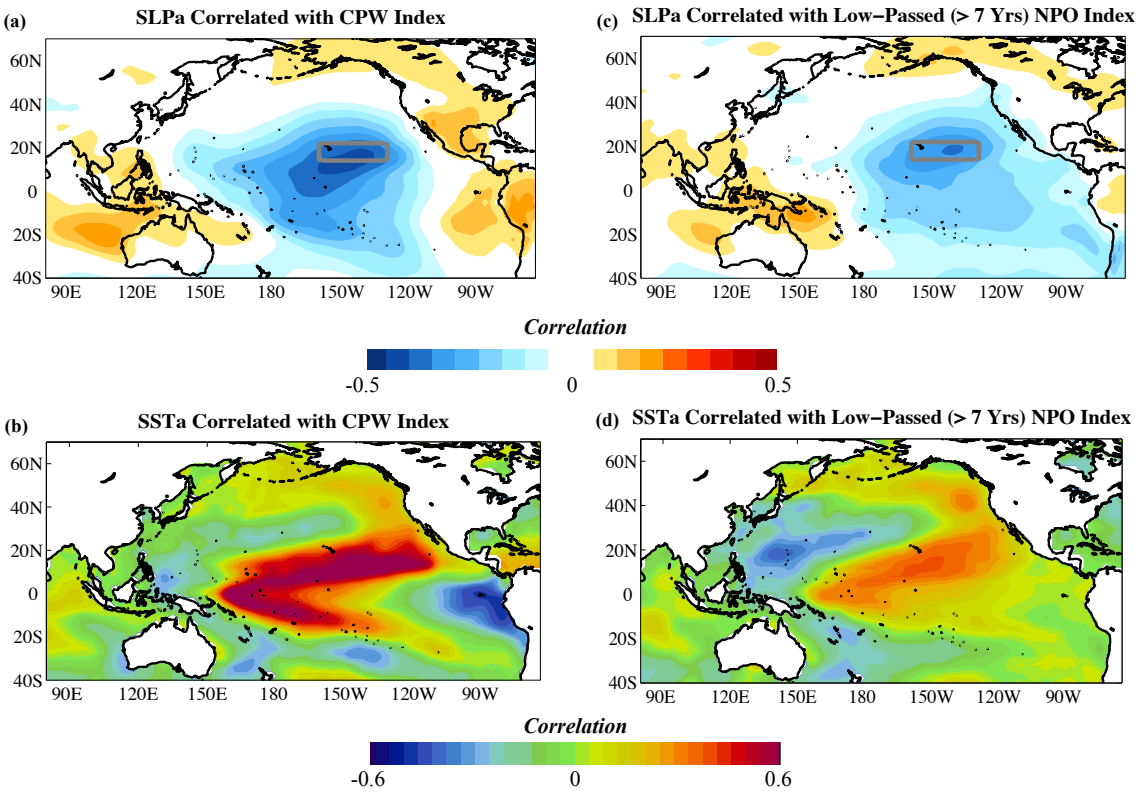

FIG. 3.4. (a) The correlation of observed monthly-mean SLPa with the monthly-mean standardized CPW index. (b) The correlation of observed monthly-mean SSTa with the monthly-mean standardized CPW index. (c) As in (a) but for the observed low-passed (periods > 7 years retained) monthly-mean NPO index. (d) As in (b) but for the observed low-passed monthly-mean NPO index. Gray boxes in (a) and (c) denotes region of SLPa used to define the SLPa Hawaii index (see text).

3.4 Analysis of the NPO and Its Individual Poles

Having examined the statistical connections between the CPW and the NPO, particularly the southern node near Hawaii, our focus shifts to examining more in-depth the NPO phenomenon. While the NPO, by its original definition, denotes an apparent see-saw in pressure between Alaska and Hawaii, this oscillation is not necessarily present at all frequencies. This section and the next offer a detailed analysis of the two poles of the NPO to show that they behave very differently in time and space from one another.

To investigate the variability in each node of the NPO separately, we use the

NPO NP and NPO SP indices defined earlier (Section 3.2.3). We define additionally one more index - an index of the average SLPa over Hawaii (called the SLPa Hawaii index). The index is defined as the average of the SLPa contained within the gray box in Figs. 3.4a and 3.4c. This index is included for a few reasons: (a) its use in previous studies concerning ENSO precursor/CPW activity (e.g., Anderson 2003, 2007); (b) Hawaii lies within the southern node of the NPO (Fig. 3.1a); and (c) for comparison with the ICTP model output, since the NPO southern node in the model runs is displaced slightly from the location in observations (Figs. 3.1b and 3.1c).

Table 3.1 shows the correlations between the four indices (i.e., NPO, NPO NP, NPO SP, and SLPa Hawaii indices) in observations and the two model runs. All correlation values significant at the $p < 0.01$ level are indicated with a double asterisk (**). For the observations, the NPO index is nearly identical to the NPO NP index (correlation close to unity). This high correlation suggests that the NPO index is overwhelmingly dominated by the variability in its northern node. Indeed, the weakest correlations seen in observations are between the NPO NP and the NPO SP ($r = -0.50$) and the SLPa Hawaii ($r = -0.37$) indices. The correlation coefficients for the CONTROL run match very well with the observations, except the relationships between the NPO/NPO SP and NPO NP/NPO SP are weaker. However, the model has almost no relationship between its NPO NP and SLPa Hawaii indices ($r = -0.07$). For the TROP runs, all correlations are nearly identical to those in the CONTROL run, though the NPO/NPO SP correlation increases a bit ($r = -0.44$ for the CONTROL;. $r = -0.50$ for the TROP ensemble-mean). Another noticeable difference between the model runs and observations is the relationship between the NPO and the NPO SP/SLPa Hawaii indices - for these indices, the correlations are dramatically reduced from the observations. Overall, the results in Table 3.1 indicate that (a) the NPO index is strongly tied to the NPO NP variability more than its southern node, even in the AGCM, and (b) the NPO NP and SLPa Hawaii indices

Table 3.1. The cross-correlation between the four indices used to describe NPO variability. Results shown for the observations, the CONTROL run, and the TROP runs (i.e., the ensemble-mean correlation). Correlations with a double asterisk (**) are significant at the 99% level.

Correlated Indices	***Observations***	***CONTROL***	***TROP (ENSMEAN)***
r(NPO, NPO NP)	0.97**	0.97**	0.97**
r(NPO, NPO SP)	-0.70**	-0.44**	-0.50**
r(NPO, SLPa Hawaii)	-0.50**	-0.27**	-0.26**
r(NPO NP, NPO SP)	-0.50**	-0.22**	-0.25**
r(NPO NP, SLPa Hawaii)	-0.37**	-0.07	-0.05
r(NPO SP, SLPa Hawaii)	0.68**	0.83**	0.80**

are the least related among the four indices, particularly in the model where the relationship is close to 0.

Figure 3.5a presents the power spectra of the NPO index (black curve), the NPO NP index (red curve), the NPO SP index (blue curve), and the SLPa Hawaii index (gray curve). For the NPO index, the power spectrum shows minor peaks at periods < 1 year, but then a relatively flat spectrum followed by a slight increase in power in the 3-6 year band. The power spectrum of the NPO NP index (Fig. 3.5a, red curve) follows closely that of the NPO index, with a local maximum in the 2-3 year band and decreasing thereafter. None of the peaks for the NPO or NPO NP power spectrum are significant at the 95% level. The NPO SP power spectrum, however, is quite different than the previous two indices (Fig. 3.5a, blue curve). For periods less than 2 years, the NPO SP power spectrum follows closely that of the NPO and NPO NP. But for periods longer than 2 years, the spectrum increases in power and has a significant peak in the 4-7 year band (dashed blue line in Fig. 3.5a denotes the 95% significance level). The power at this peak is nearly triple that of the power in the NPO and NPO NP indices at those same periods. Finally, the SLPa Hawaii index (Fig. 3.5a, gray line) exhibits a similar power spectrum to that of the NPO SP index, but its maximum power is higher in magnitude and broader in frequency, with significant periods ranging from ∼3-15 years (dashed gray line in Fig.

3.5a denotes the 95% significance level for the SLPa Hawaii power spectrum). Hence, the existence of interannual and decadal-scale power in/near the subtropical node of the NPO indicates that the NPO phenomenon may not be wholly stochastic as previous studies suggested. Moreover, the similarity in the power spectra of the SLPa Hawaii index and the CPW index (Fig. 3.3) further implies a dynamical connection between the two.

To check robustness of these results, power spectrum analysis is repeated for a station record of monthly-mean SLPa from Honolulu, HI, dating from 1921 - 2008 (Quayle, 1989)[5] Fig. 3.5b shows the power spectrum for this station record along with the 95% significance curve (dashed black line). Indeed, the Honolulu station record does exhibit enhanced significant power at low frequencies (7-15 years and beyond).

The power spectra for the NPO indices from the ICTP model runs are shown in Figs. 3.5c (CONTROL) and 3.5d (TROP ENSMEAN). In the CONTROL run (Fig. 3.5c), the spectra follow the observations well in structure, though the magnitude of power for the NPO SP and SLPa Hawaii indices is less at quasi-decadal scales than their observational counterparts. The SLPa Hawaii index still retains significance at the ∼3-15 year band, but the NPO SP power spectrum no longer contains significant peaks. Much of this lack of significance in the NPO SP power spectrum arises from the damping of variance in the power spectrum from the CONTROL run, not in actual structure of the power spectrum (i.e., it still peaks in the interannual time frame). These results are consistent with the damping of low-frequency atmospheric signals in AGCMs forced with prescribed time-varying mid-latitude SSTs (Bladé, 1997; Barsugli and Battisti, 1998).

The ensemble-mean power spectra from the ICTP TROP runs recover much of the characteristics of the observed spectra, including at low frequencies (Fig. 3.5d).

[5]The data were downloaded from the Data Support Section (DSS) of the Computational and Information Systems Laboratory (CISL) at NCAR - `http://dss.ucar.edu/datasets/ds570.0/`.

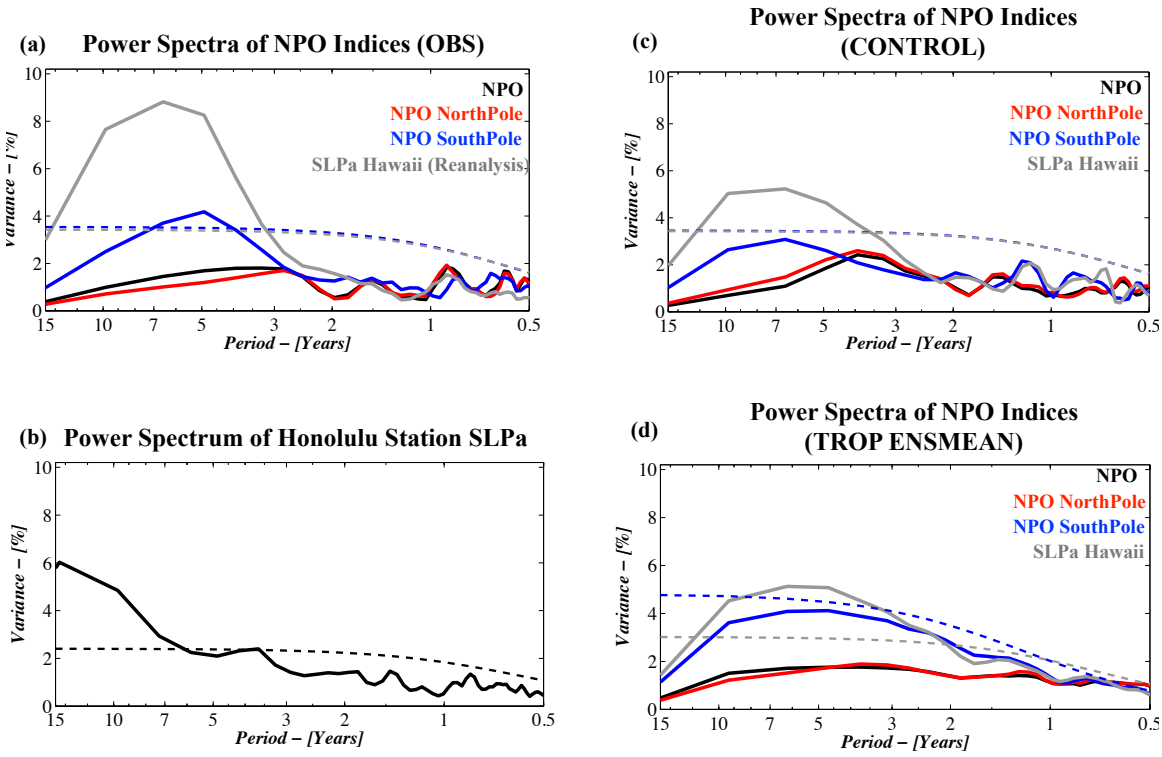

FIG. 3.5. (a) Power spectra (plotted as percent variance) of the NPO index (solid black), the NPO NP index (solid red), the NPO SP index (solid blue), and the SLPa Hawaii index (solid gray). Dashed blue (gray) line denotes the 95% significance curve for the NPO SP (SLPa Hawaii) power spectrum (b) Power spectrum (solid black) of a station record of Honolulu SLP from 1921 - 2008. Dashed black line denotes 95% significance curve. (c) As in (a) but for the ICTP CONTROL run. (d) As in (a) but for the ensemble-mean spectra of the indices from the ICTP TROP runs. The power spectra of the NPO and NPO NP indices do not pass any significance test and thus their significance curves are not plotted.

The power spectra of the NPO and NPO NP indices remain relatively flat for all periods, including high frequencies. However, the SLPa Hawaii and NPO SP power spectra in the ensemble-mean display interannual to decadal scale variability, with peaks actually broadening for both indices compared to the observed and the CONTROL (Figs. 3.5a and 3.5c). Most of the low-frequency signature of the SLPa Hawaii index is significant, though that of the NPO SP just barely misses significance for the ensemble-mean. Nevertheless, the ensemble-mean results indicate that the tropical Pacific SSTa forcing alone contributes significant power to the low-frequency content of the subtropical North Pacific SLP indices, further supporting our hypothesis of the

tropically-forced low-frequency variability of the NPO SP.

3.5 High-Frequency and Low-Frequency NPO Variability

3.5.1 Observations

As seen in Fig. 3.5, NPO variability consists of both high frequency and low frequency, particularly depending on which pole is studied. Based on evidence presented earlier, we hypothesize that the different frequency bands of the poles of the NPO contribute to two different processes in the tropical Pacific and North Pacific. At high frequencies, NPO variability generates warm SSTa in the central tropical Pacific Ocean, which may initiate a canonical ENSO or a CPW event (Vimont et al., 2001, 2003; Anderson, 2003). For decadal-scale variability, the NPO SP and SLPa Hawaii indices should project most strongly onto the central tropical Pacific SSTa because these indices contain the low-frequency content similar to that in the CPW.

In the following analyses, each of the four NPO indices are decomposed into two frequency bands: a high-passed version, which retains signals with periods less than 2 years, and a low-passed version, which retains signals with periods greater than 7 years. The 2-year cutoff for the high-pass filter allows us to examine seasonal signals and resolve the SFM along with high-frequency variability of the CPW phenomenon. The 7-year cutoff for the low-pass filter was chosen to coincide with low-frequency CPW variability.

Figure 3.6 displays the lag correlation of DJF SSTa with the high-pass filtered versions of the NPO index (top row), NPO NP index (second row), inverted NPO SP index (third row), and inverted SLPa Hawaii index (fourth row) for three specific lags: lag 0 (Fig. 3.6, Column 1), lag +6 months (Fig. 3.6, Column 2), and lag +12 months (Fig. 3.6, Column 3) (positive lags indicate that the index leads the SSTa). The last two indices are inverted so that positive SSTa are related to the positive

phase of the NPO. The lag 0 pattern depicts the characteristic ENSO precursor pattern in SSTs (e.g., Penland and Sardeshmukh 1995). The lag 0 correlation maps for the NPO and NPO SP high-pass filtered indices are very similar in structure and magnitude (Figs. 3.6a and 3.6c), indicating that the NPO SP index alone is capable of capturing the ENSO precursor pattern. By contrast, the SSTa correlation map with the high-pass filtered NPO NP index (Fig. 3.6b) has its highest correlation values in the far North Pacific and a weaker signal in the subtropical North Pacific. This difference further supports that the NPO NP has a stronger influence locally in the North Pacific because of its strong relation to high-latitude atmospheric forcing. The correlation maps of SSTa correlation with the high-passed SLPa Hawaii index (Fig. 3.6d) is similar to that of the NPO index (Fig. 3.6a).

Looking at future lags, the propagation of the subtropical SSTa into the tropical Pacific Ocean 12 months later is clearly evident for the high-passed NPO SP and SLPa Hawaii correlation plots (i.e., Figs. 3.6g and 3.6k for the NPO SP index and 3.6h and 3.6l for SLPa Hawaii index). This propagation is the key signature of the SFM, and thus these two indices most clearly capture it. Note that the NPO and NPO NP indices too show a propagation of SSTa, but the correlations are weaker than for the other two indices. Furthermore, the evolution of the subtropical SSTa pattern is quite different, particularly at lag +6 months, where the high-passed NPO and NPO NP correlation plots actually suggest nearly zero or very weakly positive correlations in SSTa near Hawaii (Figs. 3.6e and 3.6f).

While the SSTa correlation maps with the high-pass filtered versions of the four NPO indices capture the ENSO precursor pattern, correlation maps with the low-pass filtered versions of the same indices are tied more strongly to the CPW phenomenon (Figure 3.7). Using the low-pass filtered the NPO SP and SLPa Hawaii indices (Figs. 3.7c and 3.7d) produce very similar SSTa correlation maps to that of the CPW (Fig. 3.4c) with strong positive correlations extending from the far western

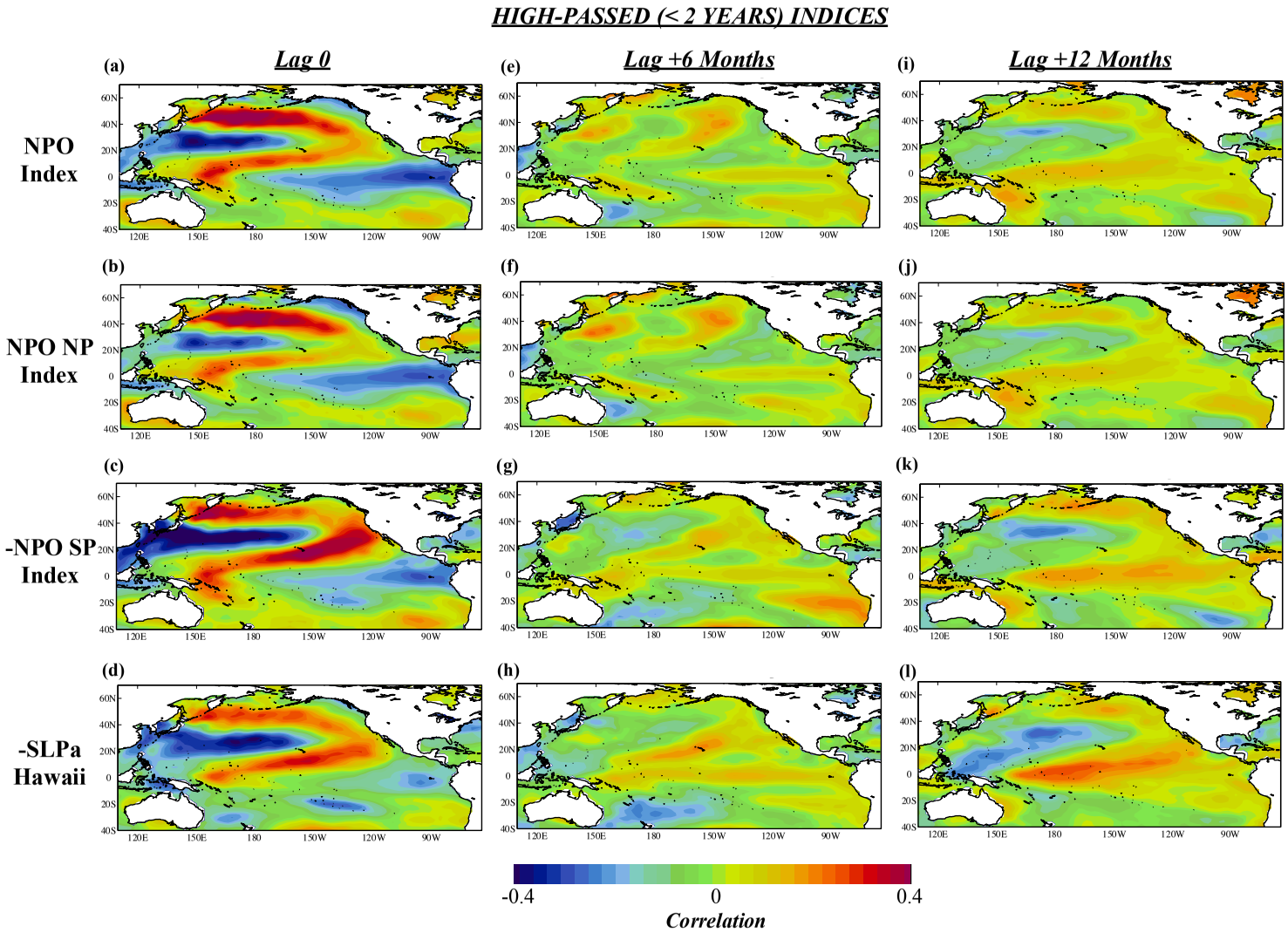

FIG. 3.6. Correlation of observed DJF SSTa with the high-pass (less than 2 years) filtered NPO indices for observations: (a) NPO index; (b) NPO NP index; (c) NPO SP index (inverted); (d) SLPa Hawaii index (inverted). (e) - (h) As in (a) - (d) except for lag = +6 months. (i) - (l) As in (a) - (d) except for lag = +12 months. Positive lag indicates that the index leads the SSTa.

tropical Pacific Ocean northeastward just south of Hawaii and up the North American coast. Negative correlations extend from the Maritime Continent and western subtropical North Pacific into the central North Pacific. For the correlation map associated with the low-passed NPO index (Fig. 3.7a), the signal across the far northern and northwestern Pacific Ocean is stronger than in the NPO SP or SLPa Hawaii correlation maps, while the positive correlations in the subtropical and tropical Pacific Ocean are comparable in structure but lower in magnitude. The SSTa correlation map with the low-passed NPO NP index, however, has a slightly different pattern (Fig. 3.7b). Maximum positive correlations exist in the far North Pacific, in the same region as seen with the high-passed NPO NP correlation map (Fig. 3.6b) and also where the correlations with the low-passed NPO index are a maximum. This result is expected - recall from Table 3.1 that the NPO and NPO NP index are virtually identical, as are their power spectra (Fig. 3.5a).

More evidence of the dominance of the NPO SP and SLPa Hawaii in low-frequency connections with the tropical Pacific SSTa and the CPW phenomenon is shown in Figure 3.8. When correlating the low-passed versions of the CPW index with the low-passed NPO or NPO NP indices, the correlations are insignificant ($r = 0.56$ and $r = 0.31$, respectively). However, for the NPO SP and SLPa Hawaii indices, the correlations are high and significant ($r = 0.77$ for both; $p < 0.05$; Figs. 3.8c and 3.8d). In particular, for almost most of the 1990s, a time of moderate CPW activity (Fig. 3.2a), the low-passed NPO SP and SLPa Hawaii indices almost perfectly coincide with the low-passed CPW index.

3.5.2 Low Frequency Connections in the ICTP Model

The observational results presented in Section 3.5.1 supports our hypothesis of the dual-role of the NPO at different frequencies: its role in the SFM at high frequencies and its connection with tropical Pacific SSTa variability, particularly in the

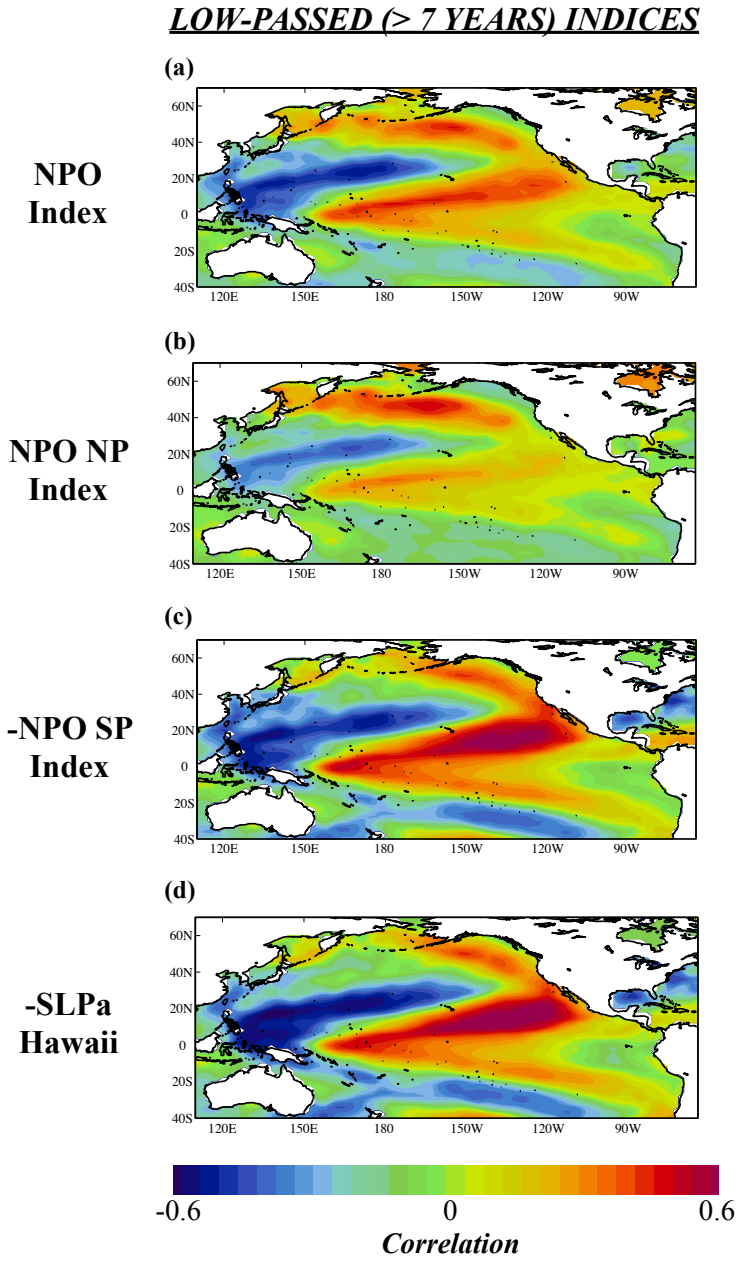

FIG. 3.7. Correlation of observed DJF SSTa with the low-pass (greater than 7 years) filtered NPO indices for observations: (a) NPO index; (b) NPO NP index; (c) NPO SP index (inverted); (d) SLPa Hawaii index (inverted).

region of the CPW phenomenon, at low frequencies. We now use the ICTP TROP runs to test our hypothesis that tropical Pacific SSTa variability forces and drives the low-frequency NPO SP/SLPa Hawaii signature. Figure 3.9 shows the CONTROL and ensemble-mean correlation maps between the tropical Pacific SSTa in the model

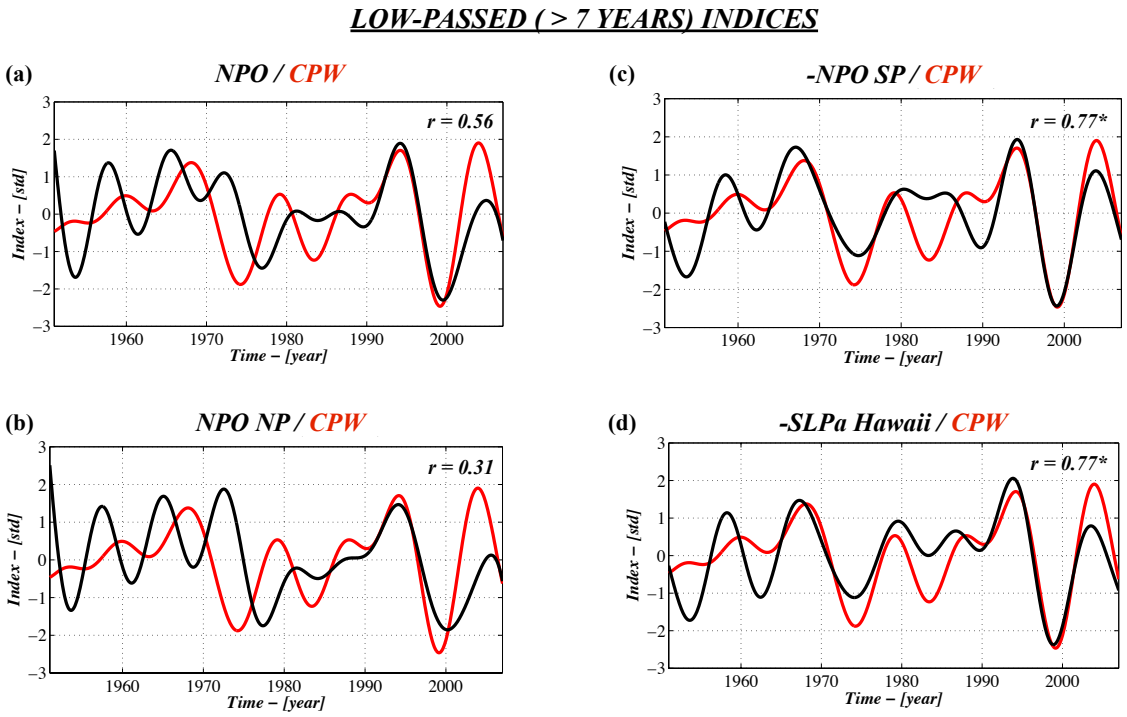

FIG. 3.8. (a) The observed low-passed NPO index (black) and low-passed CPW index (red) from 1951-2007. (b) As in (a) but with the low-passed NPO NP index (black). (c) As in (a) but with the low-passed NPO SP index (inverted; black). (d) As in (a) but with the low-passed SLPa Hawaii index (inverted; black). Correlations between the two indices indicated in each panel. Single asterisk (*) denotes that the correlation is significant at the $p < 0.05$ level.

and the low-passed versions of the four NPO indices. Here, the CONTROL run is included as a baseline for comparison. Immediately noticeable is the great difference between using the low-passed NPO/NPO NP and NPO SP/SLPa Hawaii indices in the correlations. The CONTROL and TROP ENSMEAN NPO/NPO NP correlation plots (Figs. 3.9a - b and 3.9e - f) show that these indices have almost no correlation or even weak *negative* correlations with SSTa in the tropics, contrary to what we see in the observations (Fig. 3.7). However, when looking at the bottom two rows of Fig. 3.9, the CONTROL run of the model correctly simulates the positive correlations with the low-passed inverted NPO SP and SLPa Hawaii (Figs. 3.9c and 3.9d). The tropical Pacific-forced-only runs of the model also recover these positive correlations in the central tropical Pacific, particularly for the SLPa Hawaii correlation map (Fig.

3.9h). Indeed, these results indicate that tropical Pacific SSTa directly drive low-frequency power in the subtropical node of the NPO.

3.6 A Proposed Mechanism for CPW/Extratropical North Pacific Connections

The previous sections highlighted that NPO variability differs depending on the pole examined or whether dealing with high-frequency or low-frequency variability. Results indicated that the subtropical node of the NPO/SLPa near Hawaii captured both the high- and low-frequency signatures of the NPO in the SSTa field.

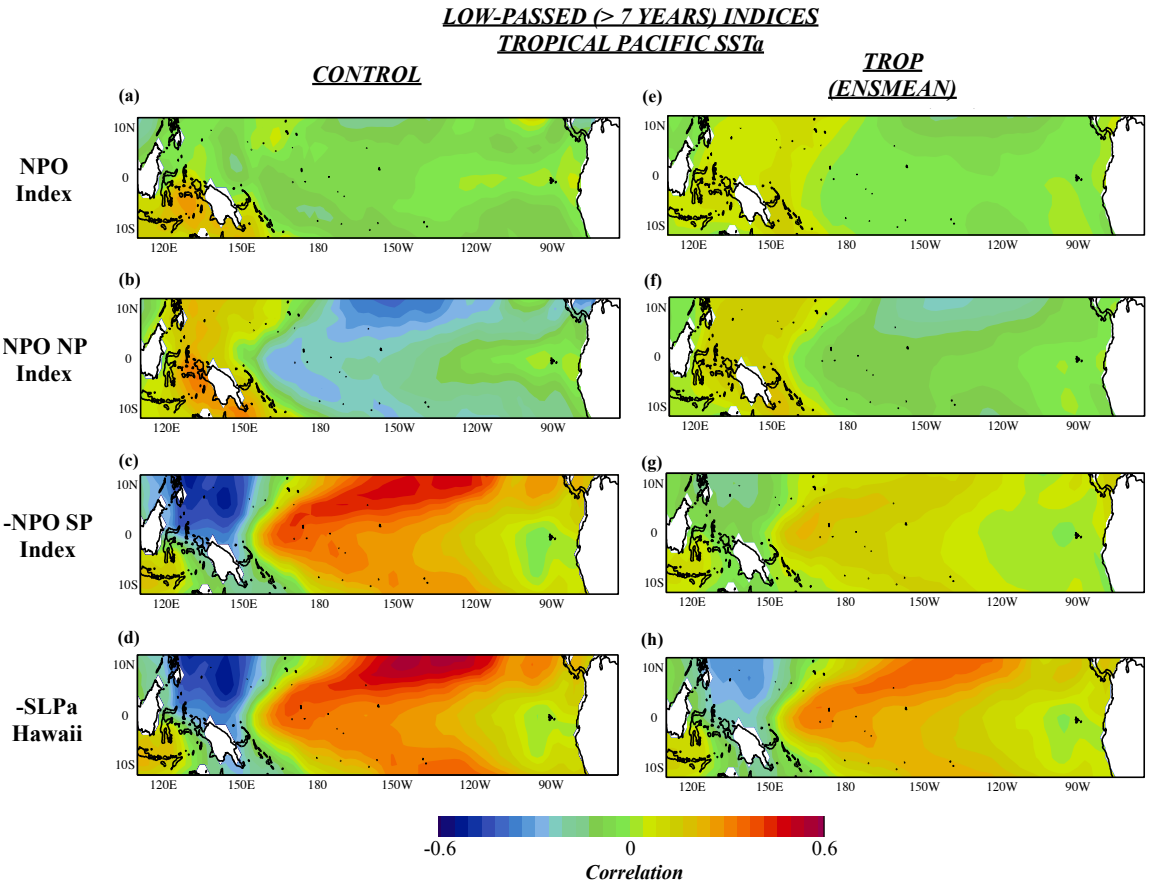

FIG. 3.9. (a) Correlation of DJF SSTa with the low-pass (greater than 7 years) filtered NPO indices from the CONTROL run: (a) NPO index; (b) NPO NP index; (c) NPO SP index (inverted); (d) SLPa Hawaii index (inverted). (e) - (h) As in (a) - (d) but for the ensemble-mean correlation patterns from the TROP runs.

Moreover, as shown with the model results, tropical Pacific SSTa are a key driver for the subtropical North Pacific SLPa near Hawaii at low frequencies.

As a step toward understanding the dynamical links between the subtropical North Pacific atmosphere and the CPW, a potential mechanism involving a Rossby wavetrain related to the CPW is presented in Figure 3.10. The 200 hPa streamfunction anomaly (Ψ') regression pattern associated with the CPW index (Fig. 3.10a; shading) clearly shows a Rossby wavetrain originating in the central tropical Pacific and oriented north/south, with maximum amplitude centers in the Northern Hemisphere just to the south/southeast and north/northwest of the Hawaiian Islands. The wavetrain associated with the CPW does not project strongly into Alaska and eastern Russia. However, the wavetrain does project directly onto the signature of the SLPa Hawaii index in the upper troposphere (Fig. 3.10a; line contours), with the positive and negative contours/shaded contours coinciding. To contrast this wavetrain with that associated with the canonical ENSO phenomenon, Fig. 3.10b shows the regression of 200 hPa Ψ' with the NINO3 index (shading) and the SLPa Hawaii index (contours). The wavetrain excited by a canonical ENSO episode is displaced slightly east of that by the CPW and is oriented more northeastward, projecting much less on the upper tropospheric Hawaiian SLPa signature (Fig. 3.10b, line contours) and more on the mean position of the AL (i.e., the region of strong negative Ψ' south of Alaska; Fig. 3.10b). In fact, across the far northern Pacific and into Alaska, note that negative streamfunction anomalies associated with NINO3 project onto *positive* streamfunction anomalies associated with the SLPa Hawaii index, indicating a cancellation in the net. Thus, there is a noticeable difference in the projection of the CPW phenomenon vs. the canonical ENSO signature in the North Pacific, the former which has a direct impact on the region near the NPO SP/Hawaii.

Differences also exist in North America and the North American east coast. For the CPW regression pattern, negative streamfunction anomalies maximize in the

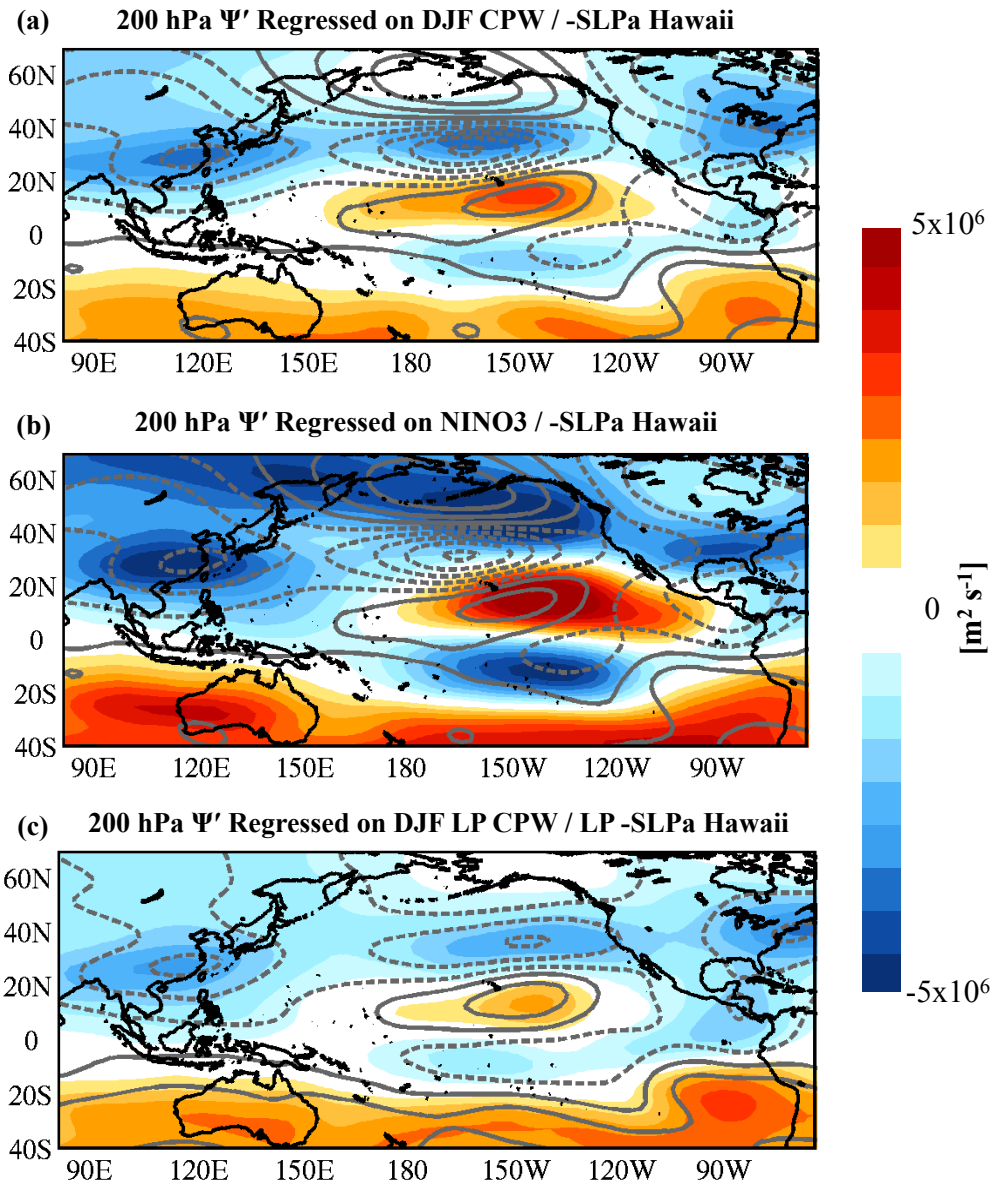

FIG. 3.10. (a) (shading) Regression of Ψ' (m^2s^{-1}) onto DJF values of the standardized CPW index. (Contours) Regression of Ψ' (m^2s^{-1}) anomalies onto DJF values of the standardized inverted SLPa Hawaii index. (b) As in (a) but shading represents regression of Ψ' (m^2s^{-1}) onto DJF values of the standardized NINO3 index. (c) (shading) Regression of Ψ' (m^2s^{-1}) onto DJF values of the standardized low-passed (i.e., periods greater than 7 years retained) CPW index. (Contours) Regression of Ψ' (m^2s^{-1}) onto DJF values of the low-passed standardized inverted SLPa Hawaii index. In all plots, gray contours have contour interval $1x10^6$ m^2s^{-1} ($\ldots,-2.5x10^6$, $-1.5x10^6$, $-0.5x10^6$, $0.5x10^6$, $1.5x10^6,\ldots$). Positive (negative) regression coefficients are solid (dashed) and indicate anomalous anticyclonic (cyclonic) circulation for the Northern Hemisphere. For the Southern Hemisphere, positive (negative) anomalies indicate anomalous cyclonic (anticyclonic) circulation.

northeastern United States (Fig. 3.10a). However, for the canonical ENSO, the negative streamfunction anomalies have a maximum magnitude across the southeastern United States (Fig. 3.10b) with weaker anomalies in Canada and the northern United States. These differences emphasize that canonical and central Pacific El Niño events have different effects on the storm tracks along the eastern United States and thus which type of El Niño develops can affect seasonal forecasts for Pacific and Atlantic wintertime weather.

Finally, when looking at low-frequency CPW variability and its connection with the low-frequency upper tropospheric circulation, Fig. 3.10c illustrates that the contours and shading nearly coincide exactly, supporting the idea that NPO variability is influenced by seasonal and low-frequency changes in the CPW phenomenon. Additionally, the low-frequency streamfunction regression map still exhibits negative anomalies in the northeastern United States and off the New England coast, suggesting that the quasi-decadal changes in the CPW could play a role in changes in storm variability and climate in that area. More work is needed to elucidate these low frequency relationships between the extratropical atmosphere and CPW activity.

3.7 Chapter Summary and Discussion

The analyses presented in this chapter contribute to addressing two initial hypotheses involving the NPO: (1) While the NPO itself is stochastic, its individual nodes exhibit different behavior in space and especially in frequency content; and (2) NPO SP variability at low frequencies is related to and forced by tropical Pacific SSTa variability. Through observational analyses and modeling experiments, we have affirmed these hypotheses and thus highlighted important dynamics associated with the NPO that are tied to other large-scale modes of Pacific interannual and decadal climate variability.

The dissection of the NPO into its two poles reveals that the phenomenon is dominated by two different processes for each pole. By nature of being an oscillation, the NPO NP and NPO SP are correlated, especially for high-frequency variability. Indeed, the power spectra for all NPO indices are nearly identical for periodicities less than 2 years (Fig. 3.5a). But, the NPO NP power spectrum has no significant power at longer periods, suggesting that seasonal variability dominates this mode. The NPO SP power spectrum, by contrast, illustrates significantly longer-term periodicity (5-10 years), which is matched well by a Hawaiian station record (Fig. 3.5b). The difference in the characteristics of each node illustrates the definition of the NPO via an EOF analysis masks the importance of the NPO SP in its role in long-term North Pacific and tropical Pacific climate variability. In particular, Figs. 3.6 and 3.7 illustrate that the NPO SP and SLPa Hawaii indices sufficiently capture a SSTa propagation pattern that is consistent with CPW activity and also possibly with the SFM at high frequencies and the connections between the NPO and the CPW at low frequencies. Moreover, the NPO and NPO NP indices are unable to explain low frequency changes in the central tropical Pacific/CPW, but the subtropical NPO indices do (Fig. 3.8).

Our original hypothesis that low frequency NPO variability is largely driven by tropical Pacific SSTa was supported with the TROP runs. The low-frequency connections between particularly the NPO SP/SLPa Hawaii indices and the CPW-type variability in the tropical SSTa field (Figs. 3.9g - 3.9h) demonstrates that variability in the tropical Pacific contributes to the deterministic component of the subtropical node of the NPO. This link between tropical Pacific SSTa variability/CPW variability and the SLPa Hawaii index also holds for the unfiltered time series (Di Lorenzo et al., 2010), suggesting a multi-timescale link between the two. Moreover, as the NPO/NPO SP is the primary forcing for the NPGO, the low-frequency component of the SLPa Hawaii index from the ensemble-mean of the TROP runs indeed reconstructs a substantial fraction of the low-frequency characteristics of the NPGO (Di Lorenzo

et al., 2010). Thus, there is a link between decadal-scale oceanic variability in the North Pacific (i.e., the NPGO) and that in the tropical Pacific (i.e., CPW). The two climate variability patterns also share a common correlation pattern, lending more support to the dynamical connection between the two climate variability patterns.

With the links between the deterministic component of the NPO SP from tropical Pacific SSTa variability, the links between SSTa variability in the CPW region and SLPa Hawaii as well as the NPGO, we have the necessary pieces to build a similar framework of tropical Pacific - North Pacific interannual and decadal-scale variability to that of the ENSO-AL-PDO framework. More about this new framework is reserved for the conclusions (Chapter 6). However, what is lacking in an "atmospheric bridge" and/or "oceanic tunnel"-type mechanism which links these three secondary modes of variability (i.e., the CPW, NPO, and NPGO) together dynamically. Section 3.6 offers initial evidence that a unique atmospheric bridge is at work in the Pacific for the CPW phenomenon, with implications for changes in atmospheric circulation in North America and the Atlantic that are different than that associated with eastern Pacific warmings (Fig. 3.10). Parallel analyses like those reviewed and conducted in Alexander et al. (2002) are needed to further develop this hypothesized mechanism for the CPW and expand on its role in extratropical wintertime variability in the Northern Hemisphere.

CHAPTER IV

NORTH PACIFIC DECADAL VARIABILITY AND ITS REPRESENTATION IN COUPLED CLIMATE MODELS

The work presented in this chapter is now accepted for publication in Journal of Climate (Furtado et al., 2010).

Chapter 3 presented evidence of a new framework of NPDV that includes secondary modes of variability in the tropical Pacific - North Pacific climate system - the CPW, the NPO, and the NPGO. This framework is now employed to investigate how the leading coupled climate models capture the leading two modes of SLPa and SSTa in the North Pacific and tropical Pacific Ocean. As shown, the models have significant issues capturing the second leading modes of North Pacific ocean-atmosphere variability and their dynamical connection. More importantly, the links between the tropical and extratropical modes of variability is very questionable and even inaccurate in these models. Such results present caution on interpreting predicted changes in the global climate system related to NPDV derived from the IPCC models.

4.1 Background and Motivation

NPDV is a key component in predictability studies of both regional and global climate change. Namias (1969) identified "climatic regimes" linked to changes in North Pacific SST induced by shifts in atmospheric SLP patterns in both the winter and summer. Subsequent studies by Namias (1972) and Davis (1976) explored the predictability aspect of these large-scale patterns of variability in the North Pacific in both the atmosphere and the ocean, the latter of which retains more memory

and can thus sustain multi-decadal variability. Though studies of NPDV remained dormant through the 1980s, the emergence of the ENSO phenomenon in the climate literature in the 1990s reinvigorated interest in the subject (e.g., Trenberth 1990; Graham et al. 1994; Trenberth and Hurrell 1994; Zhang et al. 1997). The discovery of links between NPDV and changes in marine ecosystems (Mantua et al. 1997; Mantua and Hare 2000), along with its connections to tropical Pacific climate variability (e.g., Alexander et al. 2002; Anderson 2003; Newman et al. 2003; Deser et al. 2004; Newman 2007; Alexander et al. 2008; Di Lorenzo et al. 2008), emphasizes the need to better understand and characterize NPDV for global climate change predictions.

Given the links between the PDO and the NPGO and global climate, as described in Chapter 1, the predictability and characterization of these two modes in coupled climate models is an important open question in climate dynamics. Thus far, studies concerning long-term predictability of Pacific climate have focused on changes in the amplitude and frequency of ENSO and subsequent effects on teleconnection patterns (e.g., Meehl et al. 2006; Merryfield 2006; Yeh and Kirtman 2007). Overland and Wang (2007), by contrast, examined changes in the PDO under future warming scenarios in ten coupled models used in the IPCC AR4. This study found that the ensemble-mean of the ten models predicted uniform warming of the entire North Pacific basin with no change in the mean spatial pattern of the PDO. Newman (2007) explored interannual to decadal predictability of tropical and North Pacific SSTs in the IPCC models and concluded that North Pacific/tropical Pacific connections in the IPCC models were poorly represented, thus affecting predictability of decadal-scale variability with the models. Considering these previous studies, there still remains questions on potential changes in the frequency of the leading modes of North Pacific variability and the degree to which these modes of variability are tied to atmospheric forcing patterns, both directly and remotely.

The focus of this chapter is to address some of these outstanding issues through

analysis of output from the 24 coupled climate models used in the IPCC AR4. The goals are: (1) to quantify the statistics of the leading patterns of NPDV climate variability, both in hindcast (20^{th} century) simulations and future (21^{st} century) projections; (2) to evaluate the relationship between atmospheric forcing and the oceanic modes of NPDV; and (3) to assess the degree to which known atmospheric-oceanic teleconnections between the tropical Pacific and the North Pacific are represented in the models. Data and techniques used are first presented in Section 4.2. Section 4.3 parallels Overland and Wang (2007) in looking at the leading EOFs of North Pacific SSTa as well as the power spectra associated with these leading patterns. Then, Section 4.4 explores the use of a simple AR-1 model to evaluate atmosphere-ocean connections in the North Pacific. Section 4.5 explores how the models capture teleconnections between the tropical Pacific and the North Pacific associated with both the canonical ENSO and CPWs. A synthesis of the results concludes the chapter.

4.2 Data and Methods

4.2.1 Specifics on IPCC Model Output

A description of the IPCC models was presented in Section 2.1.2.2 with a list of the models in Table 2.1. Multiple realizations of the monthly-mean SLP and SST output are extracted for each model. All available realizations are used in processing the statistics for a particular model; i.e. the mean value of statistics from all realizations of a particular model are used as the climate signature for that model. The incorporation of all realizations allows us to avoid run-to-run discrepancies in the models, as averaging will "smooth" the statistics. However, every model does not have the same number of realizations, so one disadvantage of this method is that models with only one realization available (e.g, the BCCR-BCM2 model) may be affected more by noise than models with multiple realizations (e.g., the GISS-ER model). For

eight of the 24 models, only one realization for each scenario was available.

The spatial resolution for SLP and SST in the models varies between models and within the same model for atmospheric and oceanic variables. To facilitate comparisons with the observations, the SLP and SST fields are interpolated onto the same grids as their observational counterparts (i.e., 2.5° x 2.5° for SLP, and 2° x 2° for SST). For analyses in the North Pacific, the spatial domain is defined as 15°N - 70°N in latitude and from 80°E to 65°W in longitude. For EOF analyses of the tropical Pacific only, the spatial domain is changed in latitude to 20°S - 20°N. When exploring North Pacific and tropical Pacific connections together, we use the latitudinal domain 40°S - 70°N. These same domains and variables are used for observational analyses.

Temporally, output from model years 1900 - 1999 represents 20^{th} century climate, while model years 2001 - 2100 are used for the 21^{st} century. Though the model output span a longer period of time than the observations (which only go from 1950 - 2008), our analyses and conclusions are not greatly affected by this difference in time.

4.2.2 Analysis Techniques

The primary statistical techniques used to isolate patterns of climate variability in the Pacific are traditional EOF and cEOF analysis of the SLPa and SSTa fields. For EOF analysis, each field is weighted by the square root of the cosine of latitude before computing the eigenvalues and eigenfunctions of $\mathbf{A}$ (see (2.9)). For cEOF analysis, SLPa and SSTa are used to construct $\mathbf{A}$. Because the two fields have different variances and magnitudes, each field is normalized separately before applying SVD. The SLPa field is first normalized by the standard deviation at each latitude to account for the greater variance in SLP in the extratropics. Then, both fields are standardized by the mean standard deviation in the respective field before SVD analysis is performed. Only the two leading patterns of climate covariability are retained, as these two patterns pass the significance test of North et al. (1982) and

are also of most interest for our study on NPDV.

For both EOF and cEOF analyses, the anomaly fields are calculated by removing the climatological monthly mean from the raw fields. The anomalies are then linearly detrended, and a 3-month temporal filter is applied before eigenanalysis. Furthermore, we retain only the DJF values of the filtered fields. The choice of using winter values only versus the entire year was made because the North Pacific atmosphere-ocean connections are dominant in the boreal winter months. EC time series are obtained by projecting individual unfiltered monthly-mean anomaly maps onto the corresponding EOF/cEOF spatial pattern for each mode. These time series are then used for temporal analyses. Table 4.1 provides a list of the nomenclature used to refer to the various EOFs, cEOFs, and EC time series presented in this chapter.

To explore the temporal variability of the leading SLPa and SSTa patterns, spectral analysis is used. All power spectra are normalized so that the area under the individual spectrum is unity. Hence, the values represented in the power spectra are the percentage of total variance explained at that frequency. Periods with significant power are determined using the method outlined in Section 2.2.3.

4.2.3 Ensemble-Mean Statistics

The coupled climate model output consists of multiple realizations of the same model. Characteristic climate statistics from a particular model are computed as the ensemble-mean statistics; i.e., the mean of the individual statistic among all realizations. For example, the ensemble-mean leading pattern of variability of North Pacific SSTa is calculated as follows: (1) the leading EOF is computed for a particular model, and then the SSTa from the model are regressed onto the standardized first PC time series; (2) the sign of the anomalies are changed such that the sign of one of the poles in the pattern matches among the realizations, using the observed pattern as a guide for the sign of the pole; and (c) the individual regression maps are averaged together.

Table 4.1. Abbreviations for various EOF and cEOF patterns and EC time series used in this chapter.

Abbreviation	*Description*
EOF-1_{SST}/EOF-1_{SLP}	The spatial representation of the leading mode of variability of North Pacific boreal winter SSTa/SLPa.
EOF-2_{SST}/EOF-2_{SLP}	The spatial representation of the second leading mode of variability of North Pacific boreal winter SSTa/SLPa.
cEOF-1_{SST}/cEOF-1_{SLP}	The spatial representation in SSTa/SLPa space of the leading mode of covariability between North Pacific boreal winter SSTa and SLPa.
cEOF-2_{SST}/cEOF-2_{SLP}	The spatial representation in SSTa/SLPa space of the second leading mode of covariability between North Pacific boreal winter SSTa and SLPa.
EOF-$1_{Tropics-SST}$/EOF-$2_{Tropics-SST}$	The leading/second leading mode of variability of tropical Pacific boreal winter SSTa.
EC-1_{SST}/EC-1_{SLP}	The monthly expansion coefficient time series associated with EOF-1_{SST}/EOF-1_{SLP}.
EC-2_{SST}/EC-2_{SLP}	The monthly expansion coefficient time series associated with EOF-2_{SST}/EOF-2_{SLP}.
cEC-1_{SST}/cEC-1_{SLP}	The monthly expansion coefficient time series associated with cEOF-1_{SST}/cEOF-1_{SLP}.
cEC-2_{SST}/cEC-2_{SLP}	The monthly expansion coefficient time series associated with cEOF-2_{SST}/cEOF-2_{SLP}.
EC-$1_{Tropics-SST}$/EC-$2_{Tropics-SST}$	The monthly expansion coefficient time series associated with EOF-$1_{Tropics-SST}$/EOF-$2_{Tropics-SST}$.

Similarly, for power spectra, the individual normalized power spectra of the models are averaged together to get the power spectrum of the ensemble-mean of the models.

4.3 Leading Modes of North Pacific SSTa in Present and Future Climate

The study begins by extending the statistical analysis of Overland and Wang (2007), who explored changes of the first leading mode of North Pacific SSTa (i.e., the PDO) in the IPCC models, to also include the second leading mode. Figure 4.1 compares the two leading modes (EOF-1_{SST} and EOF-2_{SST}) from observations (Figs. 4.1a and 4.1b) to the mean EOF patterns from the models (Figs. 4.1c and 4.1d). In

the observations, the canonical PDO pattern emerges in EOF-1_{SST} (Fig. 4.1a), with negative central North Pacific SSTa encircled by positive SSTa to the east. The temporal evolution of the first mode (EC-1_{SST}) closely tracks the monthly PDO index (downloaded from `http://jisao.washington.edu/pdo/PDO.latest`); the correlation between the two time series is $r = 0.71$ ($p < 0.01$). The second leading pattern of SSTa (Fig. 4.1b) exhibits a northeast-southwest oriented tripole, which is very similar to the SSTa regression pattern associated with the NPGO index and that of the Victoria mode (Bond et al., 2003). The correlation between the temporal evolution of the second mode (EC-2_{SST}) and the monthly NPGO index (downloaded from `http://ocean.eas.gatech.edu/npgo`) is $r = 0.28$ ($p < 0.05$). The ensemble-mean EOF-1_{SST} (Fig. 4.1c) compares visually well with the observations, while there are two main differences for EOF-2_{SST} (Fig. 4.1d): the lack of the tripole structure and the placement of the positive anomaly closer to the North American coast compared to observations (Figs. 4.1b and 4.1d).

Spatial correlations between individual model patterns of EOF-1_{SST} and EOF-2_{SST} and the observational counterparts are shown in Figure 4.2. All shaded correlations exceed the 95% significance level. For EOF-1_{SST} and EOF-2_{SST} the spatial correlations for the ensemble-mean patterns are $r = 0.76$ and $r = 0.81$, respectively. Note that spatial correlations vary considerably among individual models, with some (e.g., the MIUB-ECHO-G and NCAR-CCSM3.0 models) having lower spatial correlations for both North Pacific SST EOFs than the ensemble-mean, while others (e.g., both MIROC models) have higher correlations than the ensemble-mean.

The spatial patterns of EOF-1_{SST} and EOF-2_{SST} remain virtually unchanged for the future with significant spatial correlations between the ensemble-mean and the observations (not shown). Individual model spatial correlations differ between the 20C3M and SRESA1B scenarios but not significantly, suggesting that spatially the leading patterns of North Pacific SSTa are statistically stationary.

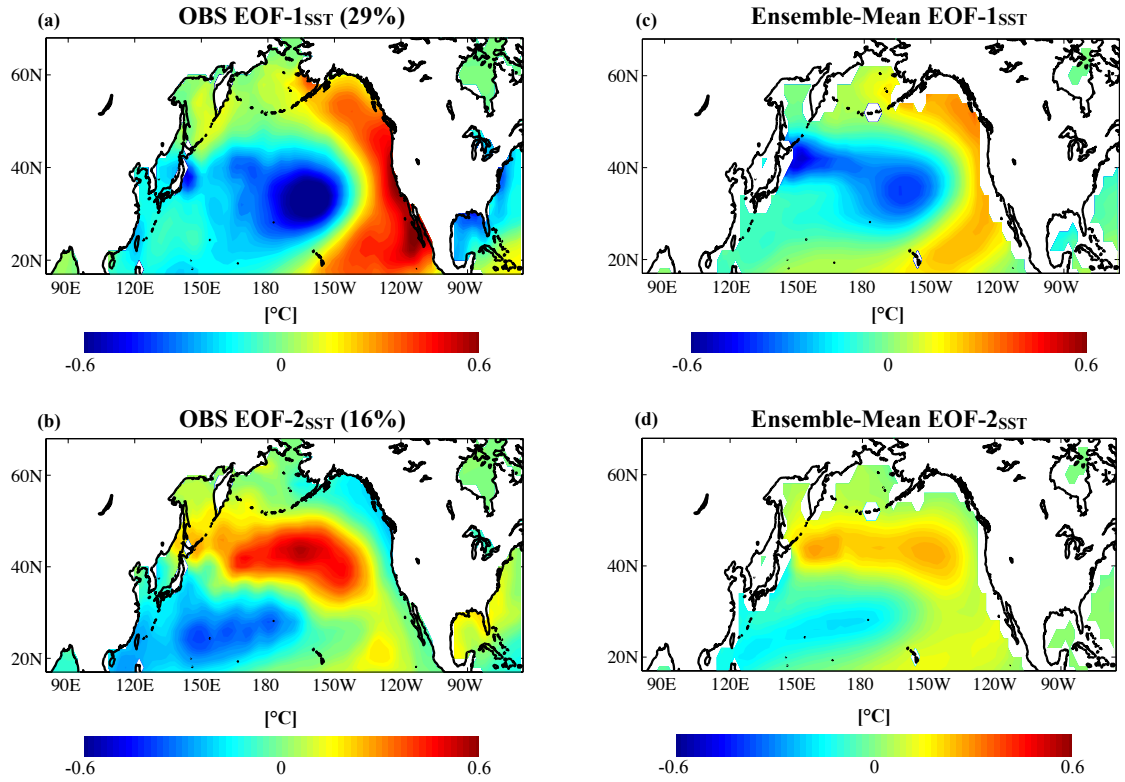

FIG. 4.1. (a) Regression of observed DJF SSTa (°C) onto the standardized first PC time series of observed North Pacific DJF SSTa. Percent variance explained by the mode is given in the title. (b) As in (a), but using the standardized second PC time series of North Pacific DJF SSTa. (c) The mean of the regression patterns of model DJF SSTa onto the standardized first PC time series of model North Pacific DJF SSTa (i.e., the ensemble-mean pattern). (d) As in (c) but for the standardized second PC time series of North Pacific DJF SSTa.

Figure 4.3 presents the power spectra for the two leading patterns of North Pacific SSTa. The ensemble-mean power spectrum of the EC-1_{SST} index of the models closely resembles that of the observations for the 20^{th} century (Fig. 4.3a). Almost all models exhibit power in the decadal (10- to 20-year) band, although to varying degrees. The BCCR-BCM2.0, the GFDL2.0, and the GISS-EH models have their strongest power in the decadal bands, while the CSIRO3.5 and the NCAR-PCM1 models exhibit weaker decadal-scale power. For the second mode (EC-2_{SST}; Fig. 4.3b), the results are less consistent with observations. The observed EC-2_{SST} index has a generally weak, broad spectrum with two significant peaks - one at 7-12 years

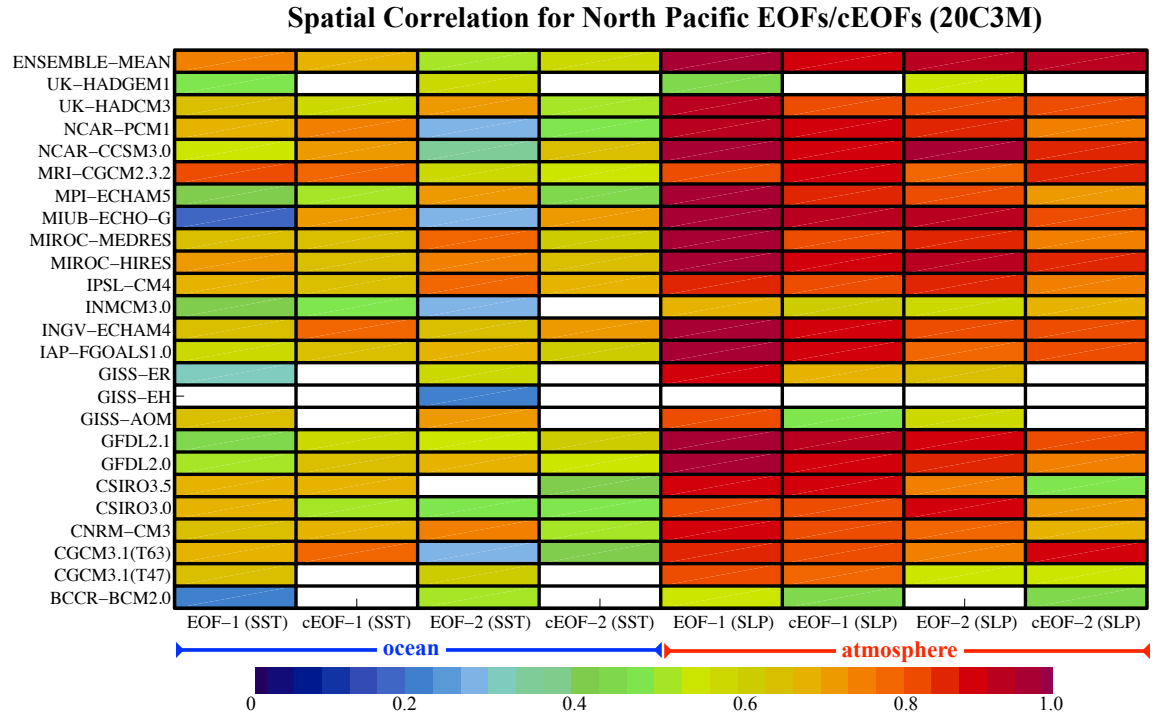

FIG. 4.2. Spatial correlations of the leading EOFs and cEOFs of North Pacific wintertime SLP and SST between the 20C3M runs of the models and observations. Only spatial correlations exceeding the 95% significance level are shaded.

and the other at 4-5 years. The ensemble-mean power spectrum, by contrast, has its maximum power in the 15-20 year band with decreasing power toward higher frequencies. Individual model members follow the characteristics of the ensemble-mean power spectrum except for the GFDL2.1 model, which captures the interannual peak seen in observations. Differences in power spectra between the 20C3M and SRESA1B scenarios for the EC-1_{SST} and EC-2_{SST} indices are insignificant in nearly every model (not shown). Only two models (the BCCR-BCM2.0 and the GISS-EH models) predict significant increases power at higher frequencies (2-5 years) for both leading modes, but since these models have low spatial correlations with observations (Fig. 4.2), we discount these results.

We also examine how much of the total variance is explained by the two leading modes of the models compared to observations. Table 4.2 presents the variance of the

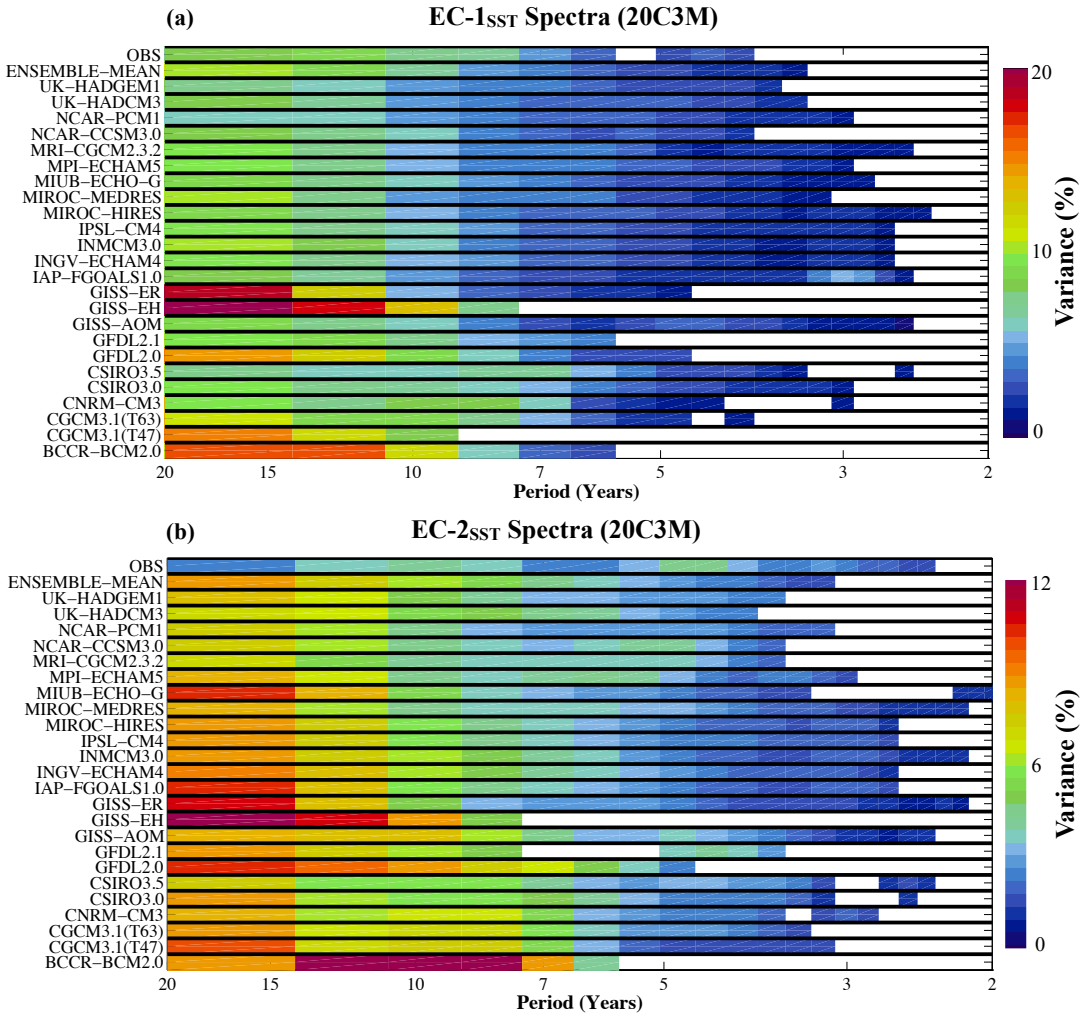

FIG. 4.3. (a) Power spectra (in percent of total variance explained) of the EC-1_{SST} index as a function of period (years) for observations, the ensemble-mean of the models, and the 20C3M runs of the IPCC models. (b) As in (a) but for the EC-2_{SST} index. Only significant power values ($p < 0.05$) are shaded.

model EC-1_{SST} and EC-2_{SST} indices (Columns 2 and 3), normalized by the variance of the observed index, for both the 20C3M and SRESA1B scenarios. This normalization facilitates comparison among the models and also between the 20C3M and SRESA1B scenarios. For the EC-1_{SST} index in the 20C3M output, most of the models have much smaller variance than the observed index, with the GISS-AOM, the GISS-ER and the MIROC-HIRES models having variances less than 10% of the observed index (Table 4.2, Column 2). Only two models have variances for their EC-1_{SST} indices greater than observed (the INMCM3.0 and NCAR-PCM1 models). By contrast, for the 20C3M

EC-2_{SST} indices (Table 4.2, Column 3), every model except for three (again, the GISS-AOM, GISS-ER, and MIROC-HIRES models) has a variance in its index larger than that in observations, ranging from double (e.g., the NCAR-CCSM3.0 model) to nearly 12 times the observed variance (the MIUB-ECHO-G model). When looking at differences between the 20C3M and SRESA1B scenarios, we find no consensus in the direction of change in variance of either index among the models, though the ensemble-mean suggests a decrease in variance for both indices.

Table 4.2. Normalized variance (i.e., actual variance divided by the variance of the same index in observations; dimensionless) of the EC-1_{SST} and EC-2_{SST} indices. Variance shown for both scenarios (20C3M/SRESA1B).

Model Name / Data	***VAR (EC-1$_{SST}$)***	***VAR (EC-2$_{SST}$)***
BCCR-BCM2.0	0.69/0.34	3.65/2.33
CGCM3.1 (T47)	0.19/0.14	1.55/1.01
CGCM3.1 (T63)	0.25/0.18	1.17/0.78
CNRM-CM3	0.70/0.58	3.52/4.29
CSIRO3.0	0.10/0.11	1.22/1.74
CSIRO3.5	0.25/0.08	1.41/1.81
GFDL2.0	0.63/1.25	6.50/4.72
GFDL2.1	0.38/0.14	6.07/1.14
GISS-AOM	0.02/0.04	0.40/0.49
GISS-EH	0.54/0.29	5.07/3.28
GISS-ER	0.05/0.09	0.55/0.74
IAP-FGOALS1.0	1.00/0.56	8.95/2.89
INGV-ECHAM4	0.21/0.04	2.29/0.20
INMCM3.0	1.83/0.97	7.42/6.78
IPSL-CM4	0.33/0.15	1.32/2.07
MIROC-HIRES	0.08/0.11	0.70/1.11
MIROC-MEDRES	0.13/0.26	1.27/2.37
MIUB-ECHO-G	0.82/0.53	11.94/9.36
MPI-ECHAM5	0.66/0.69	7.43/7.00
MRI-CGCM2.3.2	0.87/0.81	4.12/3.37
NCAR-CCSM3.0	0.58/0.67	2.08/2.45
NCAR-PCM1	1.37/1.03	8.10/5.51
UK-HADCM3	0.55/0.77	4.56/2.27
UK-HADGEM1	0.35/0.27	4.16/5.34
Ensemble-Mean	0.53/0.42	3.98/3.04
Observations	1.00	1.00

4.4 Relations Between North Pacific Atmospheric and Oceanic Variability

The leading modes of North Pacific SSTa variability are a combination of both intrinsic variability in the ocean and a response to external forcing by the overlying extratropical atmosphere (e.g., Pierce et al. 2001; Miller et al. 2004; Chhak et al. 2009). For coupled climate models to capture NPDV accurately, we should expect that similar covariances and ocean-atmosphere dynamical links exist in the models. This section offers tests for the covariability between SLPa and SSTa in the North Pacific and an AR-1 model to evaluate the degree of forcing the North Pacific atmospheric circulation contributes to the forcing of the dominant modes of oceanic variability in the region.

4.4.1 Leading Modes of North Pacific SLPa

Before performing an analysis of the coupled ocean/atmosphere modes of variability in the North Pacific, we compare the leading patterns of atmospheric variability in the SLPa fields for each model to observations. Figure 4.4 shows the leading two EOFs of North Pacific DJF SLPa in observations (Figs. 4.4a and 4.4b) and in the ensemble-mean of the models (Figs. 4.4c and 4.4d). EOF-1_{SLP} for observations (Fig. 4.4a) clearly depicts the AL, with a monopole of strong negative anomalies situated south of the Aleutian Islands. The AL mode explains nearly 30% of the total variance in wintertime SLPa in the North Pacific. By contrast, EOF-2_{SLP} displays the canonical NPO pattern (Walker and Bliss, 1932; Rogers, 1981) with a dipole in pressure between Alaska and just north of Hawaii (Fig. 4.4b). The ensemble-mean leading two EOF patterns of North Pacific SLPa (Figs. 4.4c and 4.4d) are very close to their observational counterparts, though the magnitudes are halved. Moreover, the spatial correlations of the leading two EOFs of North Pacific SLPa in the models versus the observations are high and significant (Fig. 4.2) and typically higher than the North

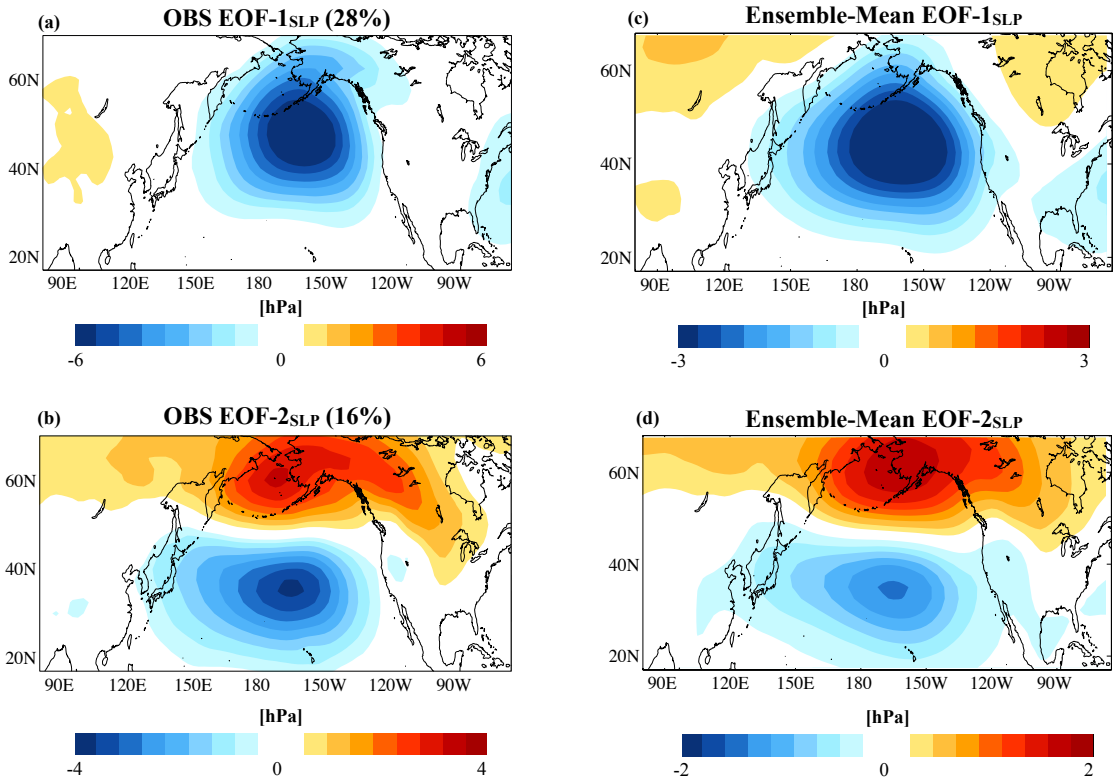

FIG. 4.4. (a) Regression of observed DJF SLPa (hPa) onto the standardized first PC time series of observed North Pacific DJF SLPa. Percent variance explained by the mode is given in the title. (b) As in (a), but using the standardized second PC time series of North Pacific DJF SLPa. (c) The mean of the regression patterns of model DJF SLPa onto the standardized first PC time series of model North Pacific DJF SLPa (i.e., the ensemble-mean pattern). (d) As in (c) but for the standardized second PC time series of North Pacific DJF SLPa. Note that the colorbars in (c) and (d) represent values half of those in (a) and (b).

Pacific SST EOFs. The power spectra of the leading two SLP EOFs in the models compare well with the observations with a broad range of low power for low and high frequencies (not shown). There is no statistically significant difference between the ensemble-mean and observed power spectrum for either the EC-1_{SLP} or EC-2_{SLP} index (not shown).

4.4.2 Coupled Patterns of Variability in the North Pacific Ocean and Atmosphere

Figure 4.5 displays the two leading cEOF patterns between North Pacific SLPa and SSTa in observations during boreal winter. Together, the first two patterns explain 38% of the covariability in the two variables. The first pattern is dominated by a broad area of negative SLPa in the central and eastern North Pacific basin residing to the south and east of the climatological center of the AL (Fig. 4.5a). The corresponding SSTa pattern (Fig. 4.5b) resembles the positive phase of the PDO displayed in Fig. 4.1a ($r = 0.98; p < 0.01$). Moreover, the cEC-1_{SST} and EC-1_{SST} indices are correlated at $r = 0.99\,(p < 0.01)$. For cEOF-2, the SLPa pattern (Fig. 4.5c) resembles the NPO signature previously shown in Fig. 4.4b. The covarying SSTa pattern (Fig. 4.5d) portrays cold anomalies stretching from the southwestern North Pacific towards the northeast, surrounded by warm anomalies extending from the Kamchatka Peninsula southeastward toward North America and around to Hawaii. The spatial pattern is highly similar to that in Fig. 4.1b ($r = 0.89; p < 0.01$), although there is a notable difference in the magnitude of the positive anomaly in the northernmost Pacific and in the positive anomalies in the subtropical North Pacific. When the spatial pattern in Fig. 4.5d is compared to the NPGO SSTa regression pattern (Fig. 1.2c), the spatial correlation is $r = 0.76\,(p < 0.01)$. Moreover, the cEC-2_{SST} index is significantly correlated with the EC-2_{SST} index ($r = 0.88; p < 0.01$) and the NPGO index ($r = 0.60; p < 0.01$).

When performing the same cEOF analysis on the 20C3M model output, we find substantial differences in the SLPa and SSTa fields in the two leading cEOF patterns (Figure 4.6). The ensemble-mean patterns of SST and SLP for cEOF-1 (Figs. 4.6a and b) resemble overall those of the observations (spatial correlations shown in Fig. 4.2), albeit with two major differences: (1) the representation of the AL is oriented more zonally in the ensemble-mean pattern and encompasses most

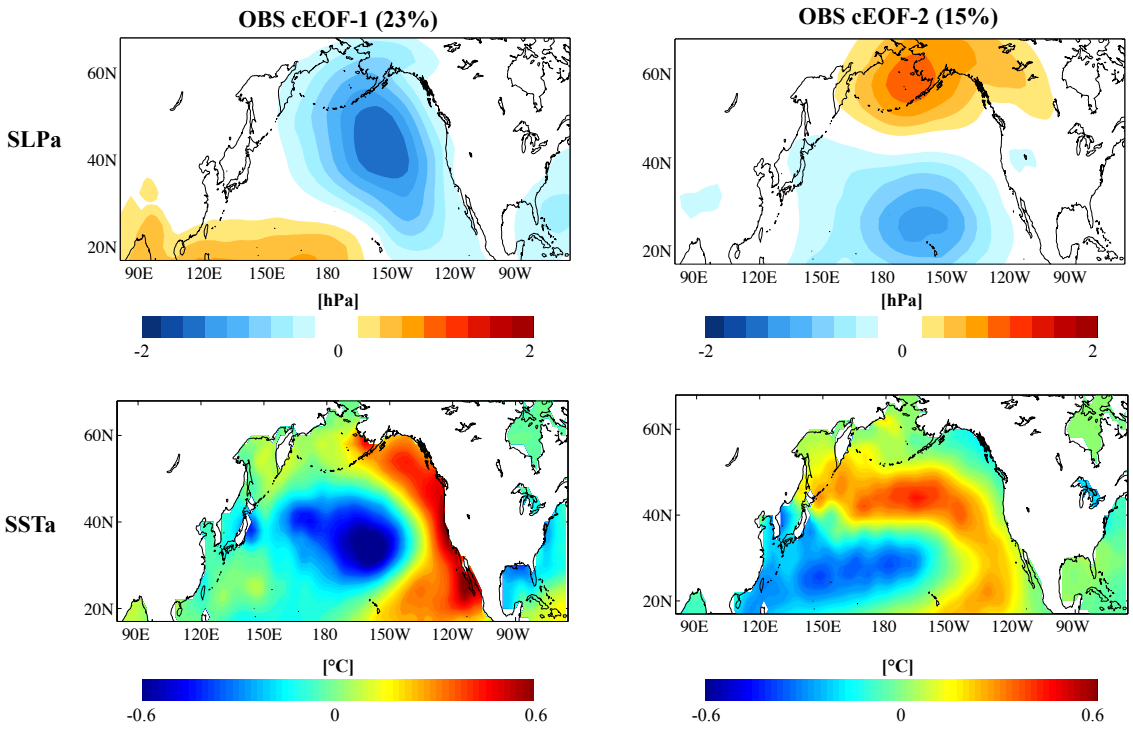

FIG. 4.5. Regression of observed DJF (a) SLPa (hPa) and (b) SSTa (°C) onto the standardized first PC time series of the cEOF analysis of North Pacific DJF SLPa/SSTa. Percent covariance explained by the mode is given in the title. (c) As in (a), but using the standardized second PC time series of the cEOF analysis of North Pacific DJF SLPa/SSTa. (d) As in (b) but using the standardized second PC times series of the cEOF analysis of North Pacific DJF SLPa/SSTa.

of the North Pacific basin with its center of action displaced towards the west; and (2) the SSTa pattern displays an elongated southwest-northeast negative pole, unlike the concentrated negative pole prominent in the observations (Fig. 4.5b). For cEOF-2, the SLPa pattern (Fig. 4.6c) is significantly correlated with the observations ($r = 0.90$; $p < 0.01$) with the typical dipole structure of the NPO. In the SSTa field (Fig. 4.6d), the ensemble-mean SSTa pattern of cEOF-2 displays a weak tripole, and the positive anomalies do not extend into the eastern subtropical Pacific as in the observations. The spatial correlation between the ensemble-mean EOF-1_{SST} (EOF-2_{SST}) and cEOF-1_{SST} (cEOF-2_{SST}) is $r = 0.78$ ($r = 0.59$), which is significant at the 99% (95%) level.

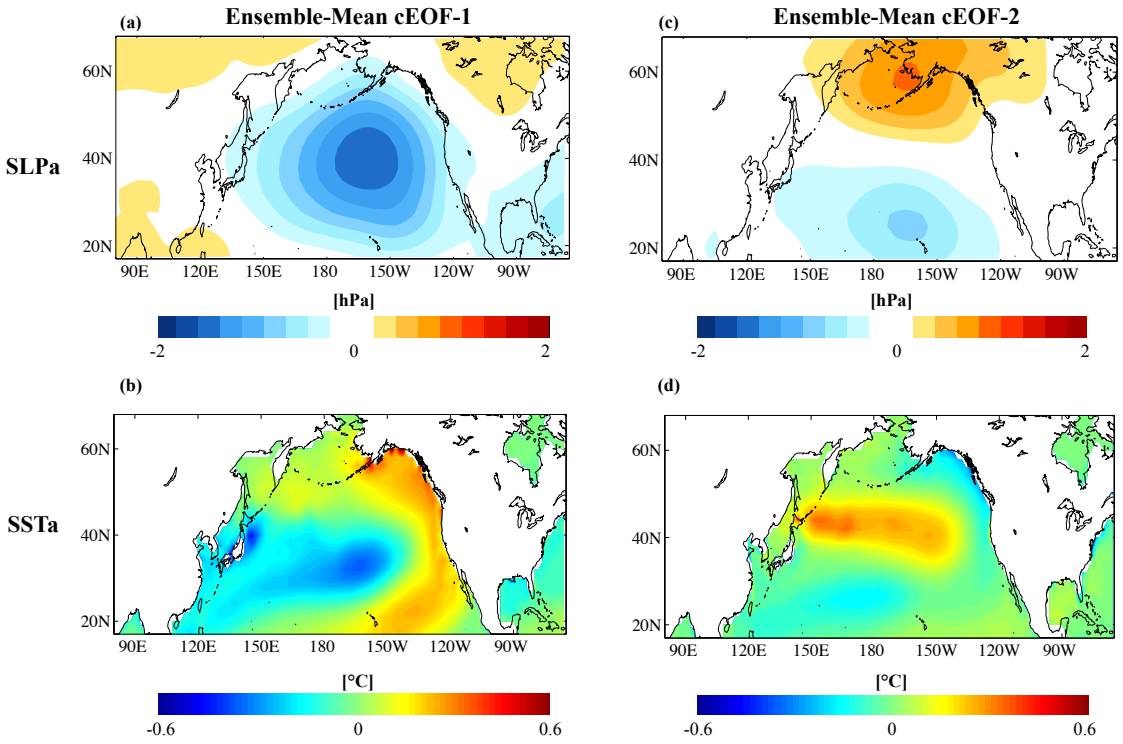

FIG. 4.6. The ensemble-mean regression maps of the model North Pacific DJF (a) SLPa (hPa) and (b) SSTa (°C) fields onto the standardized first PC time series of the cEOF analysis of North Pacific DJF SLPa/SSTa. (c) As in (a), but using the standardized second PC time series of the cEOF analysis of North Pacific DJF SLPa/SSTa. (d) As in (b) but using the standardized second PC times series of the cEOF analysis of North Pacific DJF SLPa/SSTa. Results are shown for the 20C3M runs.

When comparing cEOF-1_{SST} and cEOF-2_{SST} from each model with observations (Fig. 4.2) we generally find weaker correlations than the ones obtained by comparing the SST patterns inferred from the traditional EOF analysis. Six of the 24 models display insignificant spatial correlations for both cEOF-1_{SST} and cEOF-2_{SST} (Fig. 4.2). For the atmospheric cEOF patterns, spatial correlations are generally higher than the oceanic cEOF patterns, though four models have insignificant spatial correlations for cEOF-2_{SLP} (Fig. 4.2, Column 8). As with the North Pacific SSTa EOFs, the cEOF patterns in both SLPa and SSTa remain unchanged spatially when examining the SRESA1B output.

4.4.3 Reconstructing the cEC-1_{SST} and cEC-2_{SST} Indices Using a Simple AR-1 Model

The atmospheric patterns depicted in the cEOF analyses are also dynamically linked to the leading modes of North Pacific SSTa variability. Latif and Barnett (1996) and Pierce et al. (2001) suggested that the leading pattern of North Pacific SSTa variability (i.e., the PDO) is forced through stochastic atmospheric forcing, primarily that due to the AL. Chhak et al. (2009) used output from an ocean model to illustrate that NPGO variability is forced, at least in part, by variability in the NPO. Given the similarities between the PDO/cEOF-1_{SST} and the NPGO/cEOF-2_{SST} in observations, we employ a simple AR-1 model to check for consistency between the atmospheric forcing patterns and North Pacific SSTa variability. This test solely explores the degree to which the atmospheric forcing patterns are connected to the underlying covarying SSTa patterns in both the observations and models. The AR-1 model equations are:

$$\frac{d\left(cEC\text{-}1_{\mathrm{SST-rec}}\right)}{dt} = \beta_{cEC\text{-}1} AL\left(t\right) - \frac{cEC\text{-}1_{\mathrm{SST-rec}}}{\tau_{cEC\text{-}1}} + \epsilon_1\left(t\right), \tag{4.1}$$

$$\frac{d\left(cEC\text{-}2_{\mathrm{SST-rec}}\right)}{dt} = \beta_{cEC\text{-}2} NPO\left(t\right) - \frac{cEC\text{-}2_{\mathrm{SST-rec}}}{\tau_{cEC\text{-}2}} + \epsilon_2\left(t\right). \tag{4.2}$$

where $AL\left(t\right)$ and $NPO\left(t\right)$ are defined as the cEC-1_{SLP} and cEC-2_{SLP} time series, respectively, $\epsilon\left(t\right)$ represents white noise, and the subscript "*rec*" indicates that the indices are the reconstructed versions of the original indices. The coefficients (τ_{cEC-1}, τ_{cEC-2}, β_{cEC-1} and β_{cEC-2}) are determined using least squares fitting. A simple Euler forward time step scheme is used in solving (4.1) and (4.2).

Figures 4.7 and 4.8 show the results of the AR-1 model for the cEC-1_{SST} (Fig. 4.7) and cEC-2_{SST} (Fig. 4.8) indices. In observations, the results indicate that AL variability accounts for about 32% of the variance of the cEC-1_{SST} index (Fig. 4.7a), while NPO variability contributes to about 40% of the variance of the cEC-2_{SST}

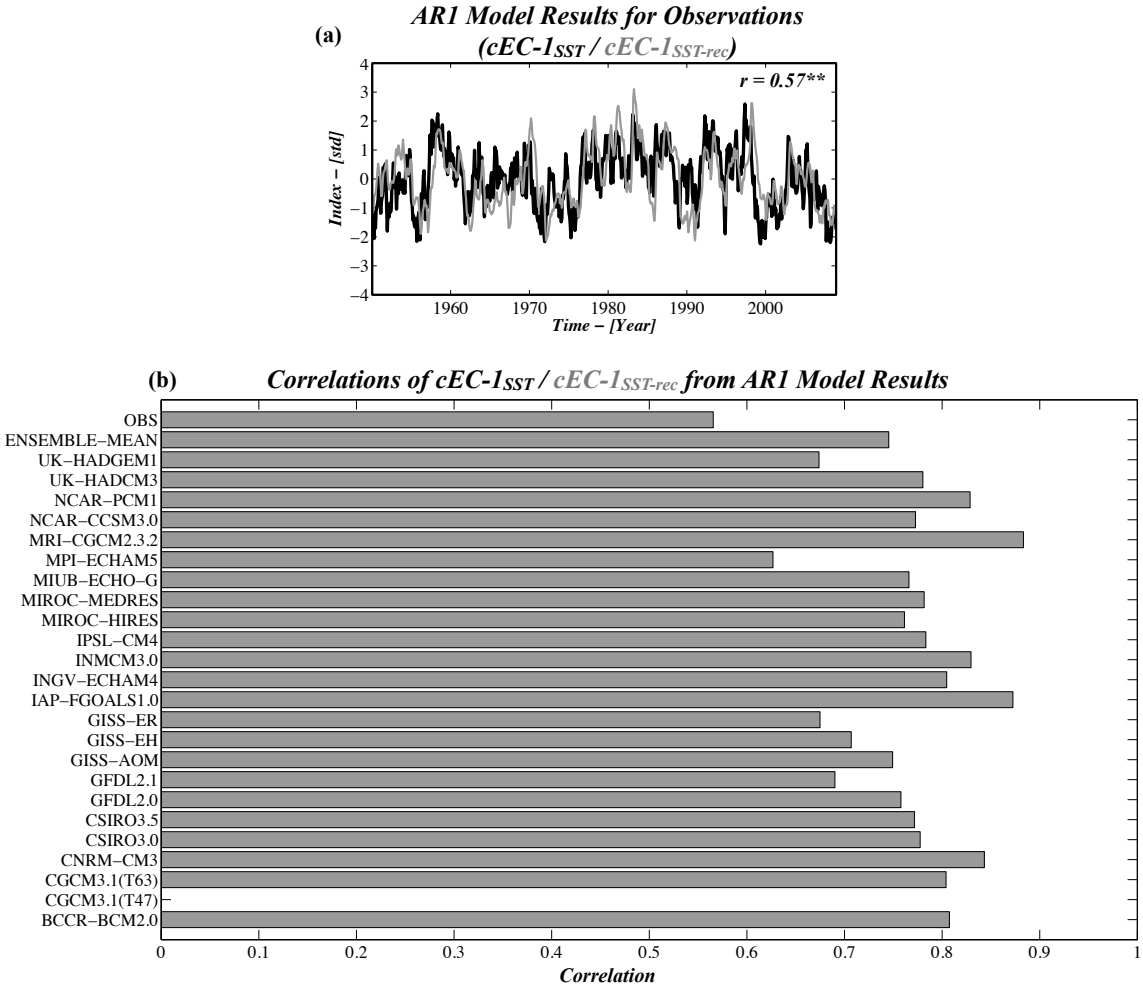

FIG. 4.7. (a) The observed cEC-1_{SST} index (black line) and the cEC-$1_{\mathrm{SST-rec}}$ index (gray line) from the AR-1 model. Correlation between the cEC-1_{SST} and cEC-$1_{\mathrm{SST-rec}}$ indices is shown and is highly significant ($p < 0.01$). (b) Correlations between the cEC-1_{SST} and cEC-$1_{\mathrm{SST-rec}}$ indices for the observations, the ensemble-mean, and all 24 models for their 20C3M runs. Only correlations exceeding the 95% significance level are plotted.

index (Fig. 4.8a). For the cEC-1_{SST} index in the models (Fig. 4.7b), every model but one (the CGCM3.1 (T47) model - $r = 0.14$) shows significant ($p < 0.05$) correlations between their cEC-1_{SST} and cEC-$1_{\mathrm{SST-rec}}$ indices. Significant correlation values range from $r = 0.63$ for the MPI-ECHAM5 model to $r = 0.88$ for the MRI-CGCM2.3.2 model. The ensemble-mean correlation for the reconstruction of the cEC-1_{SST} index with the AR-1 model is $r = 0.75$, or 56% of total variance explained.

For the cEC-2_{SST} index (Fig. 4.8b), less reproducibility exists. Seven of the

24 models (the BCCR-BCM2.0, CGCM3.1 (T47), CGCM3.1 (T63), GISS-EH, IAP-FGOALS1.0, INMCM3.0, and NCAR-CCSM3.0 models) have small, insignificant correlations. The remaining models show significant ($p < 0.05$) correlations ranging from $r = 0.24$ for the CNRM-CM3 model to $r = 0.74$ for the MIROC-HIRES model. The mean correlation among all models for the reconstruction of the cEC-2_{SST} index is $r = 0.47$, or 22% of total variance explained, which is considerably lower than the correlation derived from observations ($r = 0.63$, or 40% of variance explained). This

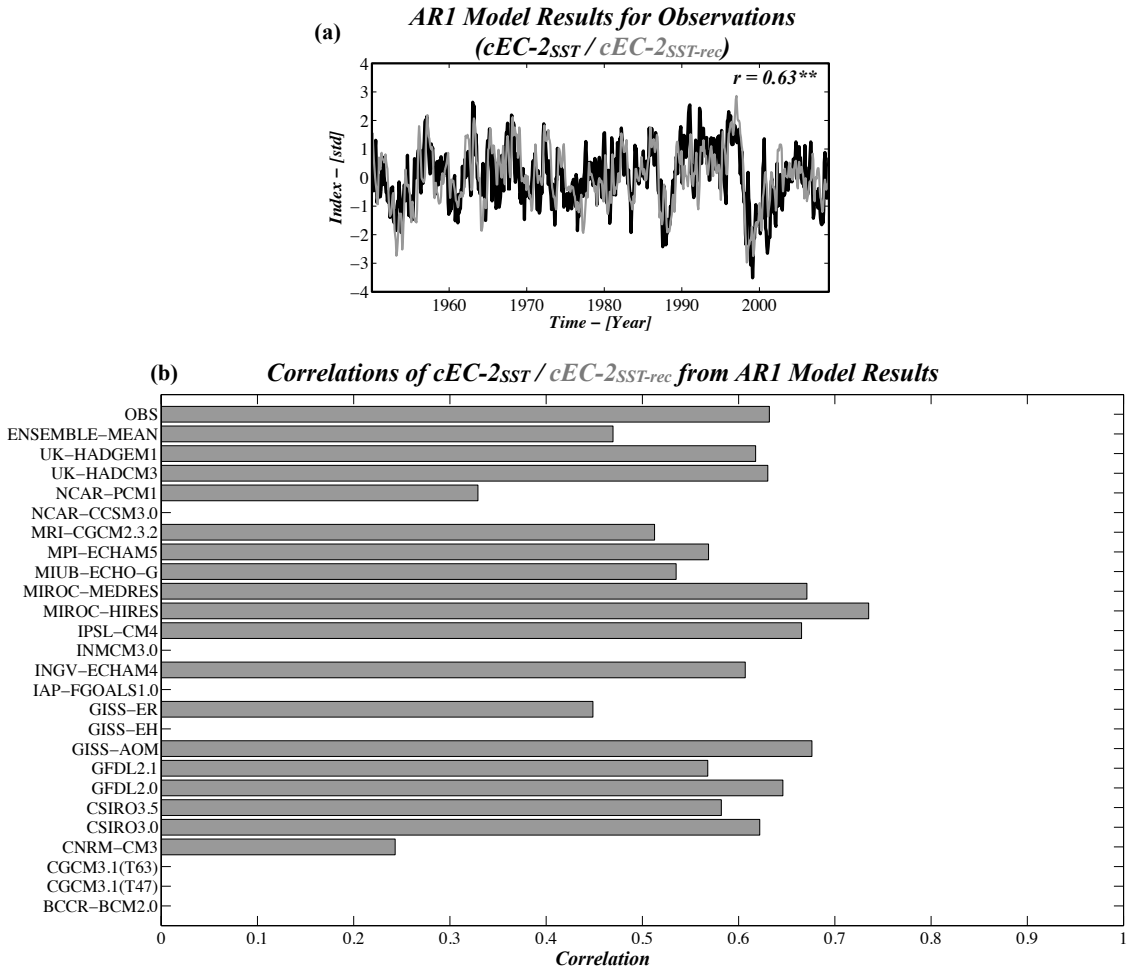

FIG. 4.8. (a) The observed cEC-2_{SST} index (black line) and the cEC-$2_{\mathrm{SST-rec}}$ index (gray line) from the AR-1 model. Correlation between the cEC-2_{SST} and cEC-$2_{\mathrm{SST-rec}}$ indices is shown and is highly significant ($p < 0.01$). (b) Correlations between the cEC-2_{SST} and cEC-$2_{\mathrm{SST-rec}}$ indices for the observations, the ensemble-mean, and all 24 models for their 20C3M runs. Only correlations exceeding the 95% significance level are plotted.

result suggests that cEOF-2_{SST} is less consistent with direct atmospheric forcing by the NPO in the models than what is observed.

Table 4.3 shows the τ values derived for the AR-1 model results. For the cEC-1_{SST} index, $\tau_{cEC\text{-}1}$ values for all of the models except for the CGCM3.1 (T47) model are smaller than that seen in observations (10.2 months), with the ensemble-mean $\tau_{cEC\text{-}1}$ equal to 6.2 months. The lower-than-observed $\tau_{cEC\text{-}1}$ values suggest that the SST in the coupled models exhibit less memory in their leading mode of North Pacific SSTa, allowing more of the high-frequency atmospheric forcing (i.e., the AL) to contribute and drive the oceanic signal. For the cEC-2_{SST} reconstruction, the ensemble-mean value for $\tau_{cEC\text{-}2}$ is 8.8 months, which is larger than that from observations (5.8 months). For individual models, the six models with the largest values of $\tau_{cEC\text{-}2}$ are also those models with insignificant correlations in the AR-1 model test (Fig. 4.8b). This suggests that these coupled models generally exhibit more memory in the second covariability climate pattern in SSTa and have less dependence on high frequency NPO forcing. This conclusion is also supported by Fig. 4.3b - recall that the maximum power for the models is generally concentrated at periods greater than 10 years, unlike the double-peak at decadal and interannual time scales in the observed spectrum.

Studies of North Pacific SST variability have identified reemergence as a significant component contributing to NPDV (e.g., Alexander et al. 1999; Deser et al. 2003). Indeed, the presence of reemergence means that North Pacific SST variability in general cannot be modeled entirely as an AR-1 process, but the leading modes and coupled modes of variability may still contain a significant component related to an AR-1 process. For example, in using the same AR-1 model as (4.1) but using the EC-1_{SLP} time series as the forcing, $\beta = 1$, and $\tau = 5$ months (i.e., the decorrelation timescale for the PDO index), the correlation between the actual PDO index and the reconstruction is $r = 0.64$, which is significant at the 99% level. Thus, nearly 41% of

Table 4.3. Values of τ (months) for each model and the observations used in the AR-1 model.

Model Name / Data	$\tau_{cEC\text{-}1}$ *(months)*	$\tau_{cEC\text{-}2}$ *(months)*
BCCR-BCM2.0	6.2	15.7
CGCM3.1 (T47)	11.2	15.6
CGCM3.1 (T63)	6.7	19.8
CNRM-CM3	6.3	9.7
CSIRO3.0	5.3	7.2
CSIRO3.5	7.4	6.7
GFDL2.0	8.5	7.4
GFDL2.1	6.6	7.0
GISS-AOM	3.1	3.9
GISS-EH	5.2	17.7
GISS-ER	4.4	6.8
IAP-FGOALS1.0	8.3	12.4
INGV-ECHAM4	5.7	5.7
INMCM3.0	6.5	11.5
IPSL-CM4	7.2	5.0
MIROC-HIRES	4.1	3.2
MIROC-MEDRES	6.2	5.4
MIUB-ECHO-G	6.2	8.9
MPI-ECHAM5	6.3	8.6
MRI-CGCM2.3.2	5.1	6.7
NCAR-CCSM3.0	7.8	7.2
NCAR-PCM1	3.5	4.8
UK-HADCM3	6.1	8.0
UK-HADGEM1	4.0	6.5
Ensemble-Mean	6.2	8.8
Observations	10.2	5.8

the variability in the PDO index can be captured with the simple AR-1 model using AL variability as forcing. To test if the assumption of an AR-1 process is consistent with the cECs, Figure 4.9 presents the winter-to-winter ACFs for the cEC-1_{SST} index (Fig. 4.9a) and the cEC-2_{SST} index (Fig. 4.9b) for the observations (red line), the individual models (gray lines), and the ensemble-mean ACF (black line). For the models, there is a lot of spread amongst the ACFs (Fig. 4.9a, gray lines), though most of the models appear to have a simple exponential decay in their ACFs. For

the observed cEC-1_{SST} index, the decay in the ACF over time is punctuated by brief bumps at lags of 5 and 10 years, which fall within the model ACF spread and are not statistically significant according to a Monte Carlo test. Some of the model ACFs exhibit some signature of longer-term memory, but the ensemble-mean ACF of the cEC-1_{SST} index (Fig. 4.9a, black line) displays a strictly exponential decay, which offers evidence that the AR-1 modeling approach is adequate to explore the relationship between the atmospheric forcing and oceanic response in the cECs.

The ACFs for the cEC-2_{SST} index (Fig. 4.9b) indicate some consistency with our previous observation of longer-term memory of the second leading SST covariability pattern in the models. Note that for short lags (less than 4 years), the ensemble-mean ACF of the cEC-2_{SST} time series generally has a slower rate of decay than the observed (black line compared to the red line in Fig. 4.9b). These higher correlations in the ensemble-mean ACF do indicate that the model has less dependency on atmospheric forcing for this mode of variability than observations would suggest. For later lags, the ensemble-mean ACF continually decays slowly yet still exponentially toward zero and remains close to zero at later lags, while the observed ACF rebounds toward positive correlations after a lag of 10 years (Fig. 4.9b). The individual models have a more complicated structure, however, with most of them showing positive (and negative) correlations extending out past 10-15 year lags. Indeed, the ensemble-mean ACF at large lags reflects the spread in positive and negative correlations there, resulting in an ensemble-mean ACF that hovers near zero.

In summary, the AR-1 model results suggest that the models are strongly influenced by the AL in driving their leading SSTa covariability pattern, but are less dependent on atmospheric forcing for their second leading SSTa covariability mode. Both of these results are somewhat contrary to the observational results and thus suggest issues with the ways the ocean components of the models integrate forcing from the overlying North Pacific atmosphere.

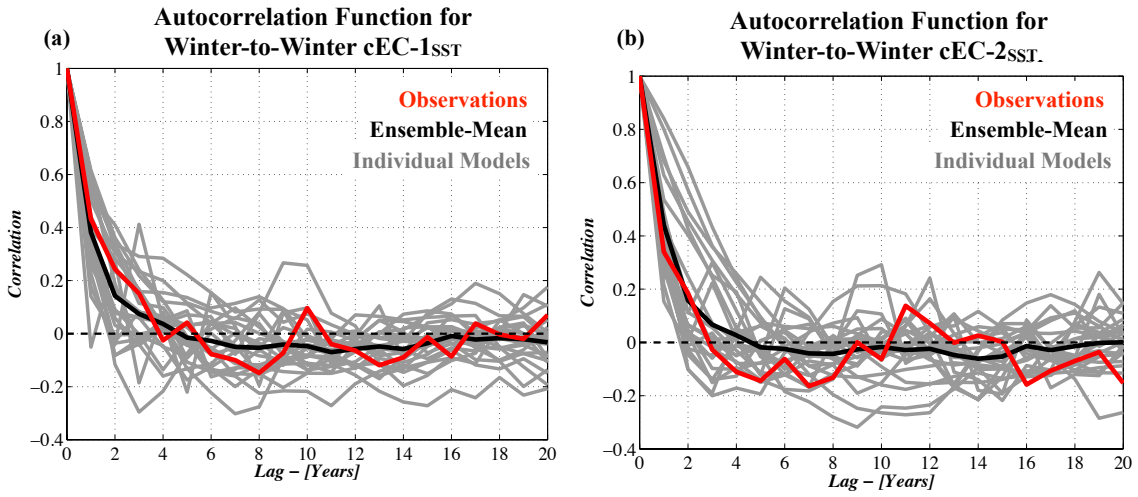

FIG. 4.9. (a) The winter-to-winter ACF (lags in years) of the cEC-1_{SST} index for the observations (red), ensemble-mean (black), and the 24 individual models (gray lines). (b) As in (b) but for the cEC-2_{SST} index. Dashed black line indicates $r = 0$.

4.5 Connections Between Tropical Pacific Climate Variability and NPDV in the Models

4.5.1 Observational Evidence

The previous two sections evaluated how extratropical variability of the atmosphere and ocean affect NPDV representation in the IPCC models. We now shift focus to examining how the models capture the relationship between tropical Pacific climate variability and NPDV. This link is important because a significant fraction of variability in NPDV can be explained from tropical Pacific oceanic and atmospheric variability (e.g., Alexander et al. 2002; Deser et al. 2004; Schneider and Cornuelle 2005; Alexander et al. 2008; Di Lorenzo et al. 2010). These links are primarily established by an atmospheric bridge whereby changes in the Hadley cell and the location and intensity of tropical convection are teleconnected to the mid-latitude atmosphere and ocean. For example, canonical ENSO activity projects onto the variability of the AL and is integrated by the ocean, providing a mechanism that drives the PDO (e.g., Alexander et al. 2002; Newman et al. 2003). The results and conclusions obtained in Chapter 3 also illustrate that tropical Pacific variability associated with the

CPW phenomenon has substantial impacts on NPDV in both the atmosphere (NPO variability) and the ocean (NPGO).

Given that the characteristics of NPDV in the short observational record are strongly connected dynamically to tropical variability, we implement a simple analysis to extract the statistical signature of the links between canonical ENSO and CPW variability and the patterns of NPDV to test in the climate models. Figure 4.10 shows the regressions of wintertime SLPa and SSTa on the EC-$1_{\mathrm{Tropics-SST}}$ and EC-$2_{\mathrm{Tropics-SST}}$ indices (calculated from projection of monthly tropical Pacific SSTa onto EOF-$1_{\mathrm{Tropics-SST}}$ and EOF-$2_{\mathrm{Tropics-SST}}$, respectively). The thick gray line in all plots denotes where correlations are significant ($p < 0.05$). The SLPa regression pattern with the EC-$1_{\mathrm{Tropics-SST}}$ index (Fig. 4.10a) displays the east-west dipole of negative-positive SLPa indicative of changes in the Walker circulation during warm ENSO events. Moreover, negative anomalies exist in the AL region (compare the North Pacific sector of Fig. 4.10a with Fig. 4.5a). Almost the entire North Pacific and tropical Pacific basin (minus a section through the central portion) exhibit significant correlations with the leading mode of tropical Pacific SSTa.

In the SSTa regression field (Fig. 4.10b), the canonical ENSO pattern is visible in the tropical Pacific. In the North Pacific, the SSTa regression pattern has spatial characteristics similar to EOF-1_{SST} (Fig. 4.1a) and cEOF-1_{SST} (Fig. 4.5b). Together, these two figures are consistent with previous studies showing that the leading mode of tropical Pacific SSTa impacts the leading modes of SLPa and SSTa in the North Pacific. Indeed, the correlation between the EC-$1_{\mathrm{Tropics-SST}}$ and EC-1_{SST} indices is 0.56, which is highly significant ($p < 0.01$).

Figs. 4.10c and 4.10d illustrate the relationship between the EC-$2_{\mathrm{Tropics-SST}}$ index and SLPa and SSTa in the Pacific basin. For SLPa (Fig. 4.10c), a dipole in the North Pacific exists and closely resembles the NPO-like pattern in Fig. 4.5c. The

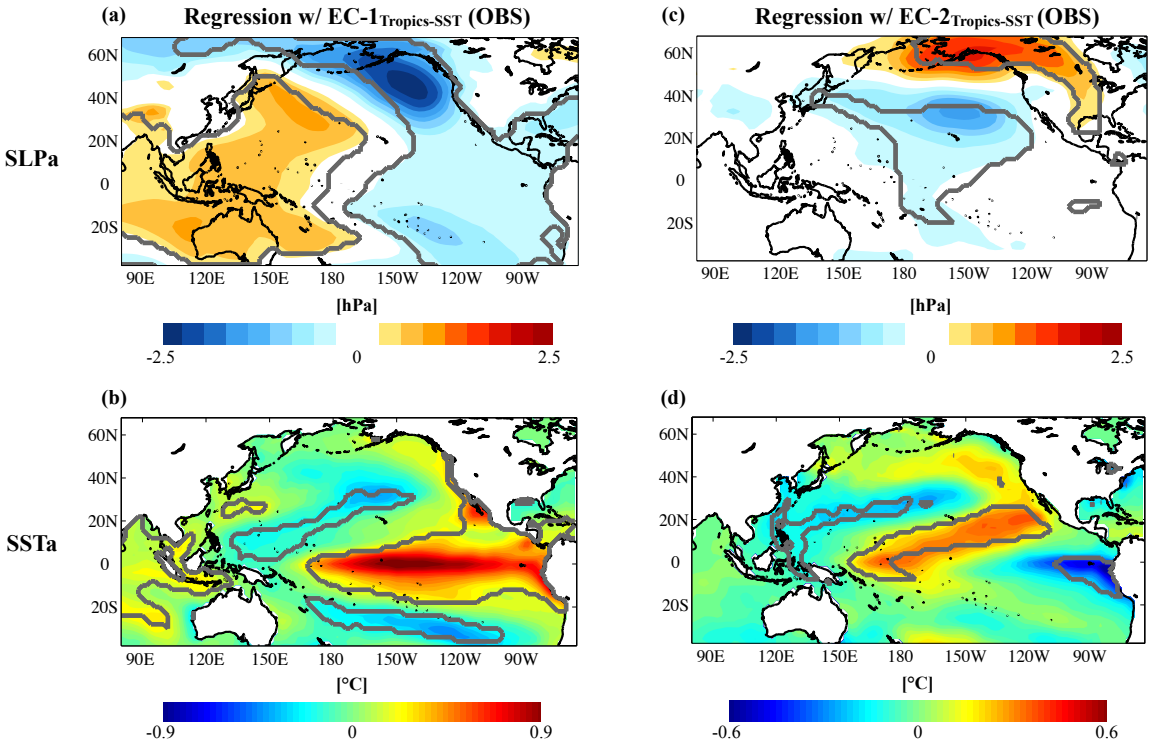

FIG. 4.10. (a) Regression of observed DJF SLPa (hPa) on the standardized EC-$1_{\text{Tropics}-\text{SST}}$ index. Thick gray line outlines region where correlation coefficients exceed the 95% significance level. (b) As in (a) but for DJF SSTa (°C). (c) Regression of observed DJF SLPa (hPa) on the standardized EC-$2_{\text{Tropics}-\text{SST}}$ index. Thick gray line as in (a). (d) As in (c) but for DJF SSTa (°C).

positive and significant anomalies across Alaska extend into central North America, which coincides with the baroclinic expression of the NPO on North American weather (Linkin and Nigam, 2008). For the SSTa field (Fig. 4.10d), the regression pattern in the North Pacific resembles cEOF-2_{SST} (Fig. 4.5d). When comparing the EC-$2_{\text{Tropics}-\text{SST}}$ and cEC-2_{SST} indices, the correlation is $r = 0.38$, which is significant ($p < 0.01$) but not high. In the tropical Pacific, positive SSTa extend from the subtropical North Pacific into the central and central-western tropical Pacific Ocean, with opposing negative anomalies in the far eastern tropical Pacific. Significance is restricted to the subtropical North Pacific and tropical Pacific features of the pattern.

4.5.2 Model Representation of Tropical Pacific-North Pacific Teleconnections

The same analysis presented in Fig. 4.10 is repeated for the 20C3M runs of the models, and the ensemble-mean regression patterns are displayed in Figure 4.11. The ensemble-mean SLPa regression pattern associated with the leading mode of tropical Pacific SSTa in the models (Fig. 4.11a) displays the east-west dipole in SLPa across the tropical Pacific, although at a weaker scale (note the different colorbars between Figs. 4.10 and 4.11). In the North Pacific, the SLPa pattern matches closely with its observational counterpart (Fig. 4.10a). However, unlike the observations, this North Pacific signal does not project onto the mean location of the AL in the models (see Fig. 4.6a). Moreover, the SLPa in the North Pacific sector is void of significant correlations throughout the basin. This lack of significant correlations in the ensemble-mean pattern is related to the differences among the models in the placement and magnitude of the North Pacific SLPa response. In the SSTa field (Fig. 4.11b), the canonical ENSO pattern is present in the tropical Pacific Ocean though in a much narrower band than in the observations. However, the North Pacific SSTa has no coherent regression pattern and thus no significant correlations. Hence, Figs. 4.11a and 4.11b indicate that the IPCC models generally have little dependence between their leading mode of tropical Pacific SSTa variability and North Pacific climate variability - a finding that echoes previous results by Newman (2007).

Figs. 4.11c and 4.11d show the ensemble-mean regression patterns of SLPa and SSTa with the EC-$2_{\mathrm{Tropics-SST}}$, respectively. The SLPa regression pattern (Fig. 4.11c) has substantial differences in structure in the North Pacific from observations. The SLPa pattern shows a broad region of negative anomalies throughout the central North Pacific with positive anomalies across northwest Canada and Alaska. This pattern contrasts strongly with the NPO-like pattern seen in Fig. 4.10c and its North American signature. Almost no area in the Pacific basin has significant correlations in

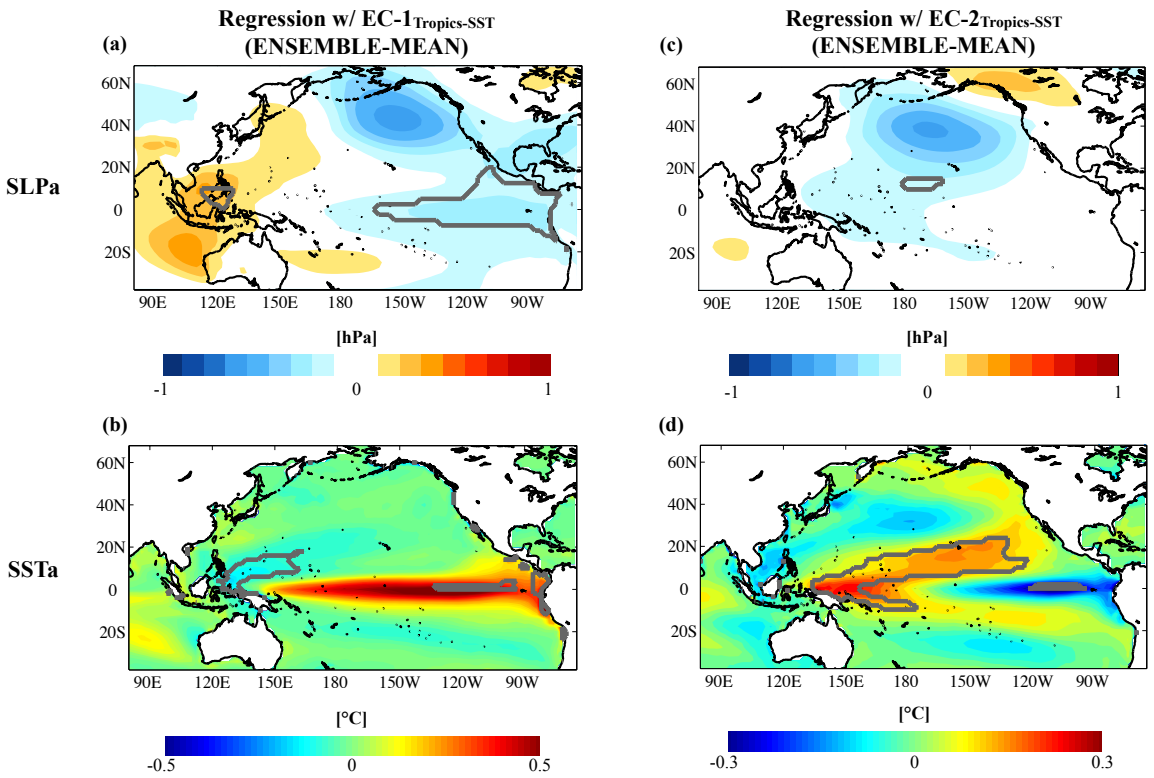

FIG. 4.11. (a) Ensemble-mean regression pattern of DJF SLPa (hPa) on the standardized EC-$1_{\text{Tropics}-\text{SST}}$ index. Thick gray line outlines region where correlation coefficients exceed ± 0.2. (b) As in (a) but for DJF SSTa (°C). (c) Ensemble-mean regression pattern of DJF SLPa (hPa) on the standardized EC-$2_{\text{Tropics}-\text{SST}}$ index. Thick gray line as in (a). (d) As in (c) but for DJF SSTa (°C).

the SLPa field, again reflecting the lack of consistency among the different models for the atmospheric response to EOF-$2_{\text{Tropics}-\text{SST}}$. The ensemble-mean SSTa regression pattern shows the core of tropical Pacific warming displaced into the Warm Pool region. Moreover, in the North Pacific, the SSTa regression pattern displays a pattern that resembles more the ensemble-mean EOF-1_{SST} than the ensemble-mean EOF-2_{SST} or cEOF-2_{SST} structures (Figs. 4.1d and 4.6d). Though insignificant in the ensemble-mean, this difference suggests that variability associated with the leading mode of North Pacific SSTa may have important connections with the *second* leading mode of tropical Pacific SSTa in many of the models.

For each model we explore in more detail the link between the two modes of tropical Pacific SSTa variability and the leading mode of North Pacific SSTa (i.e.,

the PDO) by correlating the EC-$1_{\text{Tropics}-\text{SST}}$ and EC-$2_{\text{Tropics}-\text{SST}}$ indices with the EC-1_{SST} index in the models (Table 4.4). Column 2 of Table 4.4 shows the correlation between the EC-$1_{\text{Tropics}-\text{SST}}$ and EC-1_{SST} indices. In observations, the two indices are significantly correlated ($r = 0.56; p < 0.05$). Only one model (the CSIRO3.5 model) has a correlation nearly that high ($r = 0.60$). Of the remaining models, only seven models have significant ($p < 0.05$) correlations between their EC-$1_{\text{Tropics}-\text{SST}}$ and EC-1_{SST} indices. By contrast, five models (the BCCR-BCM2.0, the CGCM3.1 (T63), and the three GISS models) display almost zero correlation between the two indices. The mean correlation in the models between EC-$1_{\text{Tropics}-\text{SST}}$ and EC-1_{SST} is 0.25, which is well below that in observations. By contrast, when evaluating the correlations between the EC-$2_{\text{Tropics}-\text{SST}}$ and EC-1_{SST} indices we find that in observations the correlation is small and insignificant ($r = 0.17$). However, nine of the 24 models show significant correlations between their EC-$2_{\text{Tropics}-\text{SST}}$ and EC-1_{SST} indices, with significant correlations ranging from $r = 0.21$ for the CSIRO3.5 model to $r = 0.69$ for the UK-HADCM3 model. The ensemble-mean correlation for the models is 0.28, which is close to the ensemble-mean correlation between the EC-$1_{\text{Tropics}-\text{SST}}$ and EC-1_{SST} indices.

4.6 Chapter Summary and Discussion

Characterizing NPDV in coupled climate models and their predictability skill for short-term and long-term climate are critical research questions in climate dynamics today. Accurately representing in the models the two leading patterns of oceanic and atmospheric variability in the region is integral to answering these questions, as these modes have profound effects on sensible weather downstream through teleconnections and on biological and ocean properties important to coastal ecosystems in the North Pacific. Moreover, both modes are important at decadal-time scales,

Table 4.4. Correlations between tropical and North Pacific SST indices for the IPCC models and observations. Correlations exceeding the 95% significance level are in bold.

Model Name / Data	$r(EC\text{-}1_{\mathbf{Tropics-SST}}, EC\text{-}1_{\mathbf{SST}})$	$r(EC\text{-}2_{\mathbf{Tropics-SST}}, EC\text{-}1_{\mathbf{SST}})$
BCCR-BCM2.0	0.07	**0.43**
CGCM3.1 (T47)	0.26	0.15
CGCM3.1 (T63)	0.04	0.12
CNRM-CM3	0.15	**0.66**
CSIRO3.0	0.25	**0.32**
CSIRO3.5	**0.60**	**0.21**
GFDL2.0	0.20	0.13
GFDL2.1	0.29	0.11
GISS-AOM	0.03	0.13
GISS-EH	0.04	0.12
GISS-ER	0.09	0.25
IAP-FGOALS1.0	**0.36**	**0.61**
INGV-ECHAM4	0.17	**0.45**
INMCM3.0	0.22	0.06
IPSL-CM4	**0.35**	0.18
MIROC-HIRES	**0.44**	**0.34**
MIROC-MEDRES	**0.41**	0.16
MIUB-ECHO-G	0.22	0.27
MPI-ECHAM5	0.30	0.18
MRI-CGCM2.3.2	**0.38**	**0.57**
NCAR-CCSM3.0	0.11	0.21
NCAR-PCM1	**0.30**	0.20
UK-HADCM3	**0.37**	**0.69**
UK-HADGEM1	0.29	0.14
Ensemble-Mean	0.25	0.28
Observations	**0.56**	0.17

meaning their representation in the models is important for future climate change studies. Previous studies have looked at characterizing changes in the North Pacific or in the ENSO phenomenon in climate models in isolation from each other. This study complements those studies and goes further by exploring both North Pacific and tropical Pacific climate variability of the IPCC AR4 models when evaluating NPDV. Moreover, we include every realization from each model, in the 20C3M and SRESA1B scenarios, providing a comprehensive examination of NPDV in the coupled

climate models.

When testing North Pacific-only variables, the models reliably reproduce the two leading oceanic patterns of variability with high spatial similarity to their observational counterparts (Figs. 4.1 and 4.2). Yet, the frequency of those patterns do not agree among the models. For the first SSTa mode (EC-1_{SST}), every model shows the strongest power at the decadal and time scales (Fig. 4.3a), but the total variance in the model indices is less than observed (Table 4.2, Column 2). For the EC-2_{SST} index, however, all models have their strongest power in the 10-20 year band, while the observations have a dual peak signature with local maxima at about 5 and 10 years. Another general issue with the models is that their EC-2_{SST} indices exhibit much more variance than observed (Table 4.2, Column 3). This higher-than-observed variance, along with different spectral characteristics of the index, lowers confidence in the predictability of NPDV and even global climate change based on these models.

For implications on future climate change, the models show no consensus on projected future changes in the frequency of either the first or second leading pattern of North Pacific SSTa. Neither the difference in power spectra (not shown) nor changes in variances of the indices (Table 4.2) displays consistent changes between the 20^{th} and 21^{st} centuries in the models. The lack of a consensus in changes in either mode also affects confidence in projected changes in the overlying atmospheric circulation. Work by Bengtsson et al. (2006), Teng et al. (2008), and Ulbrich et al. (2008) suggest that global climate change will influence changes in storm tracks and hence could influence the strength and location of planetary waves and associated climatological features like the AL. Since the wind stress curl induced by the AL and NPO are drivers to the leading modes of North Pacific SSTa, we would expect that changes in their characteristics would change the dominant SSTa patterns. There appears to be a disconnect in this aspect of the models that needs to be addressed.

The results of an AR-1 model test also present more differences between the

models and observations in the temporal evolutions of the leading two North Pacific SSTa cEOF patterns. The cEC-1_{SST} index can be reconstructed by forcing the AR-1 model with the atmospheric variability of the AL in both observations and models (Fig. 4.7), though the correlations between the original and reconstructed indices in the models are much higher than in observations. The cEC-1_{SST} index also appears to have a shorter "memory" in the models than observation (Table 4.3 and Fig.4.9). For the cEC-2_{SST} index (Fig. 4.8), NPO variability contributes significantly to the index in observations, but the integration of the NPO forcing is more challenging for the models (Fig. 4.8b). For some models, the NPO does not drive the oceanic expression of cEC-2_{SST}. We also find that the memory associated with the second mode (e.g. the τ values for the cEC-2_{SST} index reconstruction) is longer in the models than in observations (Table 4.3), suggesting that the second mode in the models may be tracking an internal ocean mode that is not directly forced by the atmosphere. Indeed, some models that exhibit poor skill in reconstructing the cEC-2_{SST} index (Fig. 4.8) also perform poorly in reproducing the NPO pattern spatially (cEOF-2_{SLP}; Fig. 4.2).

Finally, the coupled climate models display very weak or nonexistent links between North Pacific climate variability and the first two dominant modes of tropical Pacific SSTa variability (i.e., the ENSO and CPW phenomena). The ensemble-mean SSTa and SLPa projections of the two leading modes of tropical Pacific SSTa variability display little to no correlation over the North Pacific, with the mid-latitude atmospheric teleconnection having significant differences in amplitude and structure than observed (Figs. 4.11a and 4.11b). In the models, the first and/or second leading mode of tropical Pacific SSTa project onto the AL/PDO unlike observations where only the canonical ENSO mode projects onto a AL/PDO mode in the North Pacific. In fact, in the ensemble-mean, the second mode of tropical Pacific SSTa variability projects onto the SSTa pattern in cEOF-1_{SST}. This inconsistency in the teleconnection may

be directly related to the very different structure of the AL between the North Pacific analysis (Fig. 4.6a) and the tropical Pacific regression analysis (Fig. 4.11a). Reasons for this different AL representation remain unclear and may be related to mechanisms associated with the atmospheric bridge (Alexander et al., 2002), including the distribution of tropical convection in the models, which influences the generation of atmospheric waves that impacts extratropical North Pacific storm tracks.

The relationship between North Pacific variability and EOF-$2_{\mathrm{Tropics-SST}}$ is also not represented well in the coupled models (Figs. 4.11c and 4.11d). The North Pacific SLPa pattern associated with EOF-$2_{\mathrm{Tropics-SST}}$, in particular, lacks an NPO-like dipole (Fig. 4.11c). The SSTa regression pattern indicates a "Warm Pool Warming" (Fig. 4.11d), which is a common issue in select coupled climate models (e.g., Kug et al. 2010). Recent work by Yeh et al. (2009) notes that several of the climate models used in this study forecast significant increases in the frequency of the CPW-type El Niño episodes in the SRESA1B scenario. Because of the growing importance of this flavor of ENSO variability, more work is needed on understanding why coupled climate models, in general, cannot capture its statistics and dynamics.

The results presented in this chapter do not offer definitive evidence of what changes are expected in North Pacific climate variability. The lack of consensus mirrors parallel findings in changes in ENSO behavior conducted by van Oldenborgh et al. (2005), Guilyardi (2006), and Merryfield (2006), for example. Even though certain models may appear to perform better than others among the various analyses, the best approach to rectifying future climate change issues likely resides with using multi-member ensembles (Reifen and Toumi, 2009) for enhancement of the model performance and for predictions.

CHAPTER V

RECONSTRUCTIONS OF TROPICAL SEA SURFACE TEMPERATURES FROM PALEO-PRECIPITATION PROXIES

The work presented in this chapter is published in Journal of Climate (Furtado et al., 2009).

Our analysis of tropically-forced NPDV in Chapter 3 illustrated that the CPW, is strongly linked to the second-leading modes of North Pacific SLPa and SSTa. Thus, its representation in climate model output directly affects the fidelity of climate model projections of future climate for the North Pacific and also global climate change via teleconnection patterns associated with the CPW mode. Yet, the coupled climate models poorly capture the CPW-NPO-NPGO connections (Chapter 4). One method used to improve climate model projections of future climate change is examining at past climates through paleoclimate reconstructions. This chapter connects the importance of the CPW mode to paleoclimate reconstruction efforts of tropical Pacific SSTs from paleo-precipitation records. In particular, we contrast two popular paleoclimate reconstruction methods and show that the method which implicitly includes the CPW mode in its reconstruction algorithm has far superior skill, thus emphasizing the importance of checking for this mode along with the canonical ENSO signature in paleoclimate studies of tropical Pacific and North Pacific decadal climate variability.

5.1 Background

Paleoclimate reconstructions of tropical SST fields are used to characterize the range of tropical climate variability and may improve our understanding of the role that the tropics play in global climate change. These reconstructions use a variety of proxy records ranging from tree rings and ice cores to corals and marine sediments in both the tropics and extratropics (e.g., Stahle et al. 1998; Evans et al. 2002). Although some of these proxies measure changes in tropical SSTs more directly by exploiting the relationship between temperature and a geochemical proxy (e.g., δ^{18}O in corals), most tropical proxies capture changes in precipitation (e.g., lake sediments, tree rings, speleothems, and ice cores from tropical glaciers), which are only indirectly related to SSTs. In the tropics, changes in precipitation are dynamically linked to SSTs through the ENSO phenomenon (e.g., Bjerknes 1966; Wyrtki 1975; Rasmusson and Carpenter 1982), which represents the leading mode of variability for both precipitation and SST (e.g., Dai and Wigley 2000). This linkage is evident from principal component analysis (PCA; e.g., Obukhov 1947; Lorenz 1956; Kutzbach 1967) of observations and modeled data, which show that the first PC (PC-1) time series of precipitation is strongly correlated with the NINO3.4 index ($r > 0.9$ for all precipitation datasets), another measure of ENSO activity (Figure 5.1, left). The spatial expression of the leading mode of precipitation (Fig. 5.1, right) exhibits strong loadings in the central tropical Pacific and Warm Pool regions and is reminiscent of the horseshoe pattern in SST associated with ENSO (e.g., Wallace et al. 1998).

The strong resemblance between the leading precipitation and SST modes suggests that precipitation proxy records located in major loading regions will have high skill in reconstructing past ENSO conditions. This assumption is the basis for using single paleo-precipitation reconstructions to reconstruct tropical SST variations. Single proxy reconstruction methods use an individual record from corals (e.g., Cole and Fairbanks 1990; Urban et al. 2000; Tudhope et al. 2001), marine sediments (e.g.,

Rein et al. 2004), tree rings (e.g., Michaelson 1989; D'Arrigo et al. 2005), lake sediments (e.g., Rodbell et al. 1999; Moy et al. 2002), ice cores (e.g., Thompson et al. 1985; Bradley et al. 2003) and speleothems (e.g., Rasbury and Aharon 2006; Partin et al. 2007) to reconstruct tropical Pacific SST variability. First, the proxy record is calibrated with SSTs or the NINO3.4 index over a period when both proxy and instrumental data are available. If this calibration yields a significant correlation between the proxy and SST, the proxy record is then used as a surrogate of past ENSO activity and hence tropical Pacific SSTa. Despite the apparent strength of this method, large uncertainties in these types of reconstructions exist because of the inability of the proxy to record a specific climate parameter perfectly (microenvironmental effects, for example), and because a local climate signal may poorly represent large-scale climate processes.

Multi-proxy reconstructions reduce the uncertainties associated with single proxy reconstructions by using numerous proxies of various types (e.g., corals, tree rings, and sediments) from different locations, under the assumption that their shared signals represent large-scale climate patterns. Typically, such reconstructions create a climate pattern template by calibrating each proxy record against the instrumental record and use these templates to extrapolate back in time. Examples of methods that use these climate pattern templates are (a) PCA (e.g., Mann et al. 1998) and (b) reduced space objective analysis (e.g., Evans et al. 2002). Both methods reside in the climate field reconstruction (CFR) family (Mann et al., 2005), a group of methods favored for studying low frequency climate variability. Although the multi-proxy approach is useful in reducing and quantifying the uncertainties of reconstruction of SST fields based on single proxies, there are several sources of error that require careful consideration. One issue is that some proxies are better able to capture tropical SST variations over others. Secondly, different proxies may measure different climate

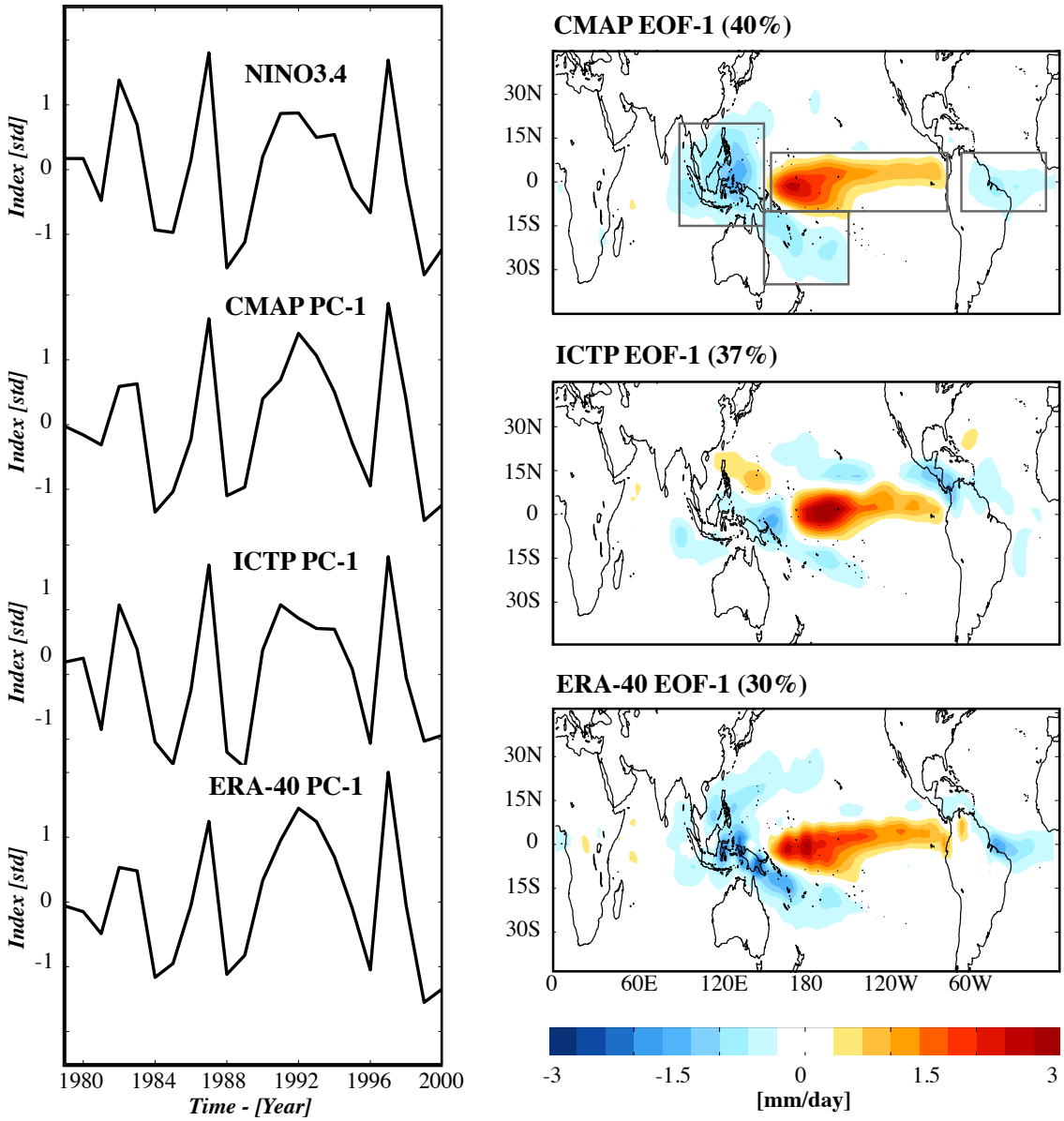

FIG. 5.1. (left) Annually-averaged NINO3.4 index from 1979 - 2000 (top) and the PC-1 time series of annual-mean global precipitation anomalies from 1979 - 2000 for the three precipitation datasets (CMAP, ICTP model output, and ERA-40). (right) Regression of global annual-mean precipitation anomalies (mm/day) onto the PC-1 time series of global precipitation anomalies for the three precipitation datasets. Percent variance explained by the leading mode of precipitation variability included in the title of each plot. Gray boxes in CMAP EOF-1 are described in the text.

variables (e.g. precipitation versus temperature), making extracting a common climate signal from the multiple proxies difficult. Finally, the inherent assumption of stationarity of the climate statistics that underlies CFR methods may not always be valid (i.e., climate patterns and teleconnections may change with time) and hence the reconstructive skill may be substantially reduced. One example of non-stationary statistics in the tropics is evident in the evolution of ENSO events following the 1976-77 climate shift (e.g., Neelin 1991; Neelin et al. 1994; Trenberth and Hurrell 1994; Zhang et al. 1997; Federov and Philander 2000, 2001; Guilyardi 2006). To what extent this change in ENSO behavior impacts the overall skill of a tropical SST reconstruction has not been explicitly addressed.

The goal of this study is to quantify the uncertainties in SST reconstructions obtained using multi-proxy records of precipitation by applying both EOF-based and multi-regression techniques to pseudoproxy data over the period 1979 - 2000. The EOF method yields significant skill only in the eastern tropical Pacific, where it captures most of the ENSO events, although some events have the wrong sign. Alternatively, the multi-regression approach has higher skill that extends throughout the tropical Pacific and Indian Oceans and correctly predicts all ENSO events. A key factor in this superior skill is the inclusion of the CPW-type variability in the multiregression model. We also show that the skill of the multi-regression method is degraded when applied to the 1950 - 2000 interval due to nonstationarity in the tropical SST-precipitation relationship.

Section 5.2 describes the data and analysis tools used. Section 5.3 assesses the sensitivity of the SST reconstructions to the method and the precipitation dataset used to build the climate pattern template. Section 5.4 addresses the issue of nonstationarity in ENSO statistics over the last 50 years and its impact on the reconstructive skill. Section 5.5 explores the performance of a realistic paleo-precipitation proxy network, including how the errors in paleo-precipitation records propagate into the

resulting SST reconstructions. A summary of the results of this chapter is provided in Section 5.6.

5.2 Methodology

5.2.1 Precipitation and SST Datasets

Precipitation data used in this study originate from three sources: CMAP, ERA-40, and the ICTP model (i.e., the AGCM is forced by prescribed SSTa from the NOAA ER SSTs globally from 1950 - 2000). To evaluate the reconstruction methods, we restrict the observational data to only 1979 - 2000, the common period for all datasets. All fields are annually averaged (January - December) and detrended. Annual-mean anomalies are derived by removing the 1979 - 2000 mean from the annual means of each year. When evaluating the effect of nonstationary climate statistics on the skill of the reconstructions, the climate pattern template is constructed using detrended annual-mean precipitation anomalies for each year from the full 51-yr model run along with the corresponding detrended annual-mean SSTa from the NOAA ER SSTs. SST and precipitation data are spatially smoothed using a 5-point averaging scheme - the value assigned to each grid point is the average of the values in that grid point and the four adjacent grid points to the north, south, east, and west. This smoothing technique reduces the effects of mesoscale features in the two fields while still retaining the large-scale features that are of interest in this study. SST anomaly reconstructions are performed only from 30°S to 30°N (referred to as *the tropics* in this chapter) and are compared to the NOAA ER SSTs to assess errors in the reconstructions.

5.2.2 Precipitation Proxy Network

One objective of our study is to assess how well a given proxy network of paleo-precipitation data can reconstruct tropical Indo-Pacific SSTa. Figure 5.2a illustrates

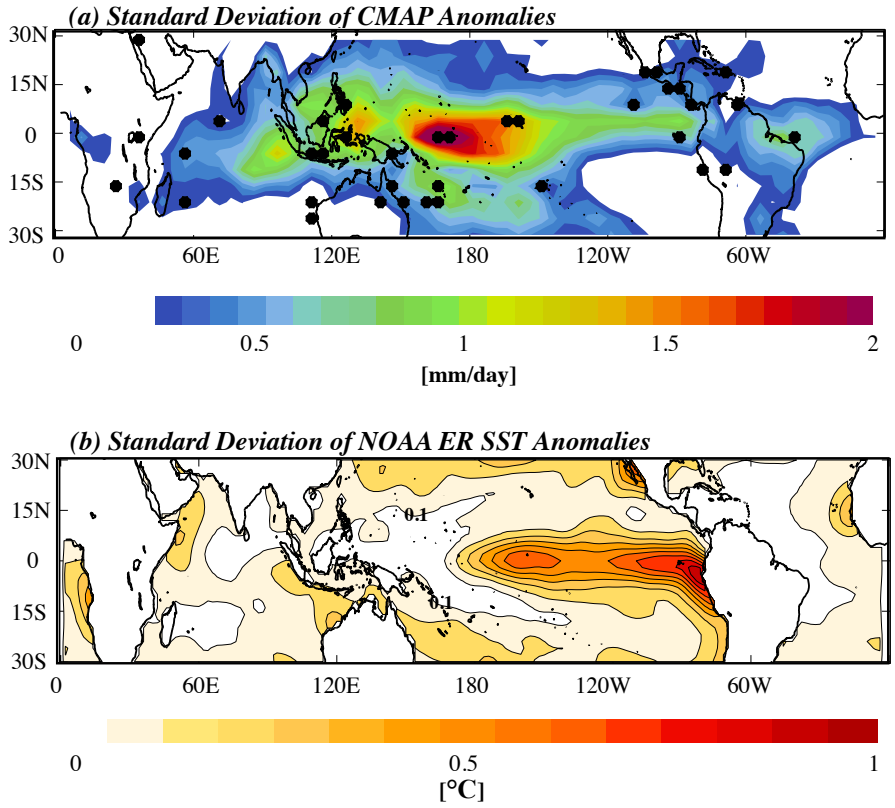

FIG. 5.2. (a) Standard deviation of annual-mean precipitation anomalies from CMAP (mm/day; shaded color contours) from 1979 - 2000 superimposed on the proxy network locations from Table 5.1 (black dots). Values smaller than 0.2 mm/day are not shaded. (b) Standard deviation of annual-mean SSTa (°C) from 1979 - 2000. Contour interval every 0.1°C. The 0.1°C contour is labeled for reference.

the paleo-precipitation proxy network employed in this study (black dots), with the names and types of proxies listed in Table 5.1. The proxy network consists of both terrestrial and oceanic proxies scattered throughout the tropics. Several of the proxies lie in areas of high precipitation variance (shaded contours in Fig. 5.2a; e.g., those in the tropical Pacific Ocean) while others do not (e.g., those in the far western Indian Ocean, Africa, and off of the Australian coast). We create a pseudoproxy network based on our realistic proxy network by replacing each proxy record with CMAP data from that proxy's location. Because multiple sites reside within the same grid box, only 39 of the 45 locales represent unique grid points for the reconstruction.

Table 5.1. Precipitation proxy network used for the tropical SST reconstructions. Dates are given in years A.D. or in years before present (YBP).

Type of Proxy	*Location (Lat, Lon)*	*Time Period*	*Reference*
Corals	Aqaba 18 (29.5°N, 35°E)	1788 – 1992	Heiss (1994)
	Cebu (10°N, 124°E)	1859 - 1979	Pätzold (1984)
	Secas Island (7.6°N, 82.3°W)	1708 - 1984	Linsley et al. (1994)
	Kiritimati (2.0°N, 157.3°W)	1938 - 1993	Evans et al. (1999)
	Tarawa Atoll (1.0°N, 172.0°E)	1894 - 1989	Cole and Fairbanks (1990)
	Urvina Bay (0.4°S, 91.2°W)	1607 - 1953	Dunbar et al. (1994)
	Punta Pitt (0.7°S, 89.1°W)	1936 - 1983	Shen et al. (1992)
	Mahe, Seychelles (4.6°S, 55.8°E)	1846 - 1995	Charles et al. (1997)
	Espiritu Santo (15°S, 167°E)	1806 - 1979	Quinn et al. (1996)
	New Caledonia (20.7°S, 166.2°E)	1657 - 1992	Quinn et al. (1998)
	Abraham Reef (22.1°S, 153.0°E)	1635 - 1957	Driffel and Griffin (1993)
	Amedee Lighthouse (22.3°S, 166.3°E)	1657 - 1992	Quinn et al. (1998)
	Bunaken (1.3°N, 124.5°E)	1860 - 1990	Charles et al. (2003)
	Brook Island (18.1°S, 146.2°E)	1565 - 1985	Hendy et al. (2002)
	Clipperton Atoll (10.3°N, 109.2°W)	1893 - 1994	Linsley et al. (2000a)
	Houtman Abrolhos Islands (28.3°S, 113.5°E)	1795 - 1994	Kuhnert et al. (1999)

Table 5.1 – Continued

Type of Proxy	*Location (Lat, Lon)*	*Time Period*	*Reference*
	Ifaty Reef (23.9°S, 43.3°E)	1659 - 1995	Zinke et al. (2004)
	La Parguera (17.6°N, 64.0°W)	1700 - 1989	Winter et al. (2000)
	Laing Island (4.1°S, 144.5°E)	1884 - 1993	Tudhope et al. (2001)
	Lombok Strait (8.2°S, 115.3°E)	1782 - 1990	Charles et al. (2003)
	Madang (5.2°S, 145.9°E)	1880 - 1993	Tudhope et al. (2001)
	Maiana (1.0°N, 173.0°E)	1840 - 1995	Urban et al. (2000)
	Malindi (3.0°S, 40.0°E)	1801 - 1994	Cole et al. (2000)
	Moorea Lagoon (17.3°S, 149.5°W)	1852 - 1990	Boiseau et al. (1999)
	Nauru (0.5°S, 167.0°E)	1897 - 1995	Guilderson and Schrag (1999)
	Ningaloo Reef (21.5°S, 113.6°E)	1878 - 1994	Kuhnert et al. (2000)
	Palmyra Island (5.5°N, 162.8°W)	1886 - 1998	Cobb et al. (2001)
	Rarotonga Island (21.1°S, 159.5°W)	1726 - 1997	Linsley et al. (2000b)
	Saint Gilles (21°S, 55°E)	1830 - 1995	Pfeiffer et al. (2004)
Marine Sediments	Cariaco Basin (10°N, 65°W)	19000 YBP - Present	Haug et al. (2001)
	Peru Lithics (12.0°S, 77.4°W)	∼12000 YBP - Present	Rein et al. (2004)

Table 5.1 – Continued

Type of Proxy	*Location (Lat, Lon)*	*Time Period*	*Reference*
	Mindanao Strait (7°N, 127°E)	∼15000 YBP - Present	Stott et al. (2004)
Tree Rings	El Vado (16.4°N, 96.5°W)	1750 - 1990	Therrell et al. (2002)
	Mzola Forest (18.2°S, 27.4°E)	1796 - 1997	Stahle et al. (1999)
	Nevado de Colima (19.4°N, 103.4°W)	1553 - 1997	Biondi (2001)
	Villareal (19.3°N, 97.5°W)	1710 - 1998	Therrell et al. (2002)
	Baobab Holes (18.4°S, 26.4°E)	1846 - 1994	Stahle, Gabor, Haynes, Klimowicz, and Ngwenya[6]
	Bigin (7.2°S, 111.5°E)	1839 - 1995	D'Arrigo et al. (1994)
	Sikumi (18.3°S, 26.6°E)	1870 - 1996	Stahle et al. (1999)
Lake Sediments	Lake Peten-Itza (16.6°N, 89.5°W)	9000 YBP - Present	Curtis et al. (1998)
	Lake Valencia (10°N, 66°W)	20000 YBP Present	Street-Perrott et al. (1989)
Speleothem	Borneo (4°N, 115°E)	2000 YBP - Present	Partin et al. (2007)
Ice Cores	Kilimanjaro (3°N, 37°E)	1800 - 2000	Thompson et al. (2002)
	Huascaràn (9°S, 77°W)	19000 YBP - Present	Thompson et al. (1995)
	Quelccaya (13.5°S, 70.5°W)	470 - 1980	Thompson et al. (1985)

[6]No published article cited. Data archived at the World Data Center for Paleoclimatology, Boulder, Colorado, USA.

5.2.3 Reconstruction Methods

5.2.3.1 EOF Method

The EOF method exploits the close relationship between SSTs and precipitation in the tropics, dominated by coupled ENSO dynamics, to reconstruct SSTs from precipitation. Here, we only use the first EOF (EOF-1) of precipitation and SSTs because the PC-1 time series of global precipitation variability explains nearly 80% of the variability in global SST variability (see Fig. 5.1). Letting $\mathbf{V}_{SST}$ and $\mathbf{U}_{SST}$ represent EOF-1 of global SSTs and its associated PC time series, respectively, SSTa ($\mathbf{y}_{SST}$; i.e., the unknown) can be approximated as

$$\mathbf{y}_{SST} \approx \mathbf{V}_{SST}\mathbf{U}_{SST}. \tag{5.1}$$

Similarly, for precipitation anomalies ($\mathbf{x}_p$),

$$\mathbf{x}_p \approx \mathbf{V}_p\mathbf{U}_p, \tag{5.2}$$

where $\mathbf{V}_p$ is EOF-1 of global precipitation anomalies, and $\mathbf{U}_p$ is the corresponding PC time series. Both $\mathbf{V}_{SST}$ and $\mathbf{V}_p$ are assumed to be time-invariant implying that SST and precipitation have stationary statistics. Given $\mathbf{x}_p$ and $\mathbf{V}_p$, we can estimate the PC time series using a least-square approach:

$$\hat{\mathbf{U}}_p = \left(\mathbf{V}^{\mathbf{T}}{}_p\mathbf{V}_p\right)^{-1}\mathbf{V}^{\mathbf{T}}{}_p\mathbf{x}_p, \tag{5.3}$$

where the caret denotes an estimate.

As noted before, $\mathbf{U}_p$ and $\mathbf{U}_{SST}$ are significantly correlated, so that $\mathbf{U}_{SST} = \alpha\hat{\mathbf{U}}_p$, where the correction factor (α) is chosen as the regression coefficient between the PC-1 time series of SST and the PC-1 time series of the precipitation data from 1979-2000. Replacing $\mathbf{y}_{SST}$ with $\hat{\mathbf{y}}_{SST}$ and setting $\mathbf{U}_{SST} = \alpha\hat{\mathbf{U}}_p$, (5.1) becomes

$$\hat{\mathbf{y}}_{SST} = \alpha\mathbf{V}_{SST}\hat{\mathbf{U}}_p, \tag{5.4}$$

which allows us to reconstruct tropical SSTa using the known leading modes of variability of global SST and precipitation anomalies. Note that this method only works for the PC-1 time series of SST because of its high correlation with the PC-1 time series of precipitation. Higher modes of precipitation and SST are not correlated, and thus this method would not be adequate unless one computes explicitly the leading modes of covariability between SST and precipitation. This is the basis for the multi-regression approach illustrated below.

5.2.3.2 Multi-Regression Method

The other reconstruction method used in this study is based on multi-regression or covariance modeling, a technique that uses least-squares fitting to estimate one variable from another (e.g., Wunsch 2006). This approach can be viewed as an extension of the EOF method in that it accounts for more modes of covariability between SSTs and precipitation, rather than the variability of each climate variable separately.

Considering two variables, the predictand $\mathbf{y}$ (SSTs) and the predictor $\mathbf{x}$ (precipitation), the linear relationship between these two variables can be written as

$$\mathbf{y} = \mathbf{E}\mathbf{x} + \mathbf{n}, \tag{5.5}$$

where $\mathbf{E}$ is a mapping matrix from $\mathbf{x}$ onto $\mathbf{y}$, and $\mathbf{n}$ is the error associated with linearization. If no known analytical relationship exists between $\mathbf{x}$ and $\mathbf{y}$, a statistical relationship can be used for $\mathbf{E}$. If $\mathbf{n}$ is assumed to be Gaussian, then the optimal statistical choice for $\mathbf{E}$ is one that minimizes the mean square error (MSE; i.e., $\langle \mathbf{n}\mathbf{n}^{\mathbf{T}} \rangle$, where $\langle\ \rangle$ denotes the averaging operator). From (5.5),

$$\langle \mathbf{n}\mathbf{n}^{\mathbf{T}} \rangle = \langle (\mathbf{y} - \mathbf{E}\mathbf{x})\,(\mathbf{y} - \mathbf{E}\mathbf{x})^{\,\mathbf{T}} \rangle = \langle \mathbf{y}\mathbf{y}^{\mathbf{T}} \rangle + \mathbf{E}\langle \mathbf{x}\mathbf{x}^{\mathbf{T}} \rangle \mathbf{E}^{\mathbf{T}} - 2\langle \mathbf{y}\mathbf{x}^{\mathbf{T}} \rangle \mathbf{E}^{\mathbf{T}}. \tag{5.6}$$

By minimizing $\langle \mathbf{n}\mathbf{n}^{\mathbf{T}} \rangle$, the optimal linear estimator is found to be

$$\mathbf{E} = \langle \mathbf{y}\mathbf{x}^{\mathbf{T}} \rangle \langle \mathbf{x}\mathbf{x}^{\mathbf{T}} \rangle^{-1} = \mathbf{C}_{yx}\mathbf{C}_{xx}^{-1}, \tag{5.7}$$

where $\mathbf{C}_{ij}$ is the covariance matrix between i and j. Hence,

$$\hat{\mathbf{y}} = \mathbf{C}_{yx}\mathbf{C}_{xx}^{-1}\mathbf{x}, \tag{5.8}$$

is the best estimate for tropical SSTs using precipitation data provided in $\mathbf{x}$. The MSE associated with using (5.7) is then

$$\langle \mathbf{n}\mathbf{n}^{\mathbf{T}} \rangle = \mathbf{C}_{yy}\left[1 - \mathbf{C}_{yy}^{-1}\mathbf{C}_{yx}\mathbf{C}_{xx}^{-1}\mathbf{C}_{yx}^{\mathbf{T}}\right], \tag{5.9}$$

which serves as an estimate of the error in our reconstructed SSTa.

Inverting covariance matrices with data from very large or high-resolution grids is computationally expensive. So, we degrade the spatial resolution of the precipitation and SST datasets to every other grid point within the tropics prior to covariance analysis. Before computing $\mathbf{E}$, the covariance matrices are calculated and decomposed into eigenvalues and eigenvectors. For $\mathbf{C}_{xx}$ and $\mathbf{C}_{yy}$ ($\mathbf{C}_{yx}$), we retain only those modes that explain more than 1% (5%) of the total covariance. This additional step is performed to eliminate statistically insignificant higher-order modes of covariability. The resulting reconstructions have fewer degrees of freedom and retain larger scale features. We also use a simple cross-validation scheme to test for robustness of the covariance statistics that enters $\mathbf{E}$. This is done by calculating $\mathbf{E}$ using a subset of the data from 11 of the 22 available years and assessing the reconstructive skill over the entire period of the data. The process is repeated 20 times with different 11-year sets of data. We then take the average error of the 20 reconstructions and verify that it is equivalent to the one estimated by (5.9).

5.2.4 Assessing Errors in the SST Reconstructions

Errors in the SST reconstructions are assessed in three ways:

- *The root-mean-square (RMS) error*:

$$\mathrm{RMS} = \sqrt{\mathrm{var}\,(\hat{y} - y)}, \tag{5.10}$$

where var ( ) is the variance function normalized by $1/(N-1)$ (N is the number of samples), $\hat{y}$ is the time series of reconstructed SSTs at a given point, and y is the time series of observed SSTs from NOAA ER SSTs at the same point. This measure allows us to determine spatially where the reconstructions perform the best.

- *The spatial correlation between the reconstructed and the observed SSTa.* This measure allows us to assess the skill of the SST reconstructions for each year. For example, strong ENSO years may reflect higher spatial correlations than non-ENSO years. Statistically significant correlations at the 95% level are found by using a Monte Carlo-like approach whereby spatial correlations are calculated between one year of observed annual-mean SSTa in the tropics from 1950 - 2000 and every other year in the 1950 - 2000 period. A normalized PDF of the correlations is then used to determine the 95% significance level ($r = 0.64$). Only positive correlations are considered in significance testing since negative correlations mean that large-scale reconstructed SST patterns are of opposite sign from the observations and are hence not meaningful for our study.

- *The reconstructive skill*:

$$\text{Skill} = 1 - \frac{\text{RMS}}{\sqrt{\text{var}\,(y)}}. \tag{5.11}$$

The measure determines how well the reconstructed anomalies compare to the observed fluctuation of SSTs. Because the standard deviation of SSTs varies across the tropics, the skill will have strong spatial dependence. Fig. 5.2b illustrates the standard deviation of SSTs over the tropics from 1979 - 2000. The variations in SSTs are strongest in the upwelling zones of the equator and the Pacific coast of South America, where standard deviations approach 1°C off of the Peruvian coast. Lower variance characterizes the West Pacific Warm Pool

and portions of the Indian Ocean. Therefore, based on (5.11), high skill (values near unity) arises in areas where the RMS error is much smaller than the standard deviation of SSTs and vice versa.

For reconstructions using the multi-regression method, the skill can be computed analytically as

$$\text{Estimated Skill} = 1 - \frac{\text{diag}\left(\langle \mathbf{nn^T} \rangle\right)}{\sqrt{\text{var}\,(y)}}, \tag{5.12}$$

where $\text{diag}\left(\langle \mathbf{nn^T} \rangle\right)$ refers to the diagonal elements of (5.9). We also use (5.12) as an estimate for the EOF method, but $\langle \mathbf{nn^T} \rangle$ contains only errors from the first covariability mode. In this way, we are able to evaluate the utility of using only the leading modes of variability in both methods.

5.3 Evaluation of Reconstruction Methods: 1979 - 2000 Statistics

5.3.1 Reconstructing SSTa from Precipitation Data Using EOF-1

To examine the "best case" scenario for the EOF method, area-averaged precipitation from the four large centers of action in EOF-1 of precipitation are used (as delimited in Fig. 5.1, right, gray boxes). Since these regions represent where the highest ENSO-related variance in precipitation exists, SSTa should be closely tied to precipitation in those regions. These regions are: (a) the equatorial Pacific Ocean (10°S to 10°N, 155°E to 80°W); (b) the Maritime Continent (20°S to 20°N, 90°E to 150°E); (c) the southwest Pacific Ocean (35°S to 10°S, 150°E to 150°W); and (d) the Nordeste region in Brazil and the adjacent tropical Atlantic Ocean (10°S to 10°N, 70°W to 10°W). This averaging would be analogous to "stacking" multiple paleo-precipitation records from the same region together.

Figure 5.3 shows the RMS error between the reconstructed SSTa using the EOF method and observations (Fig. 5.3, left column), along with the reconstructive

(Fig. 5.3, middle column) and estimated (Fig. 5.3, right column) skills, as a function of the precipitation dataset used. In all datasets, RMS errors are a maximum in the central tropical Pacific, just east of the major loading center depicted in Fig. 5.1 (right). For the ICTP model and ERA-40, a secondary maximum in RMS error exists along the South American coast. The reconstructive skill for all datasets is highest only in the eastern tropical Pacific, with the atmospheric model performing worst in terms of absolute skill and CMAP the best (Fig. 5.3, middle column). Elsewhere in the Indo-Pacific basin, little if any skill exists.

The estimated skill of the EOF method (Fig. 5.3, right column) is derived by using only the first mode of covariability between SSTs and precipitation, which strongly resembles the individual leading modes of each variable (see Figure 5.6), in the multi-regression method. Though not explicitly representative of the EOF method per se, this plot shows that using only the leading modes of variability of precipitation and SST restricts skill to the eastern and central Pacific. Note that the estimated skill plots predict maximum skill in the central tropical Pacific, while the EOF method has its highest skill in the far eastern tropical Pacific Ocean.

The spatial correlation coefficients between the reconstructed and observed SSTa (Figure 5.5, black curves) have high temporal variability, with occasional negative coefficients; negative values indicate the SST reconstructions for those years capture the wrong sign of large-scale SSTa in the tropics. These erroneous reconstructions occur mainly during neutral or weak ENSO years (i.e., when values of NINO3.4 are small). Half (11) of the 22 years have reconstructions with spatial correlations that exceed the 95% significance level. However, the mean spatial correlation coefficient for any dataset over all 22 years falls well below the 95% significance level.

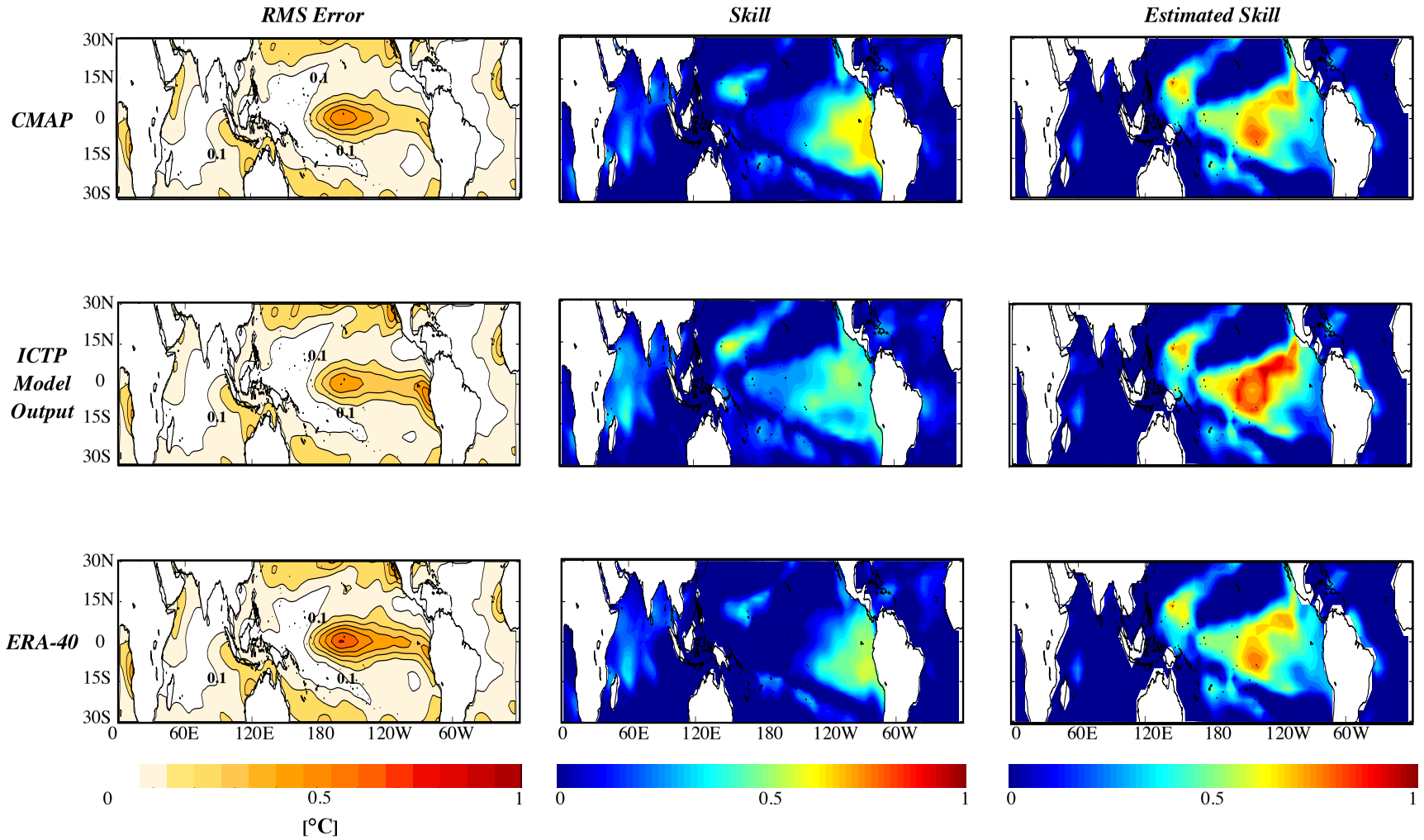

FIG. 5.3. Evaluation of the EOF-based reconstruction method using precipitation from CMAP, ICTP model output, and ERA-40. (left column) RMS error (°C). Contour interval 0.1°C. The 0.1°C contour is labeled for reference. (middle column) Reconstructive skill (dimensionless). (right column) Estimated reconstructive skill (dimensionless), evaluated using only the first covariance mode in the multi-regression model (see text for details).

5.3.2 Reconstructing SSTa from Precipitation Data Using the Multi-Regression Model

The RMS error, mean skill, and estimated skill fields for the multi-regression method are shown in Figure 5.4. RMS errors (Fig. 5.4, left column) are substantially lower than those associated with the EOF method throughout the tropical oceans, with about a 70% reduction in RMS error in the Pacific cold tongue region. The reconstructive skill (Fig. 5.4, middle column) is high over a broad area of the central and eastern tropical Pacific Ocean for all datasets. Moreover, moderate reconstructive skill now exists over the equatorial and northern Indian Ocean regions, compared to little skill with the EOF method. Quantitatively, the improvement in skill of the multi-regression method over the EOF method is roughly 30% in the eastern tropical Pacific Ocean (more so for the atmospheric model), and upwards of 200% in the central tropical Pacific Ocean and the Indian Ocean. Finally, the mean skill levels match those predicted by the estimated skill maps (Fig. 5.4, left column), though the estimated skill fields for both observational sets (CMAP and ERA-40) highly underestimate the demonstrated skill of the multi-regression model in the Indian Ocean.

When examining the spatial correlation between the reconstructed and observed SSTa for the multi-regression method (Figure 5.5, gray curves), we once again see vast improvements over the EOF method. The mean correlations range from 0.73 to 0.75, all of which are statistically significant and higher than their counterparts for the EOF method. Moreover, reconstructions for every year exhibit positive correlation coefficients, demonstrating that the multi-regression model always captures the correct sign of large-scale tropical ocean features (i.e., ENSO events). Minima in the correlation coefficients coincide with neutral or weak ENSO years, as observed with the EOF method, though their variance is less than that observed for the EOF method.

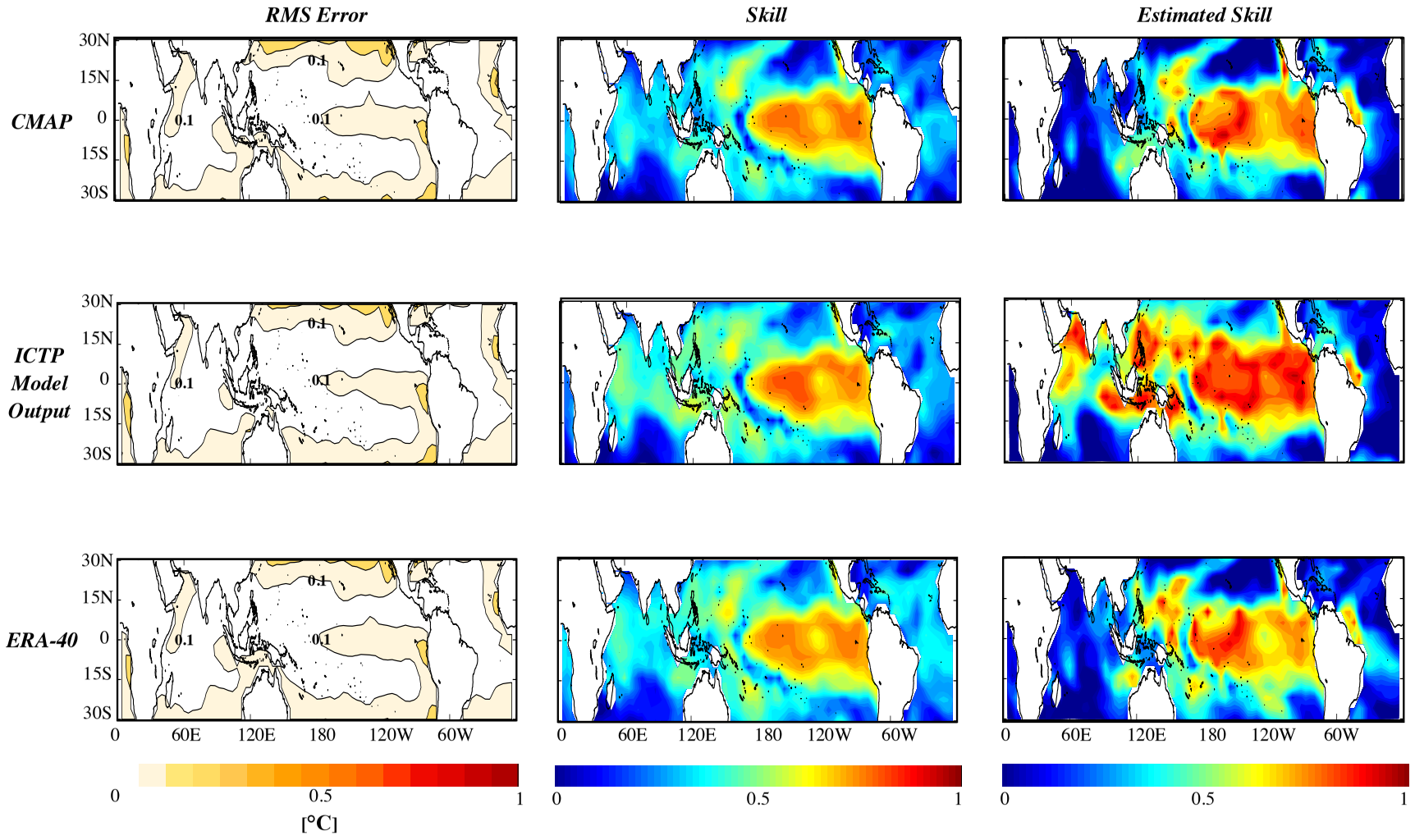

FIG. 5.4. Evaluation of the multi-regression method using precipitation from CMAP, ICTP model output, and ERA-40. (left column) RMS error (°C). Contour interval 0.1°C. The 0.1°C contour is labeled for reference. (middle column) Reconstructive skill (dimensionless). (right column) Estimated reconstructive skill of the multi-regression model (dimensionless).

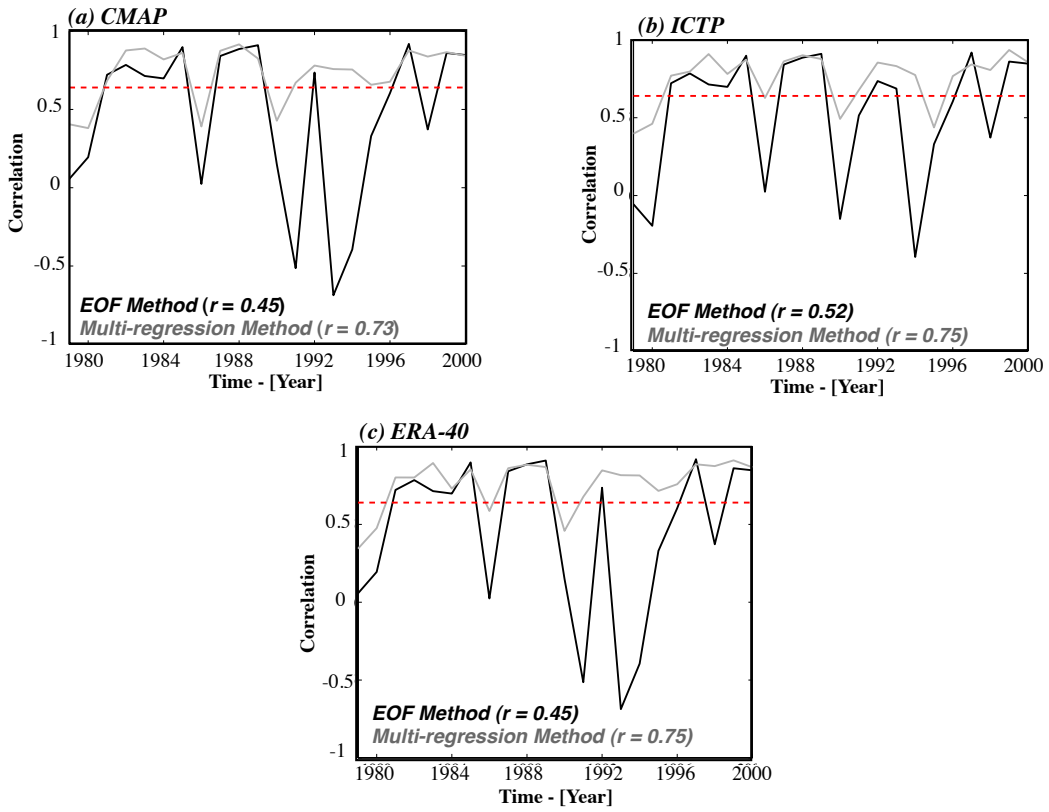

FIG. 5.5. Spatial correlation between the observed and reconstructed tropical SSTa (30°N - 30°S) from the EOF method (black curves) and the multi-regression method (gray curves). Results shown for (a) CMAP, (b) the ICTP run, and (c) ERA-40. Mean correlation for each method also given in each figure. Red dashed line denotes the 95% significance level ($r = 0.64$).

Results for the multi-regression model also hold for several variants on the analysis (figures not shown). One analysis uses boreal summer and boreal winter seasonal mean precipitation and SST fields rather than annual-mean fields. Error measures for this variant were highly similar, particularly for the boreal summer SST reconstructions presumably because of the strong coupling between tropical SSTs and the Northern Hemisphere Intertropical Convergence Zone. Two additional variants of the analysis included using annual-mean anomalies of precipitation and SSTs over the so-called ENSO year (i.e., June - May) instead of calendar year and also comparing our SST anomaly reconstructions with SSTa from the Hadley Centre SST dataset (HadISST; Rayner et al. 2003) instead of the NOAA ER SSTs. For both of these

variations, the results obtained and conclusions drawn were virtually identical those presented in this paper. These sensitivity analyses support the robustness of our results and also the robustness of the observed covariability modes with another SST dataset.

5.3.3 Examination of Modes of Covariability Between Tropical SSTs and Precipitation

As a way of examining why the multi-regression method outperforms the EOF method, we conduct SVD (Bretherton et al., 1992) analysis on the covariance matrix of tropical SST and tropical precipitation anomalies from 1979 - 2000 for each precipitation data source. For this SVD analysis, left singular vectors (LSVs) represent covariability between the two variables in the SST spatial domain, and right singular vectors (RSVs) represent the covariability in the precipitation spatial domain. The presentation of each mode is as follows: (a) We calculate the EC time series for each mode by projecting annual-mean anomaly maps of the variable onto its representative singular vectors (e.g., annual-mean SST anomaly maps are projected onto the leading mode of covariability in the SST domain; LSV-1); (b) The EC time series are then standardized and regressed onto annual-mean anomaly fields of their respective variable. In this way, the spatial patterns of variability have meaningful units of the field itself (i.e., °C for SSTs; mm/day for precipitation). Note that the regressions performed here are homogeneous, but heterogeneous regression (e.g., regressing the EC time series for SSTs onto precipitation anomaly maps) yields virtually the same results.

Figure 5.6 displays the regression of tropical SST and precipitation anomalies onto the first two EC time series from the SVD analysis (labeled Mode 1 and Mode 2 in the figure). For discussion, we will refer to these patterns simply as LSV-1/RSV-1 and LSV-2/RSV-2. The two leading modes of covariability together explain about 95% of the covariance between tropical SST and precipitation anomalies. LSV-1

displays the canonical ENSO signature, while RSV-1 is indistinguishable from EOF-1 of global precipitation anomalies (Fig. 5.1, right). Of more interest, however, is the second mode of covariability, which explains ∼15% of the covariance regardless of the precipitation data used. LSV-2 displays a zonal tripole with alternating positive-negative-positive SSTa across the equatorial Pacific. This SST pattern also coincides a similar zonal tripole in precipitation anomalies as depicted by RSV-2 (Fig. 5.6). Note that even the model captures these patterns, albeit of slightly different spatial scale from the observational datasets. This alternating pattern of SST/precipitation anomalies across the tropical Pacific is very similar to that observed during the 1997-98 ENSO event, for example (e.g., Bell et al. 1999, their Figs. 24 and 26). This correspondence may suggest that the patterns reflect the precipitation response to eastward propagation of SSTa characteristic of the T-mode/delayed oscillator mode of ENSO, prevalent after 1980, as opposed to the westward propagation of SSTs observed during the S-mode of ENSO prior to 1980 (Federov and Philander, 2001, 2003).

More importantly, the SSTa pattern in LSV-2 is also very similar to the regression pattern of the CPW index on tropical Pacific SSTa (see, for example, Fig. 4.10d). For further comparison, Figure 5.7 shows the regression of annual-mean tropical SSTa (Fig. 5.7a) and annual-mean tropical precipitation anomalies from CMAP (Fig.5.7b) onto the annually-averaged CPW index. The SSTa regression pattern mirrors the one from LSV-2 depicted in Fig. 5.6 (top), confirming that the second leading covariability mode in SST space does indeed capture the CPW phenomenon. Moreover, the tripole pattern seen in the precipitation pattern in RSV-2 (Fig. 5.6, bottom) is replicated very well in Fig. 5.7b. The correlation coefficient between the annually-averaged CPW index and the second EC time series in SST space is $r = 0.81\,(p < 0.01)$.

The eigenvalue spectrum in Figure 5.8 further illustrates the importance of including the second mode of covariability in tropical SST reconstructions. Both the

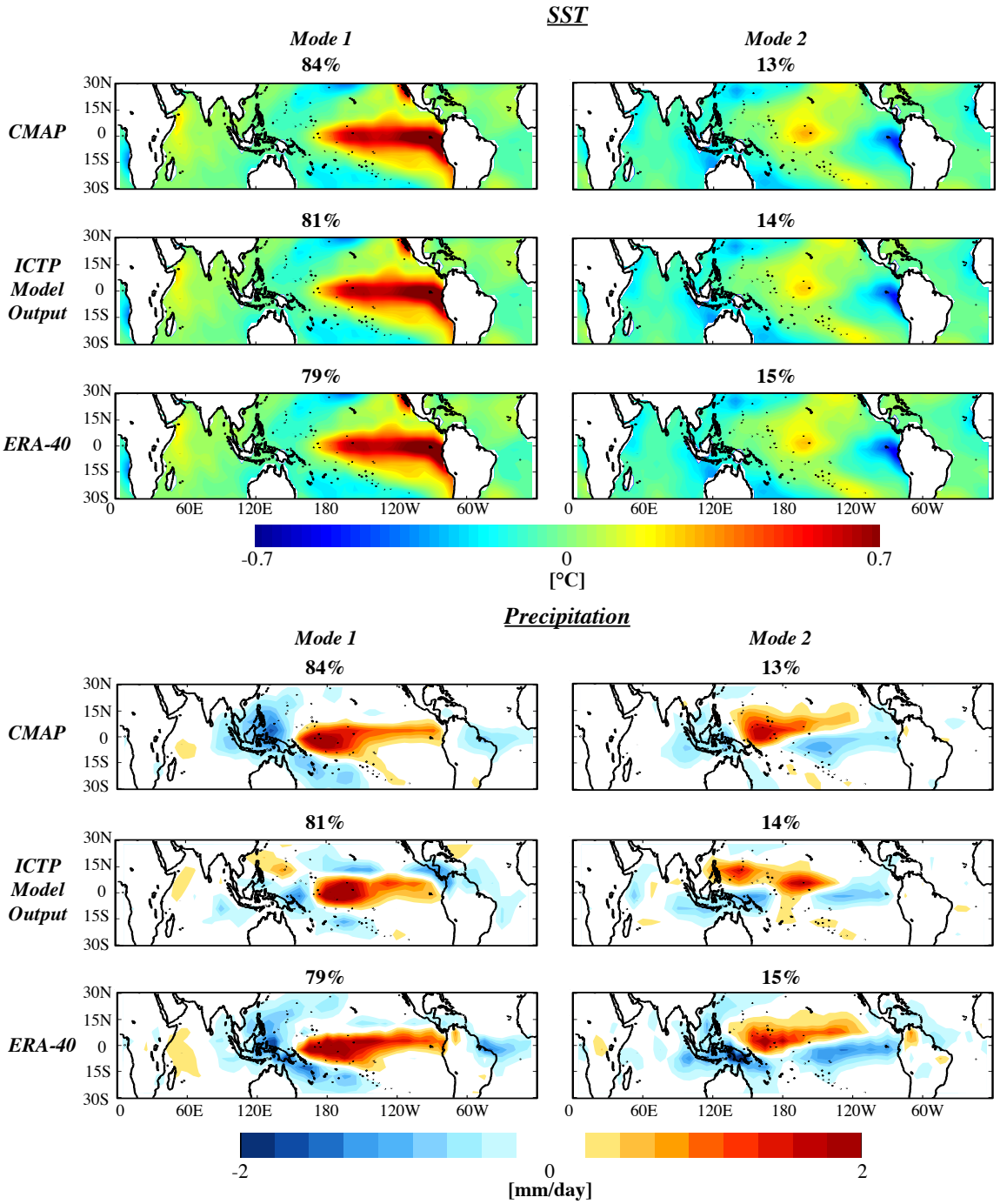

FIG. 5.6. The two leading modes of covariance between tropical SST and precipitation anomalies (30°N - 30°S) from 1979 - 2000 for each dataset. (left) (top) Regression of annual-mean SSTa (°C) onto the first and second EC time series of the LSVs of the SVD analysis. (bottom) Regression of annual-mean precipitation anomalies (mm/day) onto the first and second EC time series of the RSVs of the SVD analysis. Percent covariance explained by each mode is given in the title of each plot

first and second covariability modes are statistically significant per the North et al. (1982) criterion, with modes 3 and higher insignificantly different from each other in terms of percent variance explained.

5.4 Nonstationarity and Its Impact on Reconstructive Skill

The assessments of tropical SST reconstructions presented thus far have been based solely using statistics from the 1979 - 2000 period. This period of time is relatively short and therefore affects the significance of our results through potential bias,

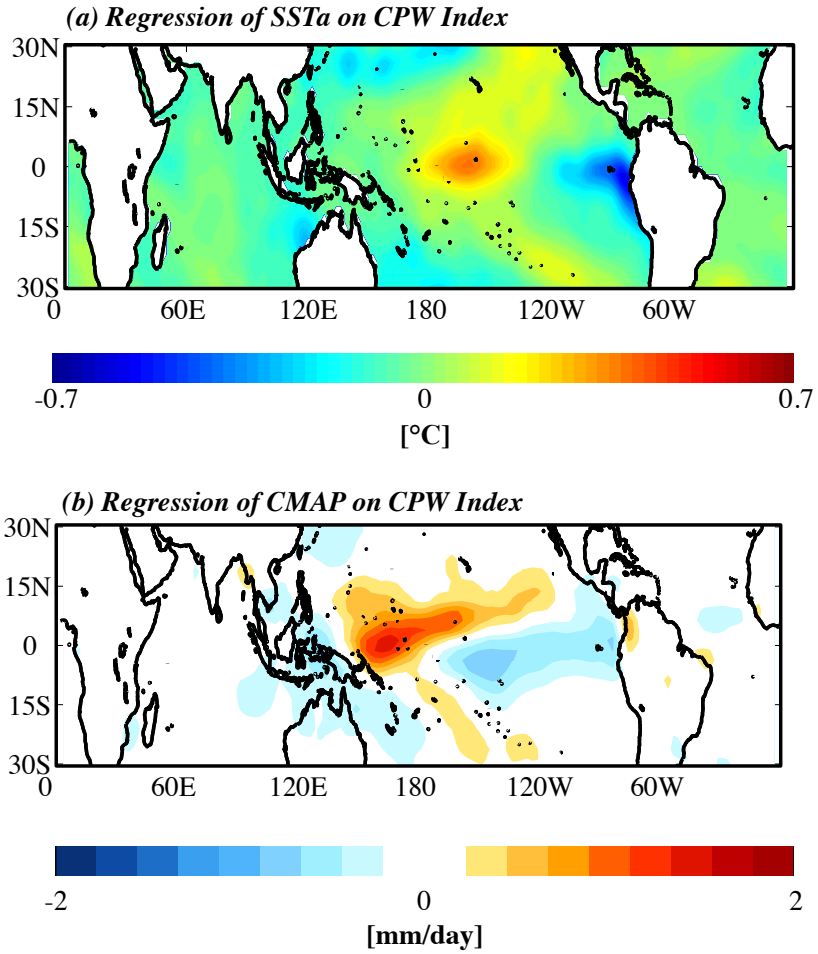

FIG. 5.7. Regression of (a) annual-mean tropical SSTa (°C) and (b) annual-mean tropical precipitation anomalies (mm/day) on the annually-averaged standardized CPW index. Compare with plots of Mode 2 in Fig. 5.6.

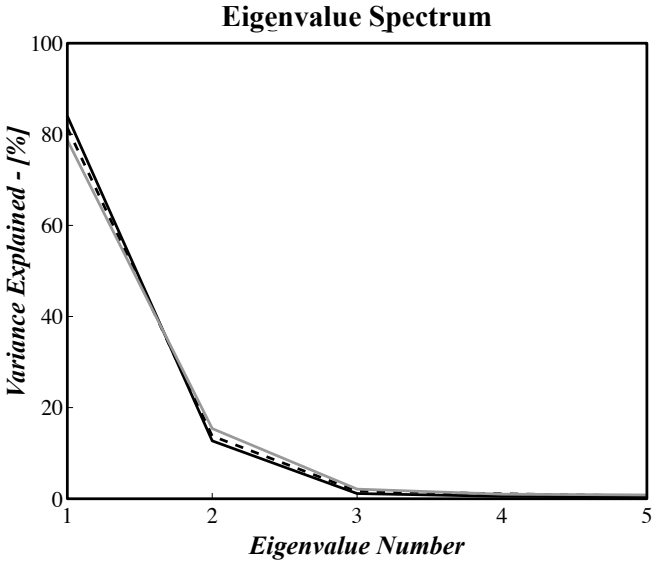

FIG. 5.8. The eigenvalue spectrum for the first five covariance modes between annual-mean tropical precipitation anomalies and annual-mean tropical SSTa, using the three precipitation datasets: CMAP (solid black), ICTP (dashed black), and ERA-40 (solid gray).

especially considering that the two largest positive ENSO events in recorded observational history occurred during that period (i.e., 1982-83 and 1997-98). Furthermore, observed changes in the character of Pacific variability after the 1976-77 climate shift (e.g., Trenberth and Hurrell 1994; Zhang et al. 1997) also introduce a source of bias to the 1979 - 2000 climate statistics. Increasing the length of our tropical precipitation and SST time series allows us to address the potential influence of nonstationarity in the joint statistics between the two variables. For this analysis, we rely on the 51-year (1950 - 2000) AGCM run. Results from Section 5.3 suggest that use of the model precipitation fields is reliable for assessing longer-term statistics because of the close match between the results from the model and those from observations.

Before proceeding with the 1950 - 2000 based reconstructions, we examine the difference in the patterns of covariability of the ICTP AGCM precipitation and NOAA ER SSTs from 1979 - 2000 (Fig. 5.6) with those from 1950 - 1978 and 1950 - 2000 (Figure 5.9). The major differences between the two periods arise in LSV-2 (i.e., the CPW-type mode). From 1950 - 2000, the Indian Ocean and eastern Pacific

Ocean are in-phase in terms of SSTa, similar to that shown in Fig. 5.6; however, for the 1950 - 1978 period, they are out of phase. In the precipitation domain, RSV-2 (Fig. 5.9) shows a more meridional tripole pattern, with positive anomalies along the equator flanked by negative anomalies to the north and south, compared to that from 1979 - 2000 (Fig. 5.6). Furthermore, the magnitude of the precipitation anomalies in Fig. 5.9 is lower than in Fig. 5.6. These lower amplitudes suggest a weaker linear relationship between SSTs and precipitation for the 1950 - 2000 period versus the 1979 - 2000 period, which could increase reconstruction errors. Overall, the differences in the second covariability mode between the 1979 - 2000 statistics and the 1950 - 1978 statistics suggest high sensitivity of our precipitation-SST relationship to the analysis period chosen. Similar results are obtained when regressing SSTa onto the annually-averaged CPW index for 1950 - 1978 and 1950 - 2000 (not shown).

Based on these findings, we conduct two new reconstructions whereby the mapping matrix in the multi-regression method ($\mathbf{E}$) consists of the covariability of tropical precipitation from the ICTP model run and tropical SSTa from NOAA ER SSTs from 1950 - 2000, but SST reconstructions are evaluated for: (a) 1950 - 2000, using model precipitation for the input precipitation vector ($\mathbf{x}$), and (b) 1979 - 2000, using CMAP precipitation data for $\mathbf{x}$. The first analysis tests how well the results presented in Section 5.3.2 hold for the longer time period. The latter case tests the possibility of using model-derived statistics from long integrations for climate pattern templates in lieu of data from the relatively shorter observational records of precipitation.

The first case (SST reconstructions for 1950 - 2000 using model precipitation over the whole period; Figure 5.10) yields poorer performance for the reconstructions than the 1979 - 2000 case (see Fig. 5.4). RMS errors nearly double in the cold tongue region (0.1 - 0.2°C) but larger changes are seen in the skill of the reconstruction (Fig. 5.10b). High reconstructive skill is now restricted to the central and eastern tropical

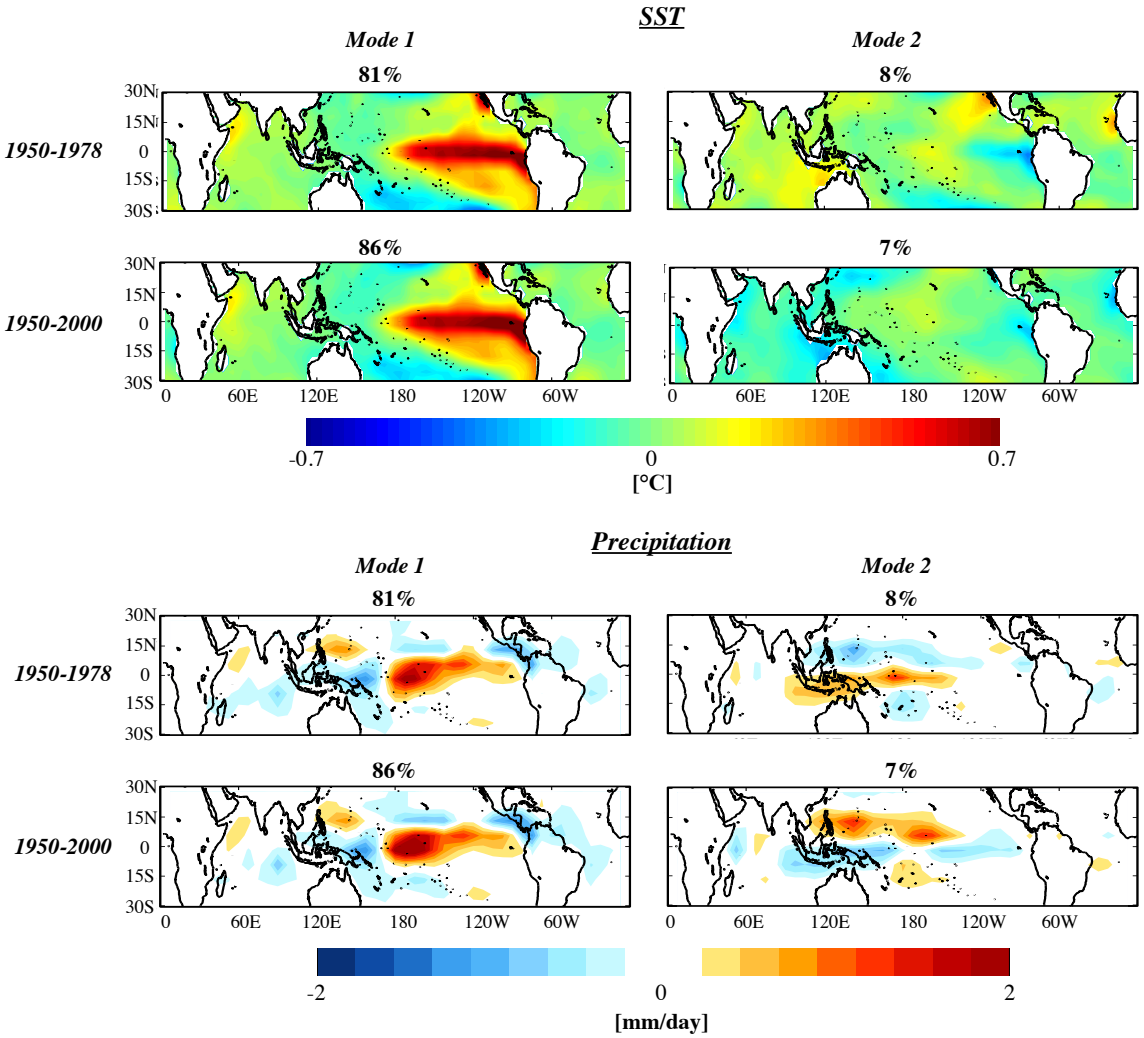

FIG. 5.9. The two leading modes of covariance between tropical SST and ICTP model precipitation anomalies (30°S - 30°N) for two different periods: 1950 - 1978 and 1950 - 2000. (top) Regression of annual-mean SSTa (°C) onto the first two EC time series from the LSVs of the SVD analysis. (bottom) Regression of ICTP precipitation anomalies onto the first two EC time series from the RSVs of the SVD analysis. Percent covariance explained by each mode is given in the title of each plot.

Pacific Ocean, and those skill values are about 25% lower than their counterparts in Fig. 5.4. Larger skill degradation is seen in the Indian Ocean and West Pacific Warm Pool region. The estimated skill field (Fig. 5.10c) reflects these changes in skill for the larger sample, though amplitudes are overestimated particularly in the West Pacific Warm Pool region. Finally, the spatial correlation coefficients (Fig. 5.10d) have higher temporal variance than Fig. 5.5b (gray curve) displays, but the coefficients are still

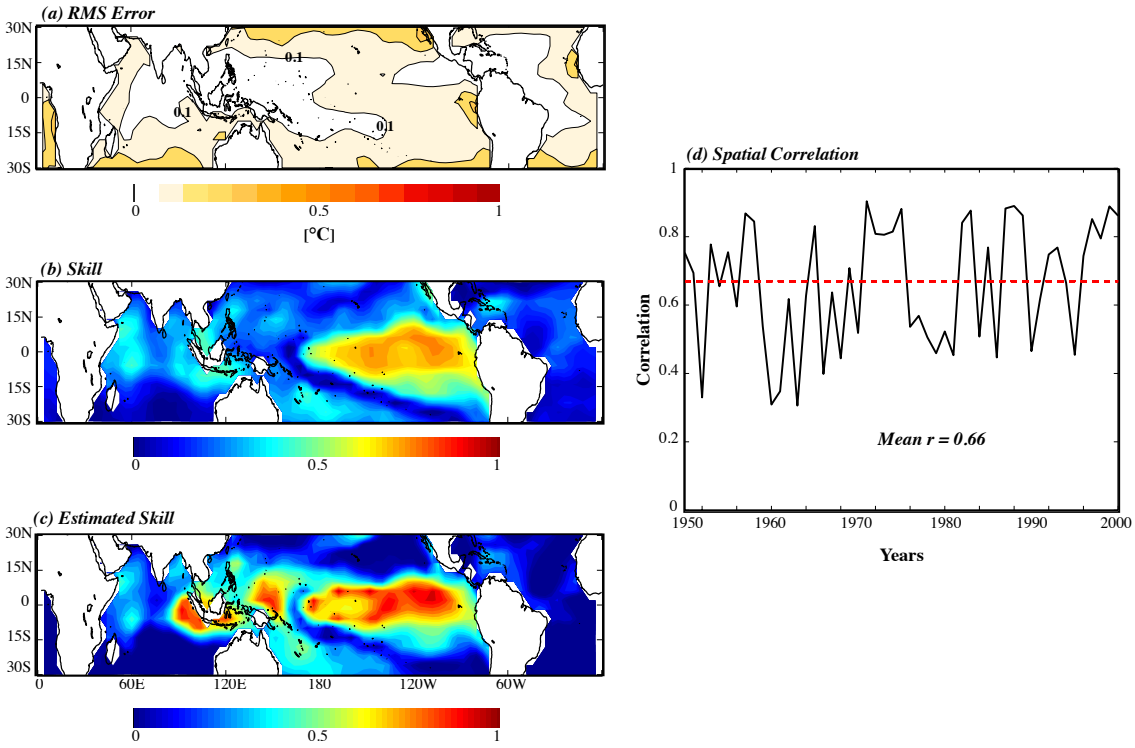

FIG. 5.10. Evaluation of the multi-regression method using NOAA ER SSTs and ICTP model precipitation fields from 1950 - 2000. (a) RMS error (°C). Contour interval 0.1°C. The 0.1°C contour is labeled for reference. (b) Reconstructive skill (dimensionless). (c) Estimated reconstructive skill (dimensionless). (d) Spatial correlation between the reconstructed and observed SSTa from 1950 - 2000. Red dashed line represents the 95% significance levels ($r = 0.64$). The mean correlation coefficient for the 51 years is also given.

all positive, and the mean correlation coefficient for the 51-year period ($r = 0.66$) is above the 95% significance level.

When considering the case of model-derived statistics from 1950-2000 with observational precipitation from 1979 - 2000 (Figure 5.11), the tropical SST reconstructions are even more degraded in skill than the reconstructions that use only instrumental data from 1979 - 2000. Note that the estimated skill levels (Fig. 5.11c) are identical to those in Fig. 5.10c since the same joint statistics are used in the multi-regression model. The RMS errors (Fig. 5.11a) approach 0.5°C in the far eastern tropical Pacific, and the mean skill of the reconstructions (Fig. 5.11b) displays only moderate skill ($\sim$0.5) throughout the eastern part of the tropical Pacific Ocean. In fact, the demonstrated skill in this case is almost similar (and even less) than the

skill shown using the EOF method for the eastern tropical Pacific (compare Fig. 5.3, top row, middle column with Fig. 5.11b). Skill decreases by approximately 40% in the tropical Pacific Ocean between Fig. 5.4 (top row, middle column) and Fig. 5.11b. Furthermore, little if any skill is demonstrated in the West Pacific Warm Pool region or the Indian Ocean. Finally, the mean spatial correlation coefficients (Fig. 5.11d) are no longer uniformly positive, and the mean correlation coefficient is statistically insignificant ($r = 0.55$). Only 10 of the 22 years ($\sim$45%) have significant spatial correlations between the reconstructed and observed SSTa, compared to 86% (19 of the 22 years) in Fig. 5.5a (gray curve).

Thus, when the multi-regression method is repeated using joint statistics of precipitation and SSTs from 1950 - 2000, the skill of the SST reconstructions decreases versus those performed using 1979 - 2000 statistics. Our observational analysis points

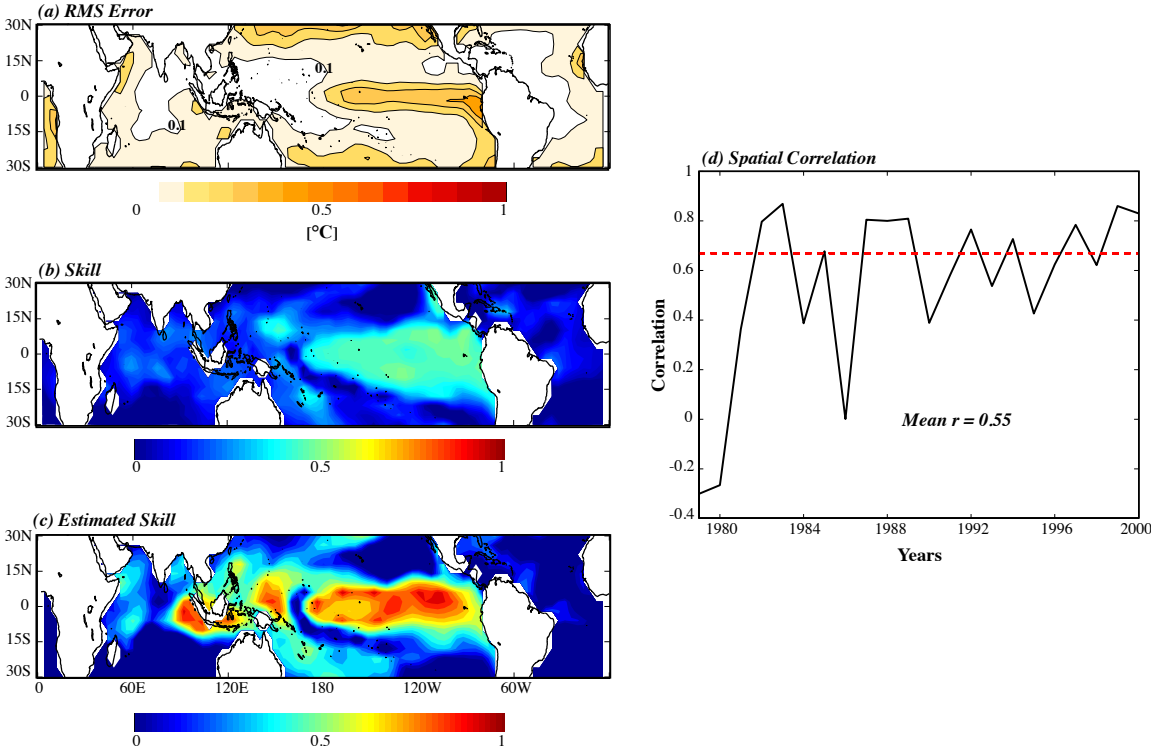

FIG. 5.11. As in Fig. 5.10 except evaluating SST anomaly reconstructions from 1979 - 2000 using SST-precipitation joint statistics from the ICTP model output for **E** and annual-mean CMAP precipitation anomalies for **x** in the multi-regression model.

to changes in LSV-2 and RSV-2 as the cause of the diminished skill. This change in the second leading mode of covariability likely reflects changes in the ENSO/CPW phenomenon. Implications of the change in this covariability mode may extend beyond tropical SST reconstructions to extratropical climate variability, owing to the far-reaching effects of tropical Indo-Pacific climate variability (e.g., Hoskins and Karoly 1981; Barsugli and Sardeshmukh 2002; Hoerling and Kumar 2002; Alexander et al. 2002).

5.5 Using the Multi-Regression Method with a Realistic Paleo-Precipitation Pseudoproxy Network

The previous analyses examined the sensitivity of tropical SST reconstructions to both the method employed and the degree of stationarity in the climate statistics. In this section, we reconstruct tropical SSTa by applying the multi-regression method to precipitation anomalies from locations corresponding to the pseudoproxy network defined in Table 5.1. We also consider the effects of errors in the proxy data on the resulting tropical SST reconstructions. For brevity, only results using CMAP data are shown; however, findings are similar if precipitation fields from the model control run or ERA-40 are used (not shown).

5.5.1 SST Reconstructions with the Pseudoproxy Network

Figure 5.12 displays the error statistics for tropical SST anomaly reconstructions for the period 1979 - 2000 using multi-regression and the precipitation proxy network in Table 5.1. The RMS error (Fig. 5.12a) and mean skill fields (Fig. 5.12b) illustrate that the network is able to capture SSTa in the central and eastern tropical Pacific Ocean when compared to the full field reconstructions (Fig. 5.4, top row). Higher RMS errors and consequently less skill exist for SSTa closer to the South American coast, despite having several precipitation proxies nearby. Reconstructive

skill in the Indian Ocean, however, is now lost with this pseudoproxy network (Fig. 5.12b). The mean skill matches well with the analytical estimate (Fig. 5.12c), while the spatial correlation coefficients are all positive with a statistically significant mean correlation of 0.67 (compared to 0.73 in Fig. 5.5a, gray curve). Overall, our specific pseudoproxy network captures almost 80% of the skill displayed using the full CMAP tropical precipitation field in the tropical Pacific, but only half of the skill in the Indian Ocean basin.

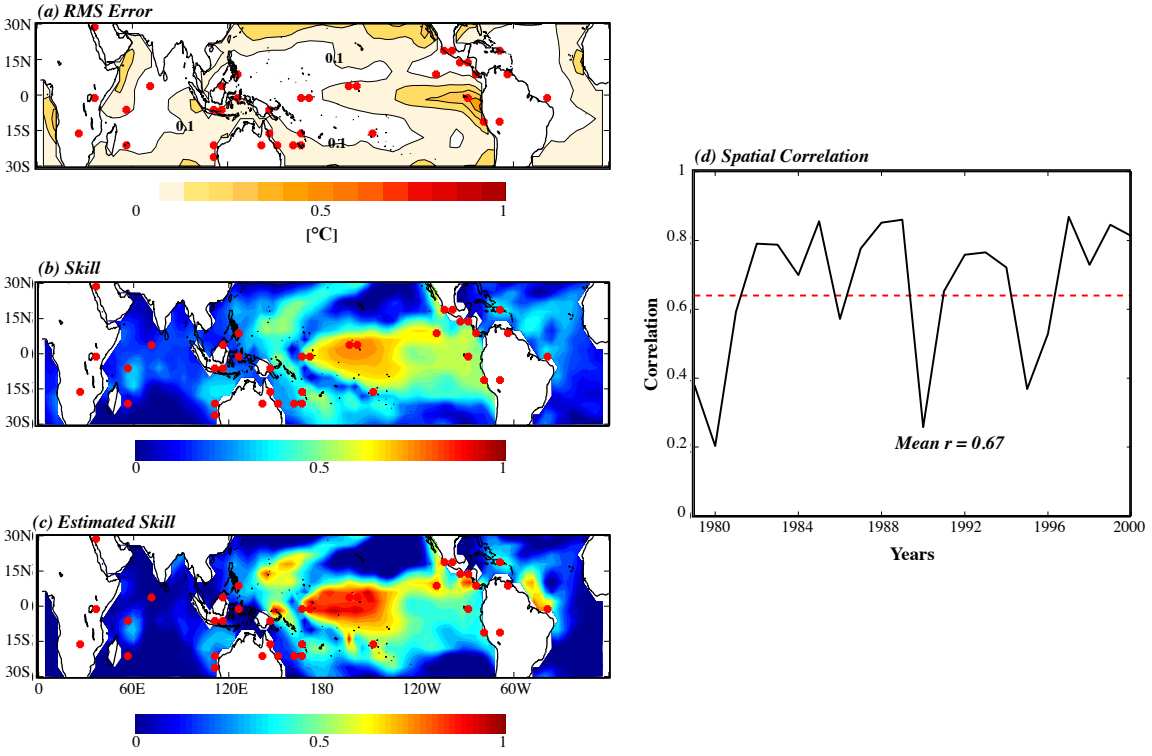

FIG. 5.12. Evaluation of the multi-regression method for SST anomaly reconstructions from 1979 - 2000 using paleo-precipitation pseudoproxies listed in Table 5.1. (a) RMS error (°C). Contour interval 0.1°C. The 0.1°C contour is labeled for reference. (b) Reconstructive skill (dimensionless). (c) Estimated reconstructive skill (dimensionless). (d) Spatial correlation between the reconstructed and observed SSTa from 1979 - 2000. Red dashed line represents the 95% significance level ($r = 0.64$). The mean correlation coefficient for the 22 years is also given. Red dots in (a) - (c) represent the locations of the pseudoproxies.

5.5.2 Error Propagation Analysis

The decrease in reconstructive skill using the pseudoproxy network suggests that the selected proxy network is missing key regions that are important for tropical SST reconstructions. In this section, we explore the importance of the spatial distribution of the proxy network sites and the potential errors associated with the precipitation proxy data.

To investigate the impact of errors in the pseudoproxy network on SST anomaly reconstructions, we make use of (5.8) and include a term on the right-hand side, $\mathbf{n}_p$, representing errors associated with the precipitation records contained in $\mathbf{x}$. With this additional error term, the estimate of SSTa now changes by some quantity, denoted $\mathbf{n}_{SST}$, changing (5.8) to $\hat{\mathbf{y}} + \mathbf{n}_{SST} = \mathbf{E}(\mathbf{x} + \mathbf{n}_p)$, where $\mathbf{E}$ is given by (5.7). From here, we directly find that

$$\mathbf{n}_{SST} = \mathbf{E}\mathbf{n}_{SST}. \tag{5.13}$$

(5.13) indicates that errors in precipitation are linearly related to errors in SST reconstructions via $\mathbf{E}$. For this analysis, precipitation errors are defined as $\mathbf{n}_p = \sqrt{\frac{\mathrm{var}(\mathbf{x})}{\mathrm{SNR}}}$, where SNR is the signal-to-noise ratio. Furthermore, we test the impact of the spatial distribution of these errors by assigning non-zero $\mathbf{n}_p$ at all proxy sites and then assigning non-zero $\mathbf{n}_p$ only to specific sites in the proxy network.

Figure 5.13 illustrates the results of the error propagation analysis as a function of the SNR and the spatial location of errors. The absolute errors in SSTa range from $0 - 0.5$°C, which is the same order of magnitude as the standard deviation in tropical Pacific SSTs (Fig. 5.2b), making these errors significant for climate reconstructions. As expected, decreasing the SNR (i.e., increasing $\mathbf{n}_p$) creates larger absolute errors in the reconstructions. SSTa in the West Pacific Warm Pool are the exception - there, SST errors remain near zero for both cases because RMS errors are low there already (Fig. 5.12a). Comparing rows in Fig. 5.13 (i.e., examining the dependence of $\mathbf{n}_{SST}$ on the spatial distribution of $\mathbf{n}_p$), errors in easternmost tropical Pacific SSTs

are larger when $\mathbf{n}_p$ is nonzero for *Eastern* Hemisphere proxy sites versus when $\mathbf{n}_p$ is nonzero in the *Western* Hemisphere (compare the second and third rows of Fig. 5.13). These regions include the few proxy sites in and near the Indian Ocean as well as those near Australia and the poleward flank of the South Pacific Convergence Zone (SPCZ; e.g., Streten 1973; Spencer 1993). Surprisingly, estimates of SSTa over the cold tongue region are less accurate when proxy sites in the Western Hemisphere have no error. This finding could be because of the greater number of ENSO-sensitive pseudoproxy sites in the Eastern Hemisphere. Another interesting possibility is that Eastern Hemisphere proxies capture key dynamical links between the Indian Ocean and the tropical Pacific Ocean, a topic garnering significant attention in tropical climate studies (Barnett, 1984; Yu et al., 2002; Kug and Kang, 2006).

Outside of the tropical Pacific cold tongue region, the regions that are most sensitive to errors in proxy precipitation anomalies lie in the northwest and southwest Pacific Ocean. In the Indian Ocean, $\mathbf{n}_{SST}$ is more dependent on the SNR than on the spatial distribution of $\mathbf{n}_p$ in the proxy network, though $\mathbf{n}_{SST}$ is small there anyways. Based on this analysis and our earlier evaluations of the reconstruction methods, assessing SST reconstructive skill in the Indian Ocean remains difficult, primarily because of the small variance in SSTs exhibited in this basin (Fig. 5.2b).

SNR values used in this study are one to two orders of magnitude higher than those used in other pseudoproxy studies (e.g., Mann and Rutherford 2002; Mann et al. 2007). Mann et al. (2007) relate their SNR choices to the average correlation of the proxy data from their network to a local climate signal (temperature) with the equation

$$r = \frac{\mathrm{SNR}}{\sqrt{\left(1 + \mathrm{SNR}^2\right)}} \tag{5.14}$$

Using the same equation for SNR = 10 (SNR = 2), the implied correlation of the proxy data from our multi-proxy network with local precipitation anomalies is 0.99 (0.89). While we assumed a very large correlation for the proxies by choosing such

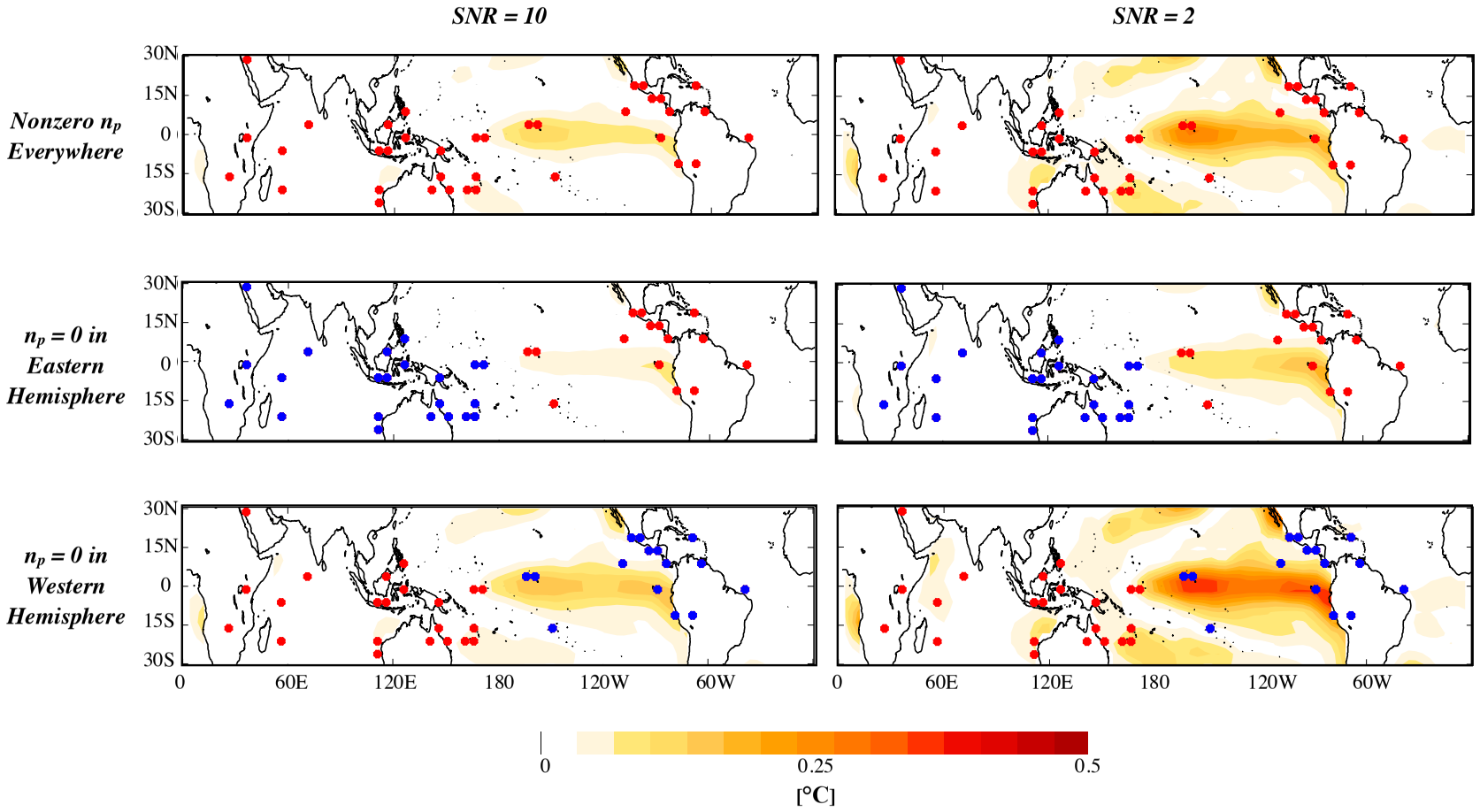

FIG. 5.13. The absolute error of the SST reconstructions (°C) using the multi-regression method resulting from assumed errors ($\mathbf{n}_p$) in CMAP precipitation records in the pseudoproxy network. Red dots show the locations where non-zero $\mathbf{n}_p$ is applied to pseudoproxies, while blue dots indicate perfect pseudoproxies (i.e., $\mathbf{n}_p = 0$). Each case is also labeled on the left-hand side. Absolute errors also shown as a function of SNR: (left) SNR = 10; (right) SNR = 2.

SNR values in this analysis, SST errors in the cold tongue region are still significant ($\sim$1 standard deviation) when $\mathbf{n}_p$ is non-zero in Eastern Hemisphere records. For comparison, with SNR = 0.4 ($r = 0.37$), errors in the central tropical Pacific are $\sim$1.0 - 1.2°C when $\mathbf{n}_p$ is non-zero in Eastern Hemisphere records (not shown). Therefore, although our SNR values are large compared to other studies, our study focuses on the spatial dependence of the SST reconstructive skill (i.e., how Indian Ocean proxies affect tropical Pacific SST reconstructions).

5.6 Chapter Summary and Discussion

The results presented in this chapter primarily offer insight into the feasibility of using two popular methods that have been applied for SST anomaly reconstructions over the last millennium. The analyses presented use tropical precipitation anomalies to directly estimate tropical SSTa. Since many proxies used in reconstruction efforts do record past precipitation more directly than past SSTs, this approach outlines strategies for taking advantage of such paleo-precipitation records. Furthermore, as these strategies are based on dynamical links that exist between tropical precipitation anomalies and SSTa, they provide additional insights into the coupled ocean-atmosphere system. We have shown that much of the variance ($> 80\%$) of the observed SSTa can be reconstructed using the multi-regression method, which significantly outperforms the EOF method in the tropical Pacific and Indian Oceans. The advantage of the multi-regression method lies in the second mode of covariability between SSTs and precipitation, which explains nearly 15% of the covariability between the two variables. Through comparison of the regression patterns (Fig. 5.7) and correlation of the two indices, we have concluded that, indeed, the second leading covariability mode between tropical SSTa and tropical precipitation anomalies coincides with the CPW phenomenon. Therefore, representing and accounting for

the CPW mode is necessary to improve tropical SST reconstructions for paleoclimate ventures and thus improve our understanding of constraints on future climate change globally. The presence of the CPW phenomenon in model-based or observational data should thus be a prerequisite for the pursuit of tropical Pacific SST reconstructions. Doing so may also provide insight into improving climate model representations of tropical-extratropical climate interactions, both oceanic and atmospheric.

Moreover, transient changes in the SST-precipitation statistical relationship limit the skill of tropical SST reconstructions. The degradation in reconstructive skill experienced between using 1979 - 2000 and 1950 - 2000 statistics (compare Figs. 5.10 and 5.11) clearly illustrates that reconstructions done using the multi-regression method are sensitive to shifts in the climate system such as that which occurred in 1976-77. This regime change is associated with changes in the evolution of individual ENSO events, which altered the tropical SST-precipitation relationship. Such changes also affect the CPW phenomenon in the same manner, illustrating that this mode and its global teleconnections may not be stationary in time. Developing reconstruction methods that account for different ENSO modes apparent in the data for different periods of time would therefore greatly improve Indo-Pacific SST reconstructions.

This study also provides some insight on the design of optimal networks of paleo-precipitation records for tropical SST reconstructions. The realistic paleo-precipitation proxy network chosen for this study preserves much of the reconstructive skill achieved when full-field tropical precipitation data are used. Decreased proxy-based skill in the Indian Ocean may reflect the low number of proxies located in the Indian Ocean (Fig. 5.2a) and/or gaps in the network from remote locations where precipitation is sensitive to Indian Ocean SSTs. A similar explanation may apply to decreased reconstructive skill throughout the tropical Pacific Ocean when using the proxy network. Indeed, the error propagation analysis illustrates the importance

of proxies in the Indian Ocean and SPCZ region for improved skill in tropical Indo-Pacific SST reconstructions (Fig. 5.13). Previous studies (e.g., Evans et al. 1998, 2002) corroborate these findings and highlight the importance of Indian Ocean proxy records for tropical Pacific SST reconstructions. Future modeling studies of coupled dynamics between the Indian and tropical Pacific Oceans would help to identify specific regions in the Indian Ocean for proxy generation. Precipitation sensitivity studies using adjoint models (e.g., $\mathbf{E^T}$ for the multi-regression model; Wunsch 2006) could also prove valuable in designing an optimal paleo-precipitation network. The complication with this approach is the low variance in the Indian Ocean compared to the tropical Pacific Ocean, which makes it harder to identify SST-related precipitation changes.

The paleoclimate SST reconstruction project presented in this chapter also illustrates the utility of performing climate field reconstructions to expand our current understanding of the climate system. By examining errors in both space and time, we identified several additional research questions related to tropical climate dynamics. Such reconstructions therefore offer a distinct advantage over reconstructions focused on a single index (e.g., Northern Hemisphere temperature or the NINO3.4 index), which do not provide any dynamical insight.

CHAPTER VI

CONCLUSIONS

6.1 Dissertation Summary and Discussion

Tropical and extratropical North Pacific climate variability on interannual to multi-decadal scales impact a wide range of systems, from local biological and ecosystems in the North Pacific to global teleconnections in weather and climate. The climate community thus far has concentrated efforts on better understanding the dynamics and the predictability of the three leading modes of atmospheric and oceanic variability in the Pacific: ENSO, the AL, and the PDO. While the effects of these three modes on the climate system are large and significant, secondary modes of variability in the tropical and extratropical Pacific (i.e., the CPW, the NPO, and the NPGO) also have significant and very different markers on biological systems and global climate. Two examples include the ability of the NPGO, not the PDO, to explain low-frequency changes in biological variables off the coast of California (Di Lorenzo et al., 2008) and the different atmospheric response in the North Pacific to CPWs vs. canonical ENSO events (e.g., projection onto the AL for the canonical ENSO vs. projection onto the NPO for the CPW). The latter effect is especially important, considering the climate models predict increased frequency and magnitude of CPWs in the future (Yeh et al., 2009).

The five original tasks presented in Section 1.3 were tackled through a series of statistical and dynamical analyses, using both observations and output from coupled climate models and experiments run with a simple AGCM. This dissertation offers evidence that includes the CPW, NPO, and NPGO into a more complete framework of Pacific decadal climate variability in the basin. As such, new avenues and efforts

to improve the predictability and the dynamics of NPDV/tropical Pacific variability emerge.

The study began by analyzing the basic dynamics and links between the NPO and tropical Pacific SSTa variability (Chapter 3). Dissecting the NPO into its two poles and examining the behavior of each pole separately illustrates that the NPO phenomenon may be stochastic as defined, but the two nodes are not wholly stochastic. As shown in the power spectra analyses (Fig. 3.5a), the NPO and NPO NP indices are white-ish, but the NPO SP contains significant power at lower frequencies (along with weak power at high frequencies). This low-frequency component is also replicated in a long station record from Honolulu, Hawaii, which resides within the NPO SP (Fig. 3.5b). Moreover, Table 3.1 reveals that, in the observations, the NPO and NPO NP are nearly identical, indicating that the traditional definition of the NPO is dominated by high-latitude SLPa variability. The weaker (though still significant) correlations between the NPO NP and NPO SP indices indicate that, although 25% of the variance in one is related to variations in the other, 75% is due to other factors. This, along with the power spectra results, illustrate that we the two centers of action should be considered independently, as they are mostly governed by different dynamics. The NPO NP is more intrinsic and is driven mainly by atmospheric "noise", thus producing a white-ish power spectrum. By contrast, the NPO SP, though it does contain high-frequency variability, is driven by tropical Pacific SSTa variability (e.g., Di Lorenzo et al. 2010), which contributes to variability at both high and low frequencies. Indeed, when the NPO index is low-passed and correlated with SLPa, the NPO NP node nearly vanishes, while the subtropical node of the NPO remains significant but shifted in location toward the east (Fig. 3.4c).

The dynamics of the NPO were also explored in frequency-space for two specific frequency bands - high-frequency (periods < 2 years retained) and low-frequency

(periods > 7 years retained). These two bands fundamentally represent two different processes in the Pacific climate system. The high-frequency band describes the seasonal ENSO precursor pattern in SLPa and SSTa, while the low-frequency band depicts decadal-scale changes in the North Pacific and tropical Pacific, particularly those driven by CPW-type variability, which also contains quasi-decadal power (Fig. 3.3a). The observational evidence showed that, for the four indices measuring NPO-type variability (NPO, NPO NP, NPO SP, and SLPa Hawaii indices), the high-passed versions of the NPO SP and SLPa Hawaii indices captured as much *or more* of the variance in boreal winter SSTa as the other two high-passed indices (Figs. 3.6a - 3.6d). Moreover, through lag correlation analysis, the high-passed NPO indices clearly captured the propagation of SSTa from the subtropics to the tropical Pacific, consistent with the SFM (Figs. 3.6e - 3.6l). As with the lag 0 plots, the high-passed NPO SP and SLPa Hawaii lag correlation maps alone were able to capture the propagation, with even stronger correlations seen than for the high-passed NPO index. Thus, it is the NPO subtropical node that is the most important for the ENSO precursor pattern/SFM, consistent with findings in previous work (e.g., Anderson 2003; Alexander et al. 2008).

For the low-passed indices, the NPO NP index correlations are a maximum in the far North Pacific and the weakest among the three indices in the subtropical North Pacific and tropical Pacific (Fig. 3.7). Both the NPO SP and SLPa Hawaii indices accurately reconstruct the CPW-type pattern in the Pacific at low frequencies (Fig. 3.7c - 3.7d). Additionally, the low-passed NPO SP and SLPa indices are significantly correlated with the low-passed CPW index (Figs. 3.8c and 3.8d). However, this is not the case for the low-passed NPO or NPO NP index, both of which have an insignificant correlation with the low-passed CPW index (Fig. 3.8a and 3.8b). The time series results lend further support to the very different fundamental characteristics of the two poles of the NPO and their links to the North Pacific - tropical Pacific climate

system.

Because of the statistical connections between the CPW and the NPO, particularly in the SLPa field at low frequencies (Figs. 3.4a and 3.4c), along with the quasi-decadal periodicity of the CPW index (Fig. 3.3a), the hypothesis was proposed that low-frequency variability in the NPO SP originates from tropical Pacific SSTa forcing. The power spectra of the TROP runs support this hypothesis: the low-frequency characteristic of the NPO SP/SLPa Hawaii indices is still recovered in the tropically-forced only runs. When examining the the SSTa correlation maps with the low-passed ICTP model indices, the patterns for the low-passed NPO SP and SLPa Hawaii in the CONTROL and TROP runs match well with the observations (Fig. 3.9). That is, the low-frequency nature of the NPO SP indeed projects strongly onto the central tropical Pacific SSTa field, in a pattern like that of the CPW phenomenon. Note, however, that the model shows very weak correlations for the low-passed NPO/NPO NP index correlation maps in the tropical Pacific for both runs. This implies that, for the TROP run in particular, the tropical Pacific SSTa forcing projects primarily onto the NPO SP/Hawaiian SLP region only at low frequencies. Moreover, the results from Di Lorenzo et al. (2010) agree with these findings and also illustrate that the NPGO, a signature of NPDV, has direct ties to variability in the NPO subtropical node and indirect ties to CPW activity. Thus, a new link between the CPW, the NPO, and the NPGO is created, akin to the ENSO-AL-PDO framework.

With the newly identified connections between the NPO, CPW and NPGO at low frequencies, the analysis then turned to evaluating the leading modes of NPDV as simulated by the 24 coupled climate models used for predictions of projected climate change made in the IPCC AR4 (Chapter 4). When the analysis is restricted to the North Pacific only, the models are able to reproduce well the spatial structure of the two leading North Pacific SLPa modes (i.e., the AL and the NPO; Fig. 4.2), while the oceanic modes exhibit much more scatter and inconsistency between models. For

the leading mode (i.e., the PDO), the models simulate well the decadal-scale power of the mode. However, the observed covariability between the PDO and the AL, its atmospheric forcing, is far stronger in the models than it is in observations (Fig. 4.7), suggesting a shorter decorrelation timescale of the PDO mode in the models. Hence, the coupled climate models generally reproduce inaccurate mechanisms and dynamics associated with the AL/PDO mode.

The second leading mode of North Pacific SSTa is much more problematic for the models. Though the spatial correlation of the ensemble-mean pattern with the observed EOF-2_{SST} is high and significant (Fig. 4.2), the pattern itself is much weaker in magnitude (Fig. 4.1d). Furthermore, the EC-2_{SST} index in the models exhibits very strong power at the interdecadal timescales, as opposed to the observations which contain two peaks: one at interannual timescales and the other in the 7-12 year range (Fig. 4.3b). Physically, the double-peak in observations is likely related to the relation of this SST mode to ENSO/CPW variability (the interannual peak) and then the low-frequency changes that are most characteristic of the NPGO (recall that the observed SSTa pattern associated with the NPGO is highly similar to the one in EOF-2_{SST}). Unfortunately, the models do not replicate this dual-nature, again pointing to disconnects between tropical-extratropical Pacific mechanisms at work in the models. Furthermore, when testing the role of NPO forcing on driving the underlying SST field, the models display the opposite effect of the AL/PDO relationship: many models *underestimate* the variance explained or simply have no significant correlation between their NPO and covarying SSTa pattern (Fig. 4.8b). This lack of covariability, unlike the relatively strong signal seen in observations (Fig. 4.8a), is readily apparent from the structure of the ensemble-mean cEOF-2_{SST} (Fig. 4.6d), which has little resemblance to the observed NPGO-like SSTa pattern.

Further evidence of poor representation of the NPO/NPGO decadal signature in the North Pacific arises when analyzing the representation of the tropical Pacific

teleconnections to the North Pacific (Fig. 4.11). The remote connections between ENSO and the AL are insignificant in the models, thus suggesting poor simulation of the atmospheric bridge mechanism. This lack of tropically-induced forcing may also explain why the PDO index is far more dependent on high frequency forcing from the AL than observations indicate, as there is not a lower frequency modulator of the PDO from the tropics to damp the response. Additionally, the ensemble-mean of the models do not capture the atmospheric teleconnections associated with the CPW in the North Pacific (Fig. 4.11c). Unlike the NPO-like response seen in observations, the ensemble-mean response resembles more the AL representation in the models, thus the strong connection between the EC-$2_{\mathrm{Tropics-SST}}$ and EC-1_{SST} indices in many models (Table 4.4). Note that this result is *not* a fact of the order of the models' EOFs not matching the observations - the ensemble-mean cEOF-$2_{\mathrm{Tropics-SST}}$ indeed captures the CPW phenomenon (albeit the center of action is shifted to the west; Fig. 4.11d). The lack of the NPO-like response may also hint at the lack of a strong ENSO precursor signature in the models, though explicit tests for that mechanism were not done in this study. Thus, the CPW-NPO connections in the models must be addressed in future studies.

Finally, the inclusion of the CPW mode was shown to offer significant improvement in paleoclimate tropical SST reconstruction methods (Chapter 5). Using precipitation as a proxy for reconstructing tropical SST, the analysis showed that the multiregression method (which includes the canonical ENSO and CPW modes, among higher order, weaker modes) far outperformed the EOF method (which only considers canonical ENSO) throughout the tropical Indo-Pacific basin (Figs. 5.3 vs. 5.4). The key to this improvement was the inclusion of the second mode of covariability associated with the CPW, which explains nearly 15% of the covariance between annual-mean tropical precipitation and tropical SSTa (Fig. 5.6). In fact, the presence of another "flavor" of ENSO as dominant and significant as the CPW discourages

future ventures in paleoclimate reconstructions from seeking to reconstruct, for example, the NINO3.4 index as a way to reconstruct and understand past climates. Reconstructing a single index of tropical Pacific variability will surely miss other contributing elements of the complex ENSO system and may give a false representation of past climates. Furthermore, since paleoclimate research seeks to test hypotheses of climate variable relationships and provide past climate conditions used to validate climate model simulations, biasing tropical SST reconstructions to only one type of ENSO neglects the very different contributions of other flavors of ENSO on the climate system. Additionally, nonstationarity in the statistics of ENSO behavior was also shown to be a large factor in the skill of reconstructions (Figs. 5.10 and 5.11), a commonly accepted criticism for reconstruction validation.

The paleoclimate reconstruction exercise also demonstrated the importance of collecting a multiproxy network that spans the entire tropical ocean, not just in the eastern and central tropical Pacific. The error propagation analysis (Fig. 5.13) illustrated that tropical Pacific SSTa reconstructions were most sensitive to high errors in the Indian Ocean/Indonesian precipitation proxy records, not to local eastern Pacific records. Thus, remote influences on the tropical Pacific from the Indian Ocean play a key role in accuracy of the paleoclimate SST reconstructions. Future ventures for paleoclimate sites for those interested in past tropical Indo-Pacific conditions should focus on records in the Indian Ocean region.

6.2 The Future

6.2.1 A New View on Tropical Pacific - North Pacific Interannual and Decadal Variability

The overall results of this dissertation, particularly those of Chapter 3, allow us to add to the original framework of North Pacific - tropical Pacific presented in Fig. 1.8. This new proposed framework is presented in Figure 6.1, which includes

an additional "wheel" showing the contributions of the NPO, the NPGO, and the CPW to Pacific interannual and decadal variability. Examining the blue wheel, NPO variability, mostly associated with the subtropical NPO node/SLPa Hawaii variability, acts on two frequency branches: (a) the low-frequency branch (blue), where the atmospheric forcing is integrated by the North Pacific to form the NPGO, and (b) the high-frequency branch (light blue), where NPO variability is tied to the ENSO precursor pattern/SFM. The SSTa field associated with the ENSO precursor pattern projects strongly into the central Pacific Ocean SSTs during the late spring and summer months, producing anomalous warming in that region. Here, a juncture in the diagram is present. The anomalous warming of the sea surface in the central equatorial Pacific Ocean may produce[7] a canonical ENSO episode (the purple branch), or a CPW-type ENSO (the blue branch). Depending on which type of ENSO ensues, the North Pacific extratropical atmosphere and ocean will react differently. Should a canonical ENSO event occur, then the red wheel outlines the teleconnection patterns. If a CPW-type event forms, then the evolution follows the blue wheel chain of events, which leads back to a projection onto the NPO pattern, particular at quasi-decadal frequencies.

One element of Fig. 6.1 is that, though components in both wheels may operate simultaneously, there are likely periods of time when the red wheel linkages are more prevalent, while others the blue wheel dominates the climate system. Since studies of future climate change focus on changes in the magnitude and frequency of individual modes like the PDO, NPGO, and ENSO, this new framework offer a convenient way to picture the chain of events that may ensue or the responsible dynamics for those amplified modes.

[7]Of course, an ENSO event may not be produced at all, as the ENSO precursor pattern / SFM does not guarantee an event will occur. Exactly why or why not an event occurs is an outstanding question, though recent work by Alexander et al. (2010) offers some preliminary evidence for prediction of the path taken.

There are noticeable "gaps" in the wheels, which represent areas that need future work. For example, in the blue wheel, no branch connects the NPGO to the anomalous warming of the central tropical Pacific Ocean or to CPW activity. The statistical analyses surely make this branch highly likely to exist, as the CPW and NPGO share common correlations in the central tropical Pacific Ocean. However, future modeling studies will need to be performed to look for this connection. Likely, this connection is not purely an "atmospheric bridge" response - there could be oceanic principles at work. The diagram also continues to have a break between the PDO and ENSO. There are oceanic mechanisms proposed that relate subtropical and extratropical North Pacific ocean waters back to the equatorial Pacific, but more work is needed to tie these oceanic "tunnels" to the ENSO-AL-PDO wheel.

6.2.2 Future Research Ideas

Below are several ideas for future work that will build upon the conclusions and results reached in this study.

1. *Conduct an "atmospheric bridge" analysis similar to Alexander et al. (2002) but for the CPW phenomenon.* Fig. 3.10 presented preliminary evidence that indeed the Rossby wavetrain excited by the CPW phenomenon has a unique projection onto the North Pacific atmosphere and contributes to enhanced variability of the NPO SP/upper tropospheric SLPa Hawaii signature. Though previous studies have presented evidence of teleconnection patterns associated with the CPW (e.g., Ashok et al. 2007; Weng et al. 2007; Ashok et al. 2009; Weng et al. 2009), a more complete dynamical picture of the CPW links to the extratropical Northern Hemisphere remains undone. Such a project would involve both observational analyses and also experiments done with coupled-climate models, mirroring work done by Alexander et al. (2002). Future work may start with the proposed mechanism suggested in Section 3.6 as the seed to build a more

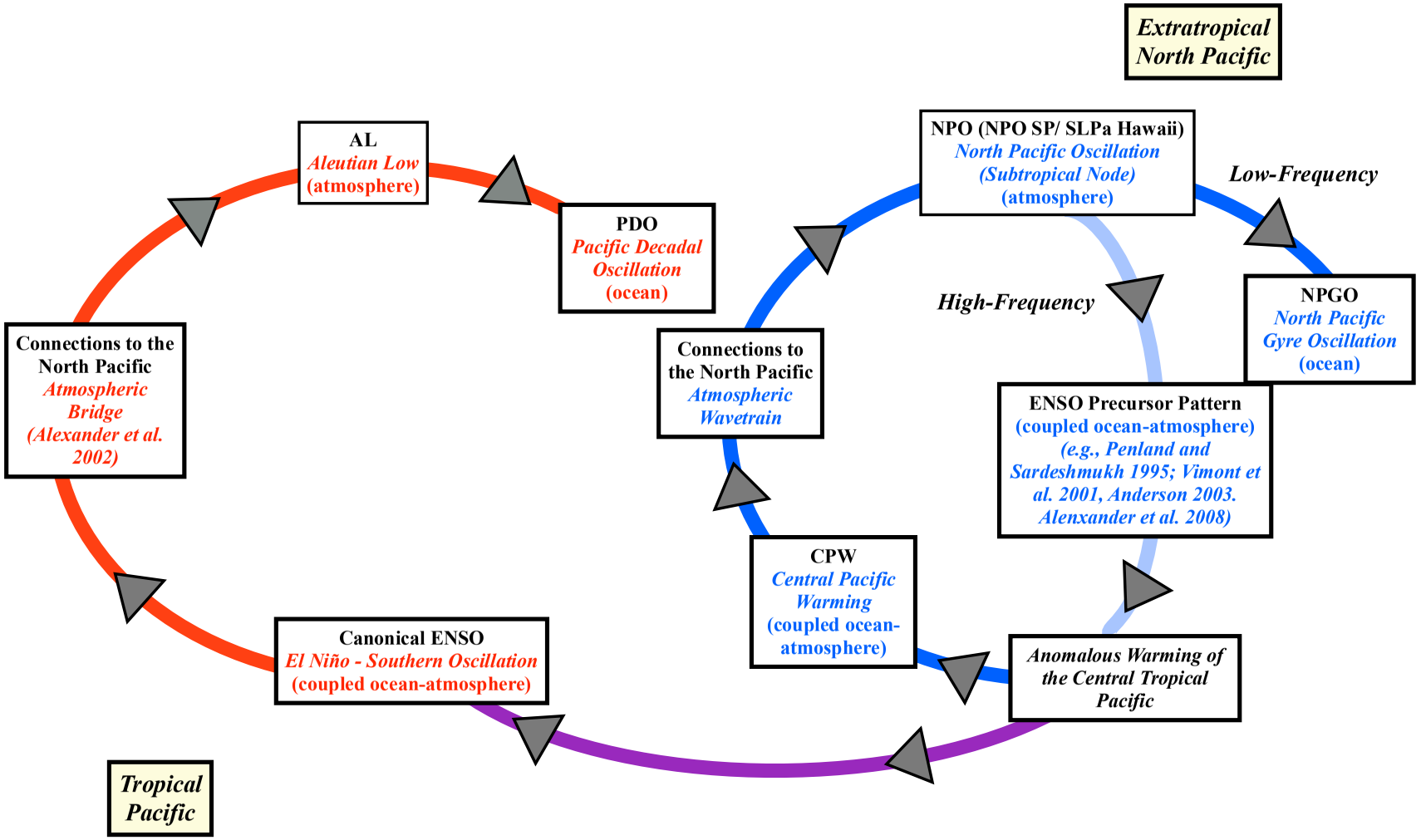

FIG. 6.1. A proposed new framework for North Pacific and tropical Pacific interannual and decadal climate variability, including dominant modes of variability and mechanisms at work. The purple curve represents the link between the ENSO-AL-PDO wheel (red) and the CPW-NPO-NPGO wheel (blue).

complete dynamical analysis of changes in storm tracks and associated feedbacks to better understand these teleconnection patterns for improvement of predictability of seasonal forecasts and for long-term climate projections.

2. *Investigate more in-depth why certain models are unable to represent the second mode of NPDV variability (i.e., the NPGO-like SSTa pattern) and its relationship to the tropics.* The analysis of the IPCC models clearly showed that the second leading mode of North Pacific SSTa variability is poorly connected to its overlying atmospheric forcing pattern (i.e., the NPO; Fig. 4.8) and is also disconnected from CPW-type activity in most of the models (Fig. 4.11). However, the study did not offer reasons why certain models may capture these relationships better than others (see correlations in Fig. 4.8b and Table 4.4). The answer likely lies in the differences in oceanic models used in for each model, including their coupling schemes. Future studies should investigate differences in dynamics or configurations among the various oceanic model components to build a better understanding of these differences and improve the "poorer performing" models.

3. *Evaluate the existence of the ENSO precursor pattern in the coupled climate models.* The analysis of NPDV in the IPCC coupled climate models focused on decadal-scale patterns of variability and did not treat the high-frequency signature of the NPO and its involvement in the SFM. One start would be to repeat the canonical correlation analysis done in Anderson and Maloney (2006) for the 24 IPCC models. This would be a straightforward way to assess the ENSO precursor pattern. However, assessing if the models then produce an ENSO event through the WES feedback path (Vimont et al., 2009) or the recharge/discharge mechanism path (Anderson and Maloney, 2006) would involve delving into the

ocean models, heat flux parameterizations, and subsurface temperature structures. Such a study could run tandem with (2) above and could provide a nice critique on issues with the models and subtropical - tropical Pacific Ocean conditions.

4. *Continue reconstruction projects of tropical Pacific SSTa, but incorporate more paleo-precipitation proxies from the Indian Ocean.* The Indian Ocean serves as the site of the origination of the Madden-Julian Oscillation (Madden and Julian, 1971, 1994), and variability in the basin has been linked to variations in the tropical Pacific (Barnett, 1984; Yu et al., 2002; Kug and Kang, 2006), which can then influence North Pacific climate variability through the atmospheric bridge mechanism. Unfortunately, the Indian Ocean basin remains relatively devoid of paleo-precipitation records. So, efforts in the future should concentrate on acquiring more records in the region (e.g., through corals or land records like those found in cave records) to improve our knowledge on changes in ENSO behavior. This venture may also work in conjunction with coupled climate model simulations which could locate prime locations for proxy recovery and also assist in improving the nonstationarity issue of ENSO and the skill of the reconstruction methods. The additional proxies in the Indian Ocean may add a further constraint onto the type of ENSO events prevalent during certain times in the recent past and assist in improving the simulation of the CPW phenomenon in future climate simulations.

5. *Critique the proposed new viewpoint presented in Fig. 6.1 with more complex models.* The foundations for the CPW-NPO-NPGO connections were assessed using a simple AGCM forced with prescribed SSTs (both globally and in the tropical Pacific only for the TROP runs). These runs were sufficient to affirm

our hypotheses, but the model cannot offer insights into any coupled ocean-atmosphere feedbacks that could be important in this framework. This is especially true for testing the high-frequency links suggested by observations. Choosing an appropriate model may be difficult, given the poor representation of tropical - North Pacific atmospheric teleconnections in most CMIP3 coupled climate models. However, improvements in later stages of the models (e.g., the CMIP5 models, currently available for analysis as of the writing of this dissertation) may be adequate to test any such ocean-atmosphere feedbacks. Moreover, the proposed framework deals almost strictly with atmospheric bridge-only mechanisms. While this scenario is accepted, oceanic pathways that could be important (e.g., Gu and Philander 1997; Schneider et al. 1999) should be assessed further and potentially added to the diagram.

Bibliography

Alexander, M. A., C. Deser, and M. S. Timlin, 1999: The reemergence of SST anomalies in the North Pacific Ocean. *J. Climate*, **12**, 2419 – 2433.

Alexander, M. A., I. Bladé, M. Newman, J. R. Lanzante, N.-C. Lau, and J. D. Scott, 2002: The atmospheric bridge: The influence of ENSO teleconnections on air-sea interaction over the global oceans. *J. Climate*, **15**, 2205–2231.

Alexander, M. A., L. Matrosova, C. Penland, J. D. Scott, and P. Chang, 2008: Forecasting Pacific SSTs: Linear inverse model predictions of the PDO. *J. Climate*, **21**, 385–402.

Alexander, M. A., D. J. Vimont, P. Chang, and J. D. Scott, 2010: The impact of extratropical atmospheric variability on ENSO: Testing the seasonal footprinting mechanism using coupled model experiments. *J. Climate*, **23**, 2885–2901.

Anderson, B. T., 2003: Tropical Pacific sea-surface temperatures and preceding sea level pressure anomalies in the subtropical North Pacific. *J. Geophys. Res.*, **108**, 4732, doi:10.1029/2003JD003805.

Anderson, B. T., 2007: Intraseasonal atmospheric variability in the extratropics and its relation to the onset of tropical pacific sea surface temperature anomalies. *J. Climate*, **20**, 926 – 936.

Anderson, B. T. and E. Maloney, 2006: Interannual tropical Pacific sea surface temperatures and their relation to preceding sea level pressures in the NCAR CCSM2. *J. Climate*, **19**, 998–1012.

Ashok, K., S. K. Behara, S. A. Rao, H. Y. Weng, and T. Yamagata, 2007: El Niño

Modoki and its possible teleconnection. *J. Geophys. Res.*, **112**, C11007, doi:10.1029/2006JC003798.

Ashok, K., C.-Y. Tam, and W.-J. Lee, 2009: ENSO Modoki impact on the Southern Hemisphere storm track activity during extended austral winter. *Geophys. Res. Lett.*, **36**, L12705, doi:10.1029/2009GL038847.

Barnett, T. P., 1984: Interaction of the monsoon and Pacific trade wind system at interannual time scales. *Mon. Wea. Rev.*, **112**, 2380–2387.

Barnett, T. P., D. W. Pierce, M. Latif, and D. Dommentget, 1999: Interdecadal interactions between the tropics and midlatitudes in the Pacific basin. *Geophys. Res. Lett.*, **26**, 615–618.

Barsugli, J. J. and D. S. Battisti, 1998: The basic effects of atmosphere-ocean thermal coupling on midlatitude variability. *J. Atmos. Sci.*, **55**, 477–493.

Barsugli, J. J. and P. D. Sardeshmukh, 2002: Global atmospheric sensitivity to tropical SST anomalies throughout the Indo-Pacific basin. *J. Climate*, **15**, 3427–3442.

Battisti, D. S., 1988: Dynamics and thermodynamics of a warming event in a coupled tropical atmosphere-ocean model. *J. Atmos. Sci.*, **45**, 2889–2919.

Battisti, D. S. and A. C. Hirst, 1989: Interannual variability in a tropical atmosphere-ocean model: Influence of the basic state, ocean geometry and nonlinearity. *J. Atmos. Sci.*, **46**, 1687–1712.

Bell, G. D., M. S. Halpert, V. E. Kousky, M. E. Gelman, C. F. Ropelewski, A. V. Douglas, and R. C. Schnell, 1999: Climate assessment for 1998. *Bull. Amer. Meteor. Soc.*, **80**, S1–S48.

Bengtsson, L., K. I. Hodges, and E. Roeckner, 2006: Storm tracks and climate change. *J. Climate*, **19**, 3518–3543.

Biondi, F., 2001: A 400-year tree-ring chronology from the tropical treeline of North America. *Ambio.*, **30**, 162–166.

Bjerknes, J., 1966: The possible response of the Hadley circulation to equatorial anomalies of ocean temperature. *Tellus*, **18**, 820–829.

Bladé, I., 1997: The influence of midlatitude coupling on the low frequency variability of a GCM. Part I: No tropical SST forcing. *J. Climate*, **10**, 2087–2106.

Boiseau, M., M. Ghil, and A. Juillet-Leclerc, 1999: Climatic trends and interdecadal variability from south-central Pacific coral records. *Geophys. Res. Lett.*, **26**, 2881–2884.

Bond, N. A., J. E. Overland, M. Spillane, and P. Stabeno, 2003: Recent shifts in the state of the North Pacific. *Geophys. Res. Lett.*, **30**, 2183, doi:10.1029/2003GL018597.

Bracco, A., F. Kucharski, F. Molteni, W. Hazeleger, and C. Severijns, 2006: A recipe for simulating the interannual variability of the Asian summer monsoon and its relation with ENSO. *Climate Dyn.*, **28**, 441–460.

Bradley, R. S., M. Vuille, D. Hardy, and L. G. Thompson, 2003: Low latitude ice cores record Pacific sea surface temperatures. *Geophys. Res. Lett.*, **30**, 1174, doi:10.1029/2002GL016546.

Bretherton, C. S., C. Smith, and J. M. Wallace, 1992: An intercomparison of methods for finding coupled patterns in climate data. *J. Climate*, **5**, 541–560.

Bretherton, C. S., M. Widmann, V. P. Dymnikov, J. M. Wallace, and I. Bladé, 1999: The effective number of spatial degrees of freedom of a time-varying field. *J. Climate*, **12**, 1990–2009.

Ceballos, L., E. D. Lorenzo, N. Schneider, and B. Taguchi, 2009: North Pacific Gyre Oscillation synchronizes climate fluctuations in the eastern and western North Pacific. *J. Climate*, **22**, 5163–5174.

Charles, C. D., K. Cobb, M. D. Moore, and R. G. Fairbanks, 2003: Monsoon-tropical ocean interaction in a network of coral records spanning the 20^{th} century. *Marine Geology*, **201**, 207–222.

Charles, C. D., D. E. Hunter, and R. G. Fairbanks, 1997: Interaction between the ENSO and the Asian Monsoon in a coral record of tropical climate. *Science*, **277**, 925–928.

Chhak, K., E. D. Lorenzo, N. Schneider, and P. Cummins, 2009: Forcing of low-frequency ocean variability in the Northeast Pacific. *J. Climate*, **22**, 1255–1276.

Cobb, K. M., C. D. Charles, and D. E. Hunter, 2001: A central tropical Pacific coral demonstrates Pacific, Indian, and Atlantic decadal climate connections. *Geophys. Res. Lett.*, **28**, 2209–2212.

Cole, J. E. and R. G. Fairbanks, 1990: The Southern Oscillation recorded in the oxygen isotopes of corals from Tarawa Atoll. *Paleoceanography*, **5**, 669–683.

Cole, J. E., R. B. Dunbar, T. R. McClanahan, and N. Muthiga, 2000: Tropical Pacific forcing of decadal variability in the western Indian Ocean over the past two centuries. *Science*, **287**, 617–619.

Curtis, J. H., M. Brenner, D. A. Hodell, R. A. Balser, G. A. Islebe, and H. Hooghiemstra, 1998: A multi-proxy study of Holocene environmental change in the Maya Lowlands of Peten, Guatemala. *J. Paleolimnology*, **19**, 139–159.

Dai, A. and T. M. L. Wigley, 2000: Global patterns of ENSO-induced precipitation. *Geophys. Res. Lett.*, **27**, 1283–1286.

D'Arrigo, R. D., G. C. Jacoby, and P. J. Krusic, 1994: Progress in dendroclimatic studies in Indonesia. *Terrestrial, Atmospheric and Oceanographic Sciences*, **5**, 349–363.

D'Arrigo, R. D., E. R. Cook, R. J. Wilson, R. Allan, and M. E. Mann, 2005: On the variability of ENSO over the past six centuries. *Geophys. Res. Lett.*, **32**, L03711, doi:10.1029/2004GL022055.

Davis, R. E., 1976: Predictability of sea surface temperature and sea level pressure anomalies over the North Pacific Ocean. *J. Phys. Oceanogr.*, **6**, 249–266.

Deser, C. and A. S. Phillips, 2006: Simulation of the 1976/77 climate transition over the North Pacific: Sensitivity to tropical forcing. *J. Climate*, **19**, 6170–6180.

Deser, C., M. A. Alexander, and M. S. Timlin, 2003: Understanding the persistence of sea surface temperature anomalies in midlatitudes. *J. Climate*, **16**, 57 – 72.

Deser, C., A. S. Phillips, and J. W. Hurrell, 2004: Pacific interdecadal climate variability: Linkages between the tropics and the North Pacific during boreal winter since 1900. *J. Climate*, **17**, 3109–3124.

Di Lorenzo, E., et al., 2009: Nutrient and salinity decadal variations in the central and eastern North Pacific. *Geophys. Res. Lett.*, **36**, L14601, doi:10.1029/2009GL038261.

Di Lorenzo, E., K. M. Cobb, J. C. Furtado, N. Schneider, B. T. Anderson, A. Bracco, M. A. Alexander, and D. J. Vimont, 2010: Central Pacific El Niño and decadal climate change in the North Pacific. *Nature Geoscience*, **3**, 762–765.

Di Lorenzo, E., et al., 2008: North Pacific Gyre Oscillation links ocean climate and ecosystem change. *Geophys. Res. Lett.*, **35**, L08607, doi:10.1029/2007GL032838.

Driffel, E. R. M. and S. Griffin, 1993: Large variations of surface ocean radiocarbon:

Evidence of circulation changes in the southwestern Pacific. *J. Geophys. Res.*, **98**, 20 246–20 259.

Dunbar, R. B., G. M. Wellington, M. W. Colgan, and P. W. Glynn, 1994: Eastern Pacific sea surface temperature since 1600 A.D.: The δ^{18}O record of climate variability in Galápagos corals. *Paleoceanography*, **9**, 291–315.

Ebbesmeyer, C. C., D. Cayan, D. R. Milan, F. H. Nichols, D. H. Peterson, and K. T. Redmond, 1991: 1976 step in the Pacific climate: Forty environmental changes between 1968-1975 and 1977-1984. *Proceedings of the Seventh Annual Climate (PACLIM) Workshop, April 1990*, J. L. Betancourt and V. L. Tharp, Eds., California Department of Water Resources, 115–126.

Evans, M. N., A. Kaplan, and M. A. Cane, 1998: Optimal sites for coral-based reconstruction of global sea surface temperature. *Paleoceanography*, **13**, 502–516.

Evans, M. N., R. G. Fairbanks, and J. L. Rubenstone, 1999: The thermal oceanographic signal of El Niño reconstructed from a Kiritimati Island coral. *J. Geophys. Res.*, **104**, 13 409–13 421.

Evans, M. N., M. A. Cane, D. P. Schrag, A. Kaplan, B. K. Linsley, R. Villalba, and G. M. Wellington, 2001: Support for tropically-driven Pacific decadal variability based on paleoproxy evidence. *Geophys. Res. Lett.*, **28**, 3689–3692.

Evans, M. N., A. Kaplan, and M. A. Cane, 2002: Pacific sea surface temperature field reconstruction from coral δ^{18}O data using reduced space objective analysis. *Paleoceanography*, **17**, 1007, doi:0.1029/2000PA000590.

Federov, A. V. and S. G. Philander, 2000: Is El Niño changing? *Science*, **288**, 1997–2002.

Federov, A. V. and S. G. Philander, 2001: A stability analysis of tropical ocean-atmosphere interactions: Bridging measurements and theory of El Niño. *J. Climate*, **14**, 3086–3101.

Federov, A. V. and S. G. Philander, 2003: Is El Niño sporadic or cyclic? *Annu. Rev. Earth Planet. Sci.*, **31**, 579–594.

Francis, R. C. and T. H. Sibley, 1991: Climate change and fisheries: What are the real issues? *NW Env. J.*, **7**, 295–307.

Furtado, J. C., E. Di Lorenzo, K. M. Cobb, and A. Bracco, 2009: Paleoclimate reconstructions of tropical sea surface temperatures from precipitation proxies: Methods, uncertainties and nonstationarity. *J. Climate*, **22**, 1104–1123.

Furtado, J. C., E. Di Lorenzo, N. Schneider, and N. Bond, 2010: North Pacific decadal variability and climate change in the IPCC AR4 models. *J. Climate*, in press.

Goddard, L. and N. E. Graham, 1997: El Niño in the 1990s. *J. Geophys. Res.*, **102**, 10 423–10 436.

Graham, N. E., T. P. Barnett, R. Wilde, M. Ponater, and S. Schubert, 1994: On the roles of tropical and midlatitude SSTs in forcing annual to interdecadal variability in the winter Northern Hemisphere circulation. *J. Climate*, **7**, 1416–1442.

Gu, D. F. and S. G. H. Philander, 1997: Interdecadal climate fluctuations that depend on exchanges between the tropics and extratropics. *Science*, **275**, 805–807.

Guilderson, T. P. and D. P. Schrag, 1999: Reliability of coral isotope records from the western Pacific warm pool: A comparison using age-optimized record. *Paleoceanography*, **14**, 457–464.

Guilyardi, E., 2006: El Niño-mean state-seasonal cycle interactions in a multi-model ensemble. *Climate Dyn.*, **26**, 329–348.

Hartmann, D. L., cited 2010: Chapter 6: Time (or Space) Series Analysis. [Available online at `http://www.atmos.washington.edu/~dennis/552_Notes_ftp.html`].

Haug, G. H., K. A. Hughen, D. M. Sigman, L. C. Peterson, and U. Röhl, 2001: Southward migration of the Intertropical Convergence Zone through the Holocene. *Science*, **293**, 1304–1308.

Heiss, G. A., 1994: Coral reefs in the Red Sea: Growth, production and stable isotopes. GEOMAR Tech Rep. 32, GEOMAR, 141 pp.

Hendy, E. J., M. K. Gagan, C. A. Alibert, M. T. McCulloch, J. M. Lough, and P. J. Isdale, 2002: Abrupt decrease in tropical Pacific sea surface salinity at end of Little Ice Age. *Science*, **291**, 1511–1514.

Hoerling, M. P. and A. Kumar, 2002: Atmospheric response patterns associated with tropical forcing. *J. Climate*, **15**, 2184–2203.

Hoskins, B. J. and D. J. Karoly, 1981: The steady linear response of a spherical atmosphere to thermal and orographic forcing. *J. Atmos. Sci.*, **38**, 1179–1196.

Jin, F.-F., 1997: An equatorial recharge paradigm for ENSO. Part I: Conceptual model. *J. Atmos. Sci.*, **54**, 811–829.

Kim, K.-Y. and G. R. North, 1999: EOF-based linear prediction algorithm: Examples. *J. Climate*, **12**, 2076–2092.

Kistler, R., et al., 2001: The NCEP-NCAR 50-Year Reanalysis: Monthly means CD-ROM and documentation. *Bull. Amer. Meteor. Soc.*, **82**, 247–267.

Kleeman, R., J. P. M. Jr, and B. A. Klinger, 1999: A mechanism for generating ENSO decadal variability. *Geophys. Res. Lett.*, **26**, 1743–1746.

Knutson, T. R. and S. Manabe, 1998: Model assessment of decadal variability and trends in the tropical Pacific Ocean. *J. Climate*, **11**, 2273–2296.

Kucharski, F., F. Molteni, and J. H. Yoo, 2006: SST forcing of decadal Indian Monsoon rainfall variability. *Geophys. Res. Lett.*, **33**, L03709, doi:10.1029/2005GL025371.

Kucharski, F., A. Bracco, J. H. Yoo, and F. Molteni, 2007: Low-frequency variability of the Indian Monsoon–ENSO relationship and the tropical Atlantic: The "weakening" of the 1980s and 1990s. *J. Climate*, **20**, 4255–4266.

Kug, J.-S. and I.-S. Kang, 2006: Interactive feedback between ENSO and the Indian Ocean. *J. Climate*, **19**, 1784–1801.

Kug, J.-S., J. Choi, S.-I. An, F.-F. Jin, and A. T. Wittenberg, 2010: Warm Pool and Cold Tongue El Niño events as simulated by the GFDL 2.1 coupled GCM. *J. Climate*, **23**, 1226–1239.

Kuhnert, H., J. Pätzold, B. Hatcher, K.-H. Wyrwoll, A. Eisenhauer, L. B. Collins, Z. R. Zhu, and G. Wefer, 1999: A 200-year coral stable oxygen isotope record from a high-latitude reef off Western Australia. *Coral Reefs*, **18**, 1–12.

Kuhnert, H., J. Pätzold, K.-H. Wyrwoll, and G. Wefer, 2000: Monitoring climate variability over the past 116 years in coral oxygen isotopes from Ningaloo Reef, Western Australi. *Int. J. Earth. Sci.*, **88**, 725–732.

Kutzbach, J. E., 1967: Empirical eigenvectors of sea-level pressure, surface pressure and precipitation complexes over North America. *J. Appl. Meteor.*, **6**, 791 – 802.

Latif, M. and T. P. Barnett, 1996: Decadal climate variability over the North Pacific and North America: Dynamics and predictability. *J. Climate*, **9**, 2407–2423.

Linkin, M. E. and S. Nigam, 2008: The North Pacific Oscillation-West Pacific teleconnection pattern: Mature-phase structure and winter impacts. *J. Climate*, **21**, 1979–1997.

Linsley, B. K., R. B. Dunbar, G. M. Wellington, and D. A. Mucciarone, 1994: A coral-based reconstruction of intertropical convergence zone variability over Central America since 1707. *J. Geophys. Res.*, **99**, 9977–9994.

Linsley, B. K., L. Ren, R. B. Dunbar, and S. S. Howe, 2000a: El Niño Southern Oscillation (ENSO) and decadal-scale climate variability at 10N in the eastern Pacific from 1893 to 1994: A coral-based reconstruction from Clipperton Atoll. *Paleoceanography*, **15**, 322–335.

Linsley, B. K., G. M. Wellington, and D. P. Schrag, 2000b: Decadal sea surface temperature variability in the subtropical South Pacific from 1726 to 1997 A.D. *Science*, **290**, 1145–1148.

Liu, Z. and M. A. Alexander, 2007: Atmospheric bridge, oceanic tunnel, and global climate teleconnections. *Rev. Geophys.*, **45**, RG2005, doi:10.1029/2005RG000172.

Lorenz, E. N., 1956: Empirical orthogonal functions and statistical weather prediction. Sci. Rep. No. 1, Statistical Forecasting Project, MIT, 48 pp.

Madden, R. A. and P. R. Julian, 1971: Description of a 40-50 day oscillation in the zonal wind in the tropical pacific. *J. Atmos. Sci.*, **28**, 702–708.

Madden, R. A. and P. R. Julian, 1994: Observations of the 40-50 day tropical oscillation - A review. *Mon. Wea. Rev.*, **122**, 814–837.

Mann, M. E. and S. Rutherford, 2002: Climate reconstructions using 'pseudoproxies'. *Geophys. Res. Lett.*, **29**, 1501, doi:10.1029/2001gl014554.

Mann, M. E., R. S. Bradley, and M. K. Hughes, 1998: Global-scale temperature patterns and climate forcing over the past six centuries. *Nature*, **392**, 779–787.

Mann, M. E., S. Rutherford, E. Wahl, and C. Ammann, 2005: Testing the fidelity

of methods used in proxy-based reconstructions of past climate. *J. Climate*, **18**, 4097–4107.

Mann, M. E., S. Rutherford, E. Wahl, and C. Ammann, 2007: Robustness of proxy-based climate field reconstruction methods. *J. Geophys. Res.*, **112**, D12109, doi: 10.1029/2006JD008272.

Mantua, N. J. and S. R. Hare, 2000: The Pacific Decadal Oscillation. *J. Oceanogr.*, **58**, 35–44.

Mantua, N. J., S. R. Hare, Y. Zhang, J. M. Wallace, and R. Francis, 1997: A Pacific interdecadal climate oscillation with impacts on salmon production. *Bull. Amer. Meteor. Soc.*, **78**, 1069–1079.

Meehl, G. A., H. Teng, and G. Branstator, 2006: Future changes of El Niño in two global coupled climate models. *Climate Dyn.*, **26**, 549–566.

Merryfield, W. J., 2006: Changes to ENSO under CO_2 doubling in a multimodel ensemble. *J. Climate*, **19**, 4009–4027.

Michaelson, J., 1989: Long-period fluctuations in El Niño amplitude and frequency reconstructed from tree rings. *Aspects of Climate Variability in the Pacific and Western Americas*, Amer. Geophys. Union, Geophys. Monogr., Vol. 55, 69–74.

Miller, A. J., D. R. Cayan, T. P. Barnett, N. E. Graham, and J. M. Oberhuber, 1994: The 1976-77 climate shift of the Pacific Ocean. *Oceanogr.*, **7**, 21–26.

Miller, A. J., F. Chai, S. Chiba, J. R. Moisan, and D. J. Neilson, 2004: Decadal-scale climate and ecosystem interactions in the North Pacific Ocean. *J. Oceanogr.*, **60**, 163–188.

Molteni, F., 2003: Atmospheric simulations using a GCM with simplified physical

parameterization. I: Model climatology and variability in multi-decadal experiment. *Climate Dyn.*, **20**, 175–191.

Moy, C. M., G. O. Seltzer, D. T. Rodbell, and D. M. Anderson, 2002: Variability of El Niño/Southern Oscillation activity at millennial timescales during the Holocene epoch. *Nature*, **420**, 162–165.

Namias, J., 1969: Seasonal interactions between the North Pacific Ocean and the atmosphere during the 1960's. *Mon. Wea. Rev.*, **97**, 173–192.

Namias, J., 1972: Experiments in objectively predicting some atmospheric and oceanic variables for the winter of 1971-1972. *J. Appl. Meteor.*, **11**, 1164–1174.

Neelin, J. D., 1991: The slow sea surface temperature mode and the fast-wave limit: Analytic theory for a tropical interannual oscillations and experiments in a hybrid coupled model. *J. Atmos. Sci.*, **48**, 584–606.

Neelin, J. D., M. Latif, and F.-F. Jin, 1994: Dynamics of coupled ocean-atmosphere models: The tropical problem. *Annu. Rev. Fluid Mech.*, **26**, 617–659.

Newman, M., 2007: Interannual to decadal predictability of tropical and North Pacific sea surface temperatures. *J. Climate*, **20**, 2333–2356.

Newman, M., G. P. Compo, and M. A. Alexander, 2003: ENSO-forced variability of the Pacific Decadal Oscillation. *J. Climate*, **16**, 3853–3857.

North, G. R., T. L. Bell, R. F. Cahalan, and F. J. Moeng, 1982: Sampling errors in the estimation of empirical orthogonal functions. *Mon. Wea. Rev.*, **110**, 699–706.

Obukhov, A. M., 1947: Statistically homogeneous fields on a sphere. *Usp. Mat. Nauk*, **2**, 196–198.

Overland, J. and M. Wang, 2007: Future climate of the North Pacific Ocean. *EOS*, **88**, 178–182.

Partin, J. W., K. M. Cobb, J. F. Adkins, B. Clark, and D. P. Fernadez, 2007: Millennial-scale trends in west Pacific warm pool hydrology since the Last Glacial Maximum. *Nature*, **449**, 452–455.

Pätzold, J., 1984: Growth rhythms recorded in stable isotopes and density bands in the reef coral *Porites lobata* (Cebu, Phillipines). *Coral Reefs*, **3**, 87–90.

Penland, C. and P. D. Sardeshmukh, 1995: The optimal growth of tropical sea surface temperature anomalies. *J. Climate*, **8**, 1999–2024.

Pfeiffer, M., O. Timm, W.-C. Dullo, and S. Podlech, 2004: Oceanic forcing of interannual and multidecadal climate variability in the southwestern Indian Ocean: Evidence from a 160 year coral isotopic record (La Réunion, 55 °E, 21 °S). *Paleoceanography*, **19**, PA4006, doi:10.1029/2003PA000964.

Pierce, D. W., T. P. Barnett, N. Schneider, R. Saravanan, D. Dommentget, and M. Latif, 2001: The role of ocean dynamics in producing decadal climate variability in the North Pacific. *Climate Dyn.*, **18**, 51–70.

Quayle, R. G., 1989: The Wolbach Dataset for global climate monitoring - Philanthropy and climatology. *Bull. Amer. Meteor. Soc.*, **70**, 1570.

Quinn, T. M., T. J. Crowley, and F. W. Taylor, 1996: New stable isotope results from a 173-year coral record from Espiritu Santo, Vanuatu. *Geophys. Res. Lett.*, **23**, 3412–3416.

Quinn, T. M., T. J. Crowley, F. W. Taylor, C. Henin, P. Joannot, and Y. Join, 1998: A multicentury stable isotope record from a New Caledonia coral: Interannual and decadal sea surface temperature variability in the southwest Pacific since 1657 A.D. *Paleoceanography*, **13**, 412–426.

Rasbury, M. and P. Aharon, 2006: ENSO-controlled rainfall variability records archived in tropical stalagmites from the mid-ocean island of Niue, South Pacific. *Geochem. Geophys. Geosyst.*, **7**, Q07010, doi:10.1029/2005GC001232.

Rasmusson, E. M. and T. H. Carpenter, 1982: Variations in tropical sea surface temperature and surface wind fields associated with the Southern Oscillation/El Niño. *Mon. Wea. Rev.*, **110**, 354–384.

Rayner, N. A., D. E. Parker, E. B. Horton, C. K. Folland, L. V. Alexander, D. P. Rowell, E. C. Kent, and A. Kaplan, 2003: Global analyses of sea surface temperature, sea ice, and night marine air temperature since the late nineteenth century. *J. Geophys. Res.*, **108**, 4407, doi:10.1029/2002JD002670.

Reifen, C. and R. Toumi, 2009: Climate projections: Past performance no guarantee of future skill? *Geophys. Res. Lett.*, **36**, L13704, doi:10.1029/2009GL038082.

Rein, B., A. Lückge, and F. Sirocko, 2004: Major Holocene ENSO anomaly during the Medieval period. *Geophys. Res. Lett.*, **31**, L17211, doi:10.1029/2004GL020161.

Rodbell, D., G. O. Seltzer, D. M. Anderson, D. B. Enfield, M. B. Abbott, and J. H. Newman, 1999: A high-resolution 15000 year record of El Niño driven alluviation in southwestern Ecuador. *Science*, **283**, 516–520.

Rogers, J. C., 1981: The North Pacific Oscillation. *J. Climatol.*, **1**, 39–57.

Schneider, N. and B. D. Cornuelle, 2005: The forcing of the Pacific Decadal Oscillation. *J. Climate*, **18**, 4355–4373.

Schneider, N., A. J. Miller, M. A. Alexander, and C. Deser, 1999: Subduction of decadal North Pacific temperature anomalies: Observations and dynamics. *J. Phys. Oceanogr.*, **29**, 1056–1070.

Schopf, P. S. and M. J. Suarez, 1987: Vacillations in a coupled ocean-atmosphere model. *J. Atmos. Sci.*, **45**, 549–566.

Shen, G. T., J. E. Cole, D. Lea, L. J. Linn, T. A. McConnaughey, and R. G. Fairbanks, 1992: Surface ocean variability at Galapagos from 1936–1982: Calibration of geochemical tracers in corals. *Paleoceanography*, **7**, 563–588.

Simmons, A. J. and J. K. Gibson, 2000: The ERA-40 Project Plan. ERA-40 Project Rep. Series No. 1, 62 pp.

Smith, T. M., R. W. Reynolds, T. C. Peterson, and J. Lawrimore, 2008: Improvements to NOAA's historical Merged Land–Ocean Surface Temperature Analysis (1880–2006). *J. Climate*, **21**, 2283–2296.

Spencer, R. W., 1993: Global oceanic precipitation from the MSU during 1979–91 and comparisons to other climatologies. *J. Climate*, **6**, 1301–1326.

Stahle, D. W., et al., 1998: Experimental dendroclimatic reconstruction of the Southern Oscillation. *Bull. Amer. Meteor. Soc.*, **79**, 2137–2152.

Stahle, D. W., P. T. Mushove, M. K. Cleaveland, F. Roig, and G. A. Haynes, 1999: Management implications of annual growth rings in *Pterocarpus angolensis* from Zimbabwe. *For. Ecolo. Manage.*, **124**, 217–229.

Stott, L., K. Cannariato, R. Thunell, G. H. Haug, A. Koutavas, and S. Lund, 2004: Decline of surface temperature and salinity in the western tropical Pacific Ocean in the Holocene epoch. *Nature*, **431**, 56–59.

Street-Perrott, F. A., D. S. Marchand, N. Roberts, and S. P. Harisson, 1989: Global lake-level variations from 18,000 to 0 years ago: A paleoclimatic analysis. U.S. Department of Energy Tech. Rep. 46, 44 pp.

Streten, N. A., 1973: Some characteristics of satellite observed bands of persistent cloudiness over the Southern Hemisphere. *Mon. Wea. Rev.*, **101**, 486–494.

Suarez, M. J. and P. S. Schopf, 1988: A delayed action oscillator for ENSO. *J. Atmos. Sci.*, **45**, 3283–3287.

Taguchi, B., S.-P. Xie, N. Schneider, M. Nonaka, H. Sasaki, and Y. Sasai, 2007: Decadal variability of the Kuroshio Extension: Observations and an eddy-resolving model hindcast. *J. Climate*, **20**, 2357–2377.

Teng, H., W. M. Washington, and G. A. Meehl, 2008: Interannual variations and future change of extratropical cyclone activity over North America in CCSM3. *Climate Dyn.*, **30**, 673–686.

Therrell, M. D., D. W. Stahle, M. K. Cleaveland, and J. Villanueva-Diaz, 2002: Warm season tree growth and precipitation over Mexico. *J. Geophys. Res.*, **107**, 4205, doi:10.1029/2001JD000851.

Thompson, L. G., E. Mosley-Thompson, J. F. Bolzan, and B. R. Koci, 1985: A 1500 year record of tropical precipitation recorded in ice cores from the Quelccaya Ice Cap, Peru. *Science*, **229**, 971–973.

Thompson, L. G., E. Mosley-Thompson, M. E. Davis, P.-N. Lin, K. A. Henderson, J. Cole-Dai, J. F. Bolzan, and K.-B. Liu, 1995: Late glacial stage and Holocene tropical ice core records from Huascarán, Peru. *Science*, **269**, 46–50.

Thompson, L. G., et al., 2002: Kilimanjaro ice core records: Evidence of Holocene climate change in tropical Africa. *Science*, **298**, 589–593.

Torrence, C. and G. P. Compo, 1998: A practical guide to wavelet analysis. *Bull. Amer. Meteor. Soc.*, **79**, 61–78.

Trenberth, K. E., 1990: Recent observed interdecadal climate changes in the Northern Hemisphere. *Bull. Amer. Meteor. Soc.*, **71**, 988–993.

Trenberth, K. E. and J. W. Hurrell, 1994: Decadal atmosphere-ocean variations in the Pacific. *Climate Dyn.*, **9**, 1004–1020.

Tudhope, A. W., et al., 2001: Variability in the El Niño Southern Oscillation through a glacial–interglacial cycle. *Science*, **291**, 1511–1517.

Ulbrich, U., J. G. Pinto, H. Kupfer, C. Leckebusch, T. Spangehl, and M. Reyers, 2008: Changing Northern Hemisphere storm tracks in an ensemble of IPCC climate change simulations. *J. Climate*, **21**, 1669–1679.

Urban, F. E., J. E. Cole, and J. T. Overpeck, 2000: Influence of mean climate change on climate variability from a 155-year tropical Pacific coral record. *Nature*, **407**, 989–993.

van Loon, H., G. A. Meehl, and R. F. Millhiff, 2003: The Southern Oscillation in the early 1990s. *Geophys. Res. Lett.*, **30**, 1478, doi:10.1029/2002GL016307.

van Oldenborgh, G. J., S. Y. Philip, and M. Collins, 2005: El Niño in a changing climate: A multi-model study. *Ocean Sci.*, **1**, 81–95.

Vimont, D. J., D. S. Battisti, and A. C. Hirst, 2001: Footprinting: A seasonal connection between the tropics and mid-latitudes. *Geophys. Res. Lett.*, **28**, 3923–3926.

Vimont, D. J., J. M. Wallace, and D. S. Battisti, 2003: The seasonal footprinting mechanism in the Pacific: Implications for ENSO. *J. Climate*, **16**, 2668–2675.

Vimont, D. J., M. A. Alexander, and A. Fontaine, 2009: Midlatitude excitation of tropical variability in the Pacific: The role of thermodynamics coupling and seasonality. *J. Climate*, **22**, 518–534.

Walker, G. T. and E. W. Bliss, 1932: World weather V. *Mem. Roy. Meteor. Soc.*, **4**, 53–84.

Wallace, J. M., E. M. Rasmusson, T. P. Mitchell, V. E. Kousky, E. S. Sarachik, and H. von Storch, 1998: On the structure and evolution of ENSO-related climate variability in the tropical Pacific: Lessons from TOGA. *J. Geophys. Res.*, **103**, 14 241–14 259.

Weng, H. Y., K. Ashok, S. K. Behera, S. A. Rao, and T. Yamagata, 2007: Impacts of recent El Niño Modoki on dry/wet conditions in the Pacific rim during boreal summer. *Climate Dyn.*, **29**, 113–129.

Weng, H. Y., S. K. Behera, and T. Yamagata, 2009: Anomalous winter climate conditions in the Pacific rim during recent El Niño Modoki and El Niño events. *Climate Dyn.*, **32**, 663–674.

Wilks, D. S., 2006: *Statistical Methods in the Atmospheric Sciences*. 2d ed., Elsevier Inc., 627 pp.

Winter, A., T. Oba, H. Ishioroshi, T. Watanabe, and J. Christy, 2000: Tropical sea surface temperatures: Two-to-three degrees cooler than present during the Little Ice Age. *Geophys. Res. Lett.*, **27**, 3365–3368.

Wunsch, C., 2006: Basic machinery. *Discrete Inverse and State Estimation Problems with Geophysical Fluid Applications*, Cambridge University Press, 19–151.

Wyrtki, K., 1975: El Niño-the dynamic response of the equatorial Pacific Ocean to atmospheric forcing. *J. Phys. Oceanogr.*, **5**, 572–584.

Xie, P. and P. A. Arkin, 1997: Global precipitation: A 17-year monthly analysis based on gauge observations, satellite estimates, and numerical model outputs. *Bull. Amer. Meteor. Soc.*, **78**, 2539–2558.

Yasuda, I., H. Sugusaki, Y. Watanabe, S. Minobe, and Y. Oozeki, 1999: Interdecadal variations in Japanese sardine and ocean/climate. *Fish. Oceanogr.*, **8**, 18–24.

Yeh, S.-W. and B. P. Kirtman, 2007: ENSO amplitude changes due to climate change projections in different coupled models. *J. Climate*, **20**, 203–217.

Yeh, S.-W., J.-S. Kug, B. Dewitte, M.-H. Kwon, B. P. Kirtman, and F.-F. Jin, 2009: El Niño in a changing climate. *Nature*, **461**, 511–514.

Yu, J.-Y., C. R. Mechoso, J. C. McWilliams, and A. Arakawa, 2002: Impacts of the Indian Ocean on the ENSO cycle. *Geophys. Res. Lett.*, **29**, 1204, doi:10.1029/2001GL014098.

Zhang, Y., J. M. Wallace, and D. S. Battisti, 1997: ENSO-like interdecadal variability. *J. Climate*, **10**, 1004–1020.

Zinke, J., W.-C. Dullo, G. A. Heiss, and A. Eisenhauer, 2004: ENSO and Indian Ocean subtropical dipole variability is recorded in a coral record off southwest Madagascar for the period 1659 to 1995. *Earth Planet. Sci. Lett.*, **228**, 177–194.